University of Leoben

PhD Thesis

The microstructural break down: the effect of initial grain size

Christian Rupert Rehrl

Leoben, July 2011

To Andrea

Affidavit

I declare in lieu of oath, that I wrote this thesis and performed the associated research myself, using only literature cited in this volume.

Leoben, July 2011

Acknowledgements

I would like to express my gratitude to a number of persons who have contributed and supported me during course of this work. I, particularly, wish to thank:

- Reinhard Pippan, my supervisor, for his guidance and support and for giving an expertise to this thesis.
- Siegfried Kleber, my co-supervisor, for his support and help and the patience at all stages of my work.
- Gerhard Dehm, the head of the department of materials physics for giving me the opportunity to work here.
- Thomas Antretter, for supporting the modeling part of my thesis.
- My office colleagues, former office colleagues and "non-office" colleagues, Marianne Kapp, Kut Matoy, Christian Motz, Oliver Renk, Wolfgang Pranger, Bernhard Völker, Megan Cordill and Stefan Wurster, for their help and countless discussions.
- Edeltraud Haberz, for the excellent sample preparation and Franz Hubner, Günter Aschauer for the fabrication of specimens and various apparatuses.
- All employees of the Erich Schmid Institute for their help.
- My family and friends for their support and friendship.

Abstract

Production of high quality materials is an important target of the metal forming industry. A low quantity of inclusions and a well defined microstructure are essential if good mechanical and physical properties are to be obtained. Remelting processes are widely used to remove impurities and lead to a more homogeneous microstructure compared to the cast structured state. Mechanical properties and microstructure are improvable. In metals without a solid state phase transformation (Ni, Cu, Al, γ-iron), structural break down is the unique process to refine and homogenize the heterogeneous state. Hence, it is necessary to understand deformation mechanisms and the acting softening phenomena; recovery and recrystallization. The present thesis is devoted to the fundamental understanding of the effects of initial grain size and forming parameters on the microstructural refinement and homogenization. Experiments were performed using the model material pure nickel and a technically relevant austenitic stainless steel (Böhler A220) at different forming conditions. Different initial grain size states in the μm- to mm range were used. Special attention has been devoted to the investigation of the deformation microstructure and the potential of crystal plasticity-FEM models to predict the crystal fragmentation processes.

For pure nickel and the austenitic stainless steel, the softening mechanisms acting during the deformation at elevated forming temperatures are dynamic recovery and dynamic recrystallization, nevertheless, in both materials the initial microstructure has a significant effect on the structural evolution during hot forming. A coarsening of the starting microstructure retards and slows down the dynamic recrystallization kinetics. The increase in grain size directly reduces the density of potential nucleation sites and decreases the stored energy, which is a well known driving force for microstructural instability, at these positions. New grains are formed by a discontinuous dynamic recrystallization process, where initial grain boundaries act as potential nucleation sites. The nucleation process can be characterized by extensive grain-boundary motion, bulging and annealing twinning, whereas the alloying content of the austenitic steel clearly reduces the grain boundary mobility. For the break down process in coarser grained structures, intragranular inhomogeneities (deformation bands or subgrain boundaries) serve as nucleation sites. For the first time it could be clearly shown for pure nickel that the dynamically recrystallized grain size depends significantly on the initial microstructure.

With crystal plasticity models based on dislocation slip, the crystal orientation evolution – which is strongly dependent on the initial grain orientation, sample geometry and boundary conditions – and the evolution of strain gradients and rigid body rotation can be captured. It has been shown that such models can predict quite well the generated inhomogeneities from grain to grain interaction or the sample geometry, however they cannot explain the dislocation structure governed fragmentation. A slight modification of the first model used, by deactivation of slip systems and the implementation of a structural length scale, delivers the experimentally observed substructures.

The problem of refining coarse grained materials is clearly based on a weak tendency to recrystallize. For an efficient industrial forming process, a double hit forming strategy which uses static- and dynamic recrystallization is recommended.

Kurzfassung

Für Stahlproduzenten ist die Herstellung von qualitativ hochwertigen Werkstoffen ein Hauptziel. Das Einstellen einer definierten Mikrostruktur bei möglichst niedriger Anzahl von Einschlüssen kann als Schlüssel zu guten mechanischen und physikalischen Eigenschaften gesehen werden. Durch das Umschmelzen erreicht man reinere Werkstoffe mit niedriger Einschlussdichte und homogenerer Mikrostruktur als bei konventionellen Gusswerkstoffen. Bedingt durch ausgeprägte Textur und grobkörnige Struktur sind die mechanischen Eigenschaften verbesserungsfähig. Für spezielle Werkstoffgruppen, welche über keine Phasenumwandlung im Festen verfügen (Ni, Cu, Al, γ-Eisen), kann nur über einen Warmumformprozess eine homogene und feinkörnige Mikrostruktur eingestellt werden. Das Feinen und Homogenisieren der Ausgangsstruktur setzt ein hohes Maß an Verständnis der zugrunde liegenden metallphysikalischen Prozesse wie Erholung und Rekristallisation voraus.
Ziel dieser Untersuchung ist es durch die Charakterisierung der Einflussfaktoren Ausgangskorngröße und Umformparameter ein tieferes Verständnis über den Kornfeinungs- und Homogenisierungsvorgang zu erlangen. Untersucht wurden die Werkstoffe Reinnickel und eine austenitische FeCrNi Legierung, Marke Böhler A220 mit Ausgangskorngrößen vom μm bis mm-Bereich. Die Entwicklung und die experimentelle Erfassung der Verformungsstruktur, sowie die Analyse des Potentials mit Hilfe kristallplastischer Finite Elemente Modelle die Kristallfragmentierung zu beschreiben, waren wesentliche Punkte dieser Arbeit.
Beide Werkstoffe zeigen während der Verformung bei höheren Umformtemperaturen in ihrem Entfestigungsverhalten das Auftreten von dynamischer Erholung und dynamischer Rekristallisation sowie einen starken Einfluss der Ausgangsmikrostruktur auf die weitere Strukturentwicklung. Die Variation der Ausgangskorngröße zeigt, dass in gröberen Ausgangsstrukturen die Rekristallisation verlangsamt und erst bei höherer plastischer Verformung einsetzt. Durch diese Änderung der Korngröße verringert sich die potentielle Keimstellendichte und die gespeicherte Verformungsenergie an diesen Stellen ist geringer, wodurch der Drang zur Neubildung des Gefüges abnimmt. Als Keimstellen des diskontinuierlichen Rekristallisationsprozesses dienen meist die ursprünglichen Korngrenzen, deren Beweglichkeit eine notwendige Eigenschaft zum Einformen eines Keims ist. Charakteristisch für das Formen eines Korns ist die Beweglichkeit und das Krümmen der Korngrenze, sowie die Bildung eines Glühzwillings. Das Zulegieren von Elementen, typisch für technische Werkstoffe, verringert die Korngrenzenmobilität und erschwert die Keimbildung. In sehr grobkörnigen Ausgangsstrukturen dienen aufgrund der niedrigen Korngrenzendichte auch strukturelle Inhomogenitäten im Korninneren (Verformungsbänder, Subkorngrenzen) als Keimstellen. Es konnte in dieser Arbeit erstmals deutlich gezeigt werden, dass im Werkstoff Reinnickel die dynamisch rekristallisierte Korngröße sehr stark von der Ausgangsstruktur abhängt.
Die kristallplastische Modellierung der Strukturentwicklung mit Finite Elemente Modellen, welche auf der Versetzungsplastizität beruhen, zeigt – unter der Berücksichtigung von der Kornorientierung, Probengeometrie und den Randbedingungen der Verformung – dass Dehnungsgradienten und Starrkörperrotationen richtig wiedergegeben werden können. Das Potential dieser Modelle liegt in der Vorhersage von Verformungsinhomogenitäten, welche von Kornwechselwirkung oder Probengeometrie verursacht werden. Die auf der Versetzungsstruk-

tur beruhende Fragmentierung eines Kristalls zeigt klar die Grenze dieser Modelle. Durch eine leichte Modifikation des Modells, indem man einen strukturellen Längenmaßstab einführt und Gleitsysteme gezielt ausschaltet, ist es möglich die kristallographische Fragmentierung zu beschreiben.
Das Hauptproblem für das Feinen von grobkörnigen und heterogenen Mikrostrukturen liegt klarerweise in ihrem schwachen Rekristallisationsverhalten begründet. Als Empfehlung für die industrielle Umformung von groben Strukturen sollte ein zweistufiger Prozess angestrebt werden. In diesem wird die statische und dynamische Rekristallisation zum Kornfeinen und Homogenisieren verwendet.

I was born not knowing
and have had only a little time to change
that here and there.

Richard P. Feynman

Contents

1 Introduction and motivation

1.1. Physical mechanisms determining warm forming behavior

For the description of microstructural evolution, the knowledge of the physical mechanisms which are determining the final microstructure are essential. During the forming steps at elevated temperature the material undergoes a hardening by dislocation storage and a softening by recovery and recrystallization. The understanding of these physical mechanisms, as well as their mathematical description, allows one to tailor mechanical and physical properties of the material by setting the microstructure. The softening mechanisms can be related to their occurrence during or after the deformation process. They can be classified into dynamic recovery, dynamic recrystallization (during deformation) and static recovery, static recrystallization (after deformation). The general driving force for all softening mechanisms is to minimize the total energy of a system by a change to a low energy dislocation configuration.

1.1.1. Static and dynamic recovery

During the recovery process the stored deformation energy can be reduced by removal (annihilation) or rearrangement (polygonization, cell formation) of the randomly arranged dislocation structure. This continuous process proceeds without any incubation time and without high angle grain boundary movement. Dynamic recovery (DRV) reduces the hardening due to thermal activated dislocation cross slip or climbing while a material plastically deforms. Owing to their long range stress fields dislocations interact. Thermally activated dislocations migrate and dislocations annihilate or polygonize and form subgrain boundaries. For DRV and dynamic recrystallization (DRX), the stored energy is the driving force and both processes compete with each other. In high stacking fault energy materials (e.g. aluminum) DRV is the main softening mechanism, whereas medium to low stacking fault energy metals tend more to DRX.[1–4]
It is well known in the literature[4–6] that DRV is essential to form a movable subgrain boundary which is assumed an essential step for the formation of a DRX nucleus. The static recovery acts between deformation steps or after the deformation. Basically the mechanisms are the same as for DRV, dislocation annihilation and polygonisation. Further details on the softening mechanisms are given in the excellent textbook of Humphreys and Hatherly.[4]

1.1.2. Static and dynamic recrystallization

Recovery is a relatively homogeneous process, whereas recrystallization can be seen as strongly discontinuous by formation of a new grain and its growth. The microstructural change can be characterized by a new grain structure with a lower dislocation density compared to the deformed or recovered one. In medium to low stacking fault energy materials, such as Ni, Cu and γ-iron, recrystallization dominates the softening of the material and the structural evolution. Conforming with the nomenclature of Humphreys and Hatherley,[4] "recrystallization" will be used in terms of the primary recrystallization of a deformed microstructure. In the case of static recrystallization, the as worked state of the material undergoes nucleation, grain growth and further grain coarsening processes. The final grain size is strongly dependent on the temperature, time and of course on the cold worked state. For higher strained materials, the nucleation density is much higher and this reduces the recrystallized grain size.
In the case of dynamic recrystallization a critical stored energy level will be reached during deformation. Therefore a new grain originates at existing grain boundaries or at microstructural heterogeneities created during the deformation (e.g. deformation bands, twins, subgrain-boundaries, inclusions) and grows. Further deformation hardens the recrystallized grain and reduces the driving force for grain boundary migration. The new grain stops to grow when the driving force remains zero or a new grain will be nucleated. If a new grain is nucleated the necklace structure, as shown in Fig. 1.1 (a) to (d), will be formed.

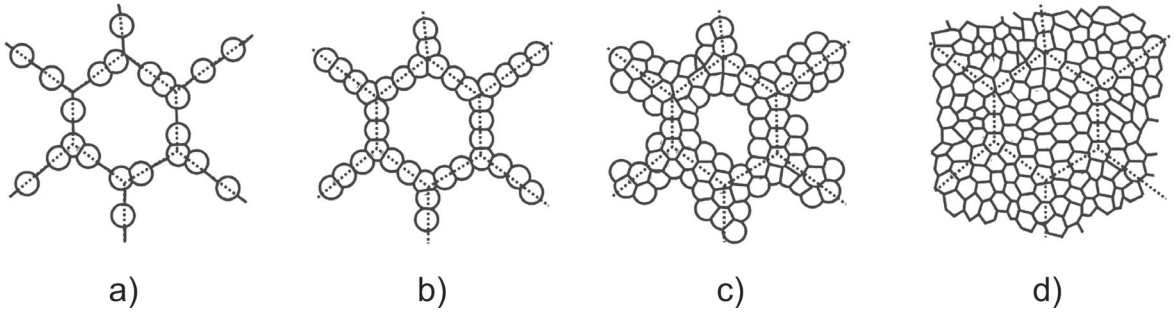

Figure 1.1.: Schematic illustration of a dynamic recrystallization process. Necklace structure is formed from (a) to (d). The initial grain is marked by dotted lines. Image was taken from Humphreys and Hatherly.[4]

The size of a dynamically recrystallized grain shows a strong dependency on the forming condition, the deformation temperature and strain rate. In connection with the nucleation process, grain boundaries are the most preferential sites to form a new grain. For the formation of a nucleus, grain boundary serration, bulging on the size of a nucleus, as well as grain boundary sliding and annealing twinning are named as essential steps.[7–11]
For the sake of completeness, it should be mentioned that dynamic recrystallization mechanisms exists which differs from the discontinuous dynamic recrystallization (DDRX) in terms of nucleation and growth. The mechanisms of geometric DRX and rotation DRX are classified by the term continuous dynamic recrystallization (CDRX) and they are described elsewhere.[4]
This thesis is clearly focused on microstructure evolution during a warm forming process. Therefore, the investigation is based on dynamical softening processes DRX and DRV. Metadynamic or static softening was not considered in this work.

1.2. Motivation and aim of the present work

The aim of the current work is to better understand the grain refinement process of coarse grained microstructures during the warm forming process. This is an important question for the metal forming industry, in order to produce high quality materials from cast structured ingots. A cast structured state with improvable mechanical properties is existent after the remelting process. This is a process widely used in industry for the production of high-quality steels, superalloys and titanium alloys. To obtain refined and uniform microstructures in metals without phase transformations (Ni, Cu, Al, γ-iron), it is necessary to understand both deformation mechanisms as well as recovery- and recrystallization phenomena. In this study special attention has been paid to investigate the deformation microstructure with local strain analysis and orientation measurements on the scale of a nucleus of a new grain. The origination of structural heterogeneities, known as potential nucleation sites in crystals with a low grain boundary fraction, is of great importance for the refinement process. Therefore, the evolution of the microstructure is determined by the discrete nature of deformation due to dislocation processes and cannot be described by continuum plasticity models, which can only capture the macroscopic point of view. To get insight into the structural fragmentation process, the influence of the grain-grain interaction, the grain boundary density and the sample geometry on the structural evolution process were studied in detail.
In the last decades a large number of investigations on the microstructural evolution at elevated temperatures were done. Most of the experimental findings were based on light microscopy and transmission electron microscopy observations, being aware that studying onset of dynamic recrystallization phenomena in coarse grained structures, considering stored deformation energy, may hardly be realized with these methods. The orientation imaging microscopy (OIM) opens access to new insights in the nucleation process of grains and provides, in combination with local strain measurement, an efficient tool for studying crystal plasticity on the macroscopic scale.

2

Summary and discussion of the results from the thesis

In this chapter the most important results of the thesis (Publications A to E), are presented and discussed:

- effect of deformation parameter and initial grain size on the microstructural evolution of pure nickel and austenitic stainless steel;
- influence of the alloying content on the microstructural evolution;
- evolution and computational description of intragranular deformation heterogeneities: potential and limits of crystal plasticity finite element analyses.

Based on these findings, consequences on structural refinement of corse structured material, e.g. pure nickel and austenitic stainless steel Böhler A220 are discussed and an outlook for an efficient refinement strategy is given.

2.1. Effect of deformation parameter and initial grain size on the microstructural evolution of pure nickel and austenitic stainless steel

The work of this thesis was performed with the model material pure nickel and a technical austenitic stainless steel grade A220 produced by Böhler. The stainless steel is a single phase fcc steel, which has a similar composition to steel grade 316L. The chemical composition is given in Table 2.1.

Material	T_m (°C)	Fe	Cr	Ni	Mo	Mn	Si	N	C
Nickel	1453			99.99					
A220	1420	63.2	17.5	14.5	2.7	1.7	0.3	0.07	max. 0.03

Table 2.1.: Melting point and chemical contents (in wt%) of pure nickel and austenitic stainless steel Böhler A220.

The influence of initial grain size on the structural refinement process was investigated by compression tests. The specimens are deformed at a constant temperature of 25°C, 0.42 $T_m\,(K)$ (only for nickel) and 0.64, 0.74, 0.84 $T_m\,(K)$ (for both materials), with a constant cross-head speed of 5 mm/min ($\dot{\epsilon} \approx 0.01\,s^{-1}$) or 50 mm/min ($\dot{\epsilon} \approx 0.1\,s^{-1}$). For example, for a 60% strained compression test sample the given strain rate $\dot{\epsilon}$ varied from about 70% (at the beginning of deformation) to 130% (at 60% deformation) of the average strain rate. The forming conditions temperature T and strain rate $\dot{\epsilon}$ are described by a single parameter, the Zener-Holloman parameter Z

$$Z = \dot{\epsilon} \cdot exp(Q/RT), \tag{2.1}$$

where Q is the activation energy for warm forming and R the universal gas constant. For the experimental details, see Publications D and E.

2.1.1. Pure nickel

Polycrystalline nickel with different starting grain sizes d_0 of 240 μm and 770 μm was deformed in compression in the temperature range from 25°C to 1180°C (T_h=0.84). From microstructural investigations it can be seen that the main forming mechanism is dislocation slip from ambient- to hot forming temperature. Therefore, the strain hardening is determined by the generation and annihilation of dislocations. The deformation experiments resulted in cold-working stress-strain curves at lower forming temperatures and a typical warm forming stress-strain response at elevated temperature, see Fig. D.3 (a) and Fig. D.4. For the warm forming experiments, the occurrence of a peak stress, a slight stress drop and a steady state region indicates that the microstructural instability of "dynamic recrystallization (DRX)" was reached. The deformed microstructures were consumed by the formation of new grains, thus minimizing the entire energy of the material. Generally, for a lower Zener-Holloman parameter Z, a reduced flow-stress and a shift of the peak strain and -stress to smaller values was observed.
The experimental results, presented in Fig. D.9 b) and Fig. D.12, show that DRX in nickel is a discontinuous process. From the microstructural point of view, new grains were nucleated during the deformation step and grew to a critical strain-hardened state and the well known necklace mechanism operated. For the first necking of recrystallized grains the initial grain boundaries act as potential nucleations sites. In the coarser grained material intragranular nucleation at deformation heterogeneities also took place.
For the formation of a nucleus at potential nucleation sites, the grain boundary motion must be taken into account. In the initially finer grained material (d_0=240 μm), see Fig. D.9 b) the grain boundary serration and bulging has the same scale compared to the size of a nucleus of a new grain. In contrast, in the coarser grained material (d_0=770 μm), the grain boundary displacement is already present but without the necessary waviness to form a nucleus. The differences in grain boundary motion seem to result from the grain size dependency of the acting deformation mechanism, see Fig. D.9 a). In the coarser grained material the forming compatibility is fulfilled by an intragranular structural fragmentation process. In finer grained structures a higher density of geometrically necessary dislocations are stored per unit volume to achieve strain gradients at grain boundaries. Therefore, in finer grained structures the areas of highest stored energy are close to the grain boundary, whereas in coarser grained materials the stored energy is in general lower and located at intragranular crystal orientation fragments. Taking into account that an increase of grain size reduces the density of potential nucleation sites and the stored energy, the difficulties in DRX process, as reported by several authors,[12–20] are understandable. This leads to a retarding and a slowing down of the DRX kinetic and a shift of critical strains and -stresses, see flow curves Fig. D.4. However, that

allows one to conclude that coarser grained materials must deformed to higher strains to reach the critical energy levels at potential nucleation sites.
From the microstructural point of view, these difficulties in DRX process end up in a partly recrystallized microstructure for the 770 μm grained material and in a nearly fully recrystallized microstructure for 240 μm grained material, see inverse pole figures (IPFs) in Figs. D.6 (a),(d) and D.7 (a),(d). The decrease of the Zener-Holloman parameter Z, presented in Figs. D.6(b-c,e-f) and D.7(b-c,e-f), leads to a fully recrystallized microstructure for all the different materials. The slight multipeak flow behavior observed for the coarser grained structure at the lowest Z value (T=1180°C and $\dot{\epsilon} \approx 0.01\,s^{-1}$), indicates a high synchronization of the DRX process and therefore clearly shows that nucleation is a time consuming process and the density of new grains is certainly a function of temperature and strain rate.
In contrast to the observation of Sah et al.[12], who reported that in nickel, the steady state DRX grain size occurs after few percent recrystallization, a meta-stable grain DRX grain size was observed. The coarser, initially 770 μm grained material was refined to a metastable DRX grain size $D_s^{'}$ smaller than the steady state grain size. For the 240 μm grain sized material the microstructural steady state seems to be nearly reached, see IPFs in Figs. D.6 and D.7. In misorientation path plots of Fig. D.14, a clear correlation of the intragranular orientation changes with the metastable DRX grain size was found. Therefore, the pronounced crystal fragmentation restricted the growth process of a DRX grain and before the steady state grain size could be reached, a new grain was nucleated, see Fig. D.14. From deformation experiments at lower Z parameter, the influence of initial grain size on DRX grains diminishes. Owing to a more homogeneous deformation, weaker orientation gradients allow the unrestricted growth to the final stable state grain size, see Table D.1 and grain size distribution in Fig. D.8.
As mentioned above, grain boundary density and mobility has a strong influence on the DRX behavior. From flow curves analysis, represented in Fig. D.3, an anomalous grain size effect was found. For deformation smaller than the critical strain, the coarser grained material showed a higher flow stress and hardening in the temperature range from 450°C (0.42 $T_m\,(K)$) to 1000°C (0.74 $T_m\,(K)$). For strains $\epsilon < \epsilon_c$ DRX acts to a minimal extent and therefore an additional grain size dependent softening mechanism must cause the decrease in work hardening. Strain induced grain boundary migration (SIBM), proposed by Angella et al.[21] for an austenitic stainless steel, describes the unusual hardening behavior in this work for nickel. In finer grained material the softening process due to the higher grain boundary density and therefore the higher affected volume is stronger than in the coarser grained material. Decreasing the forming temperature minimizes the mobility of grain boundaries and SIBM works in a minimal extent. For the highest forming temperature of 1180°C (0.74 $T_m\,(K)$) softening is dominated by dynamic recovery, (for strains $\epsilon < \epsilon_c$) and SIBM plays a minor role.

2.1.2. Austenitic stainless steel

To study the the influence of grain size in a high alloyed material Böhler A220, different initial grain sizes D_0 of 16, 26, 120, 205 μm (globular shape) and a cast material with mm-sized grains (columnar structured) were deformed. At ambient temperature, dislocation slip and mechanical twinning are the main deformation mechanisms of the high alloyed steel, see Fig. A.6. For elevated forming temperatures, the deformation mechanism changes to pure dislocation slip. Owing to extensive dynamic recovery and recrystallization, the onset stress for mechanical twinning cannot be reached at warm- and hot forming temperatures. The stress strain behavior of the finer grained materials clearly represents the change from cold

working to warm forming flow curves at the lowest Zener-Holloman parameter Fig. E.1. For an increase in starting grain size, as well as a higher Z value, the microstructure is stabilized and therefore the softening mechanism dynamic recrystallization is retarded and weaker, see quantitative analysis in Fig. E.6.

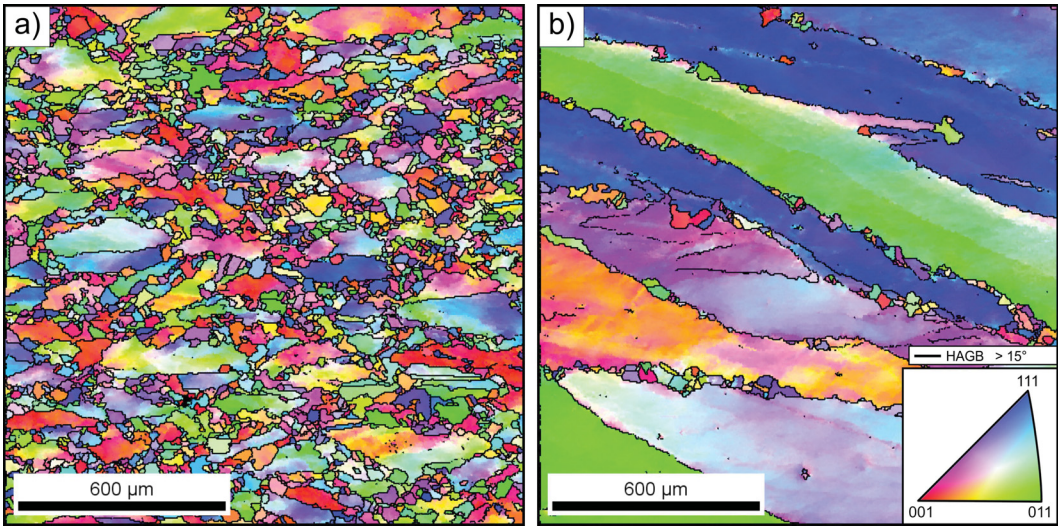

Figure 2.1.: IPF maps transversal to the compression direction of austenitic steel Böhler A220, 57% strained at $0.84\,T_m$ and an $\dot{\epsilon} \approx 0.01\,s^{-1}$: (a) nucleation at grain boundaries and operating necklace mechanism (starting grain size of 205 μm), (b) nucleation at present grain boundaries and intragranular structural heterogeneities, which are formed during the deformation process (initial cast state); high angle grain boundaries are marked as black lines.

As shown in IPF maps in Publication E and in Fig. 2.1 new grains are nucleated at present high angle grain boundaries and additionally at intragranular structural heterogeneities, which are formed during the deformation process. In accordance with the literature,[5,6,8–11] pronounced recovery, grain boundary migration and in the majority of cases annealing twinning are the essential steps for the onset of DRX. Decreasing the grain boundary density lowers the average misorientation (Fig. E.6) in the material and therefore slows down the dynamic recovery process at grain boundaries necessary for mobilization of grain boundaries. Forming at higher Zener-Holloman parameter enhanced the average misorientation but reduces all thermal activated processes, which are necessary to form a nucleus. These points illustrate the influence of grain size and forming parameter on the nucleation process of new grains.
For an increase in starting grain size the intragranular fragmentation process is stronger. The stored deformation energy in the material is clearly higher at lower forming temperatures, but the formation of mobile subgrain boundaries by dynamic recovery, which promotes DRX, is easier at higher forming temperatures and lower strain rates, see IPFs in Fig. E.3. These observations show an opportunity to refine cast structures by combined forming process, see refining strategies in Publication E.

2.2. Influence of the alloying content on the microstructural evolution under consideration of initial grain size

The main softening mechanisms of metals at high forming temperatures are dynamic recovery and dynamic recrystallization. In materials with a medium to low stacking fault energy (SFE), the recovery process is more difficult due to the reduced node detachment, climb and crossslip of dissociated dislocations. The lower dynamic recovery rate turns into higher stored energy states and this clearly promotes dynamic recrystallization.[1–4]

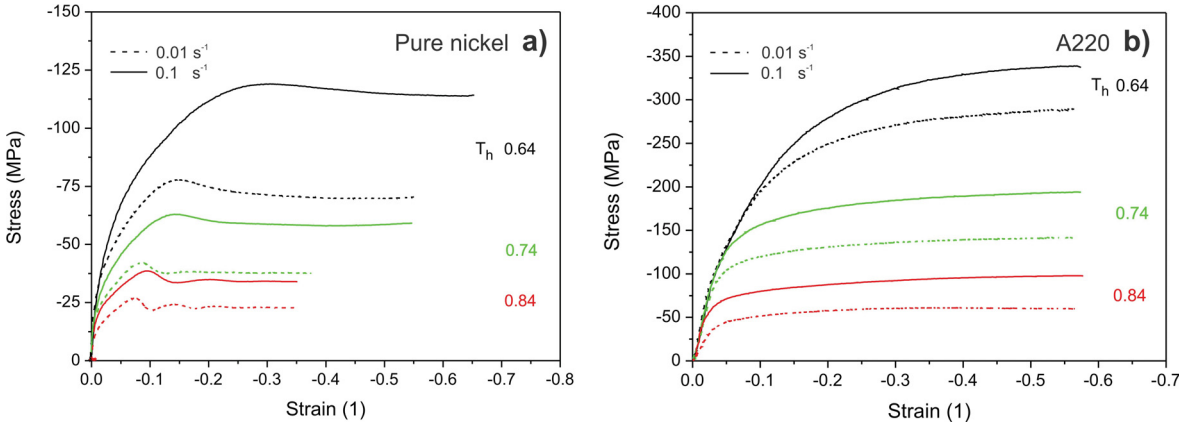

Figure 2.2.: Stress-strain cruves of pure nickel, initial 240 μm grain size (a) and austenitic stainless steel Böhler A220, initial grain size 205 μm (b), deformed at 0.64, 0.74 and 0.84 T_m with an $\dot{\epsilon} \approx 0.01\,s^{-1}$ and $\dot{\epsilon} \approx 0.1\,s^{-1}$.

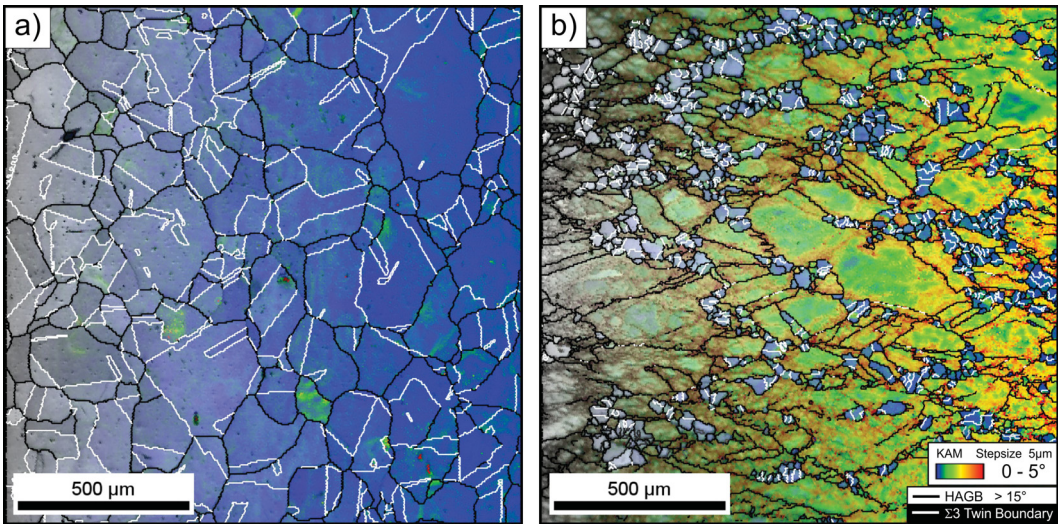

Figure 2.3.: Image quality maps faded wit kernel average misorientation (KAM) of pure nickel with a starting grain size of 240 μm after 34% deformation (a); austenitic stainless steel Böhler A220 with a starting grain size of 205 μm after 57% deformation (b). Both materials were deformed at 0.84 T_m and a strain rate of $\dot{\epsilon} \approx 0.1\,s^{-1}$. High angle grain boundaries (black) and twin boundaries (white) are indicated. The kernel average misorientation (KAM) is derived from Equation D.1. The kernel point contains information on the average misorientation of the perimeter at a radius of twice the step size.

Both investigated materials can be classified in the low to medium stacking fault regime, but they have certain differences in the SFE. The SFE of pure nickel and the austenitic stainless steel are $120\,mJ/m^2$ [22] and about $28\,mJ/m^2$ [23,24], respectively. The high alloying content of the austenitic stainless steel of 36.8 wt% should enhance the tendency to dynamically recrystallize, however it lowers the recrystallization rate due to difficulties in nucleation process of a new grain. Stress-strain curves of pure nickel and austenitic stainless steel, with nearly the same initial grain size of about $200\,\mu m$ show strong differences in the recrystallization kinetic, see Fig. 2.2. The higher hardening at the beginning of deformation experiments indicates that the austenitic material undergoes a lower recovery compared to pure nickel. However, for higher plastic strains the shape of the flow curves illustrates the weaker DRX tendency of the austenite. Therefore, the austenitic steel must be deformed at higher forming temperatures to induce typical hot forming behavior. According to the mechanical observations, forming at T_h of 0.84 with an $\dot{\epsilon} \approx 0.1\,s^{-1}$ leads to a partially recrystallized microstructure in the austenite, whereas pure nickel fully recrystallizes, see Fig. 2.3. This weak tendency of the austenitic steel to recrystallize is based on difficulties in the formation process of a new grain. The high onset stress and strain before nucleation starts, as well as the pronounced misorientation, see Fig. 2.3, pointed out the extensive microstructural stability of the austenite. For an efficient industrial refinement strategy, a double hit forming process which uses static- and dynamic recrystallization is recommended, for details see Publication E.

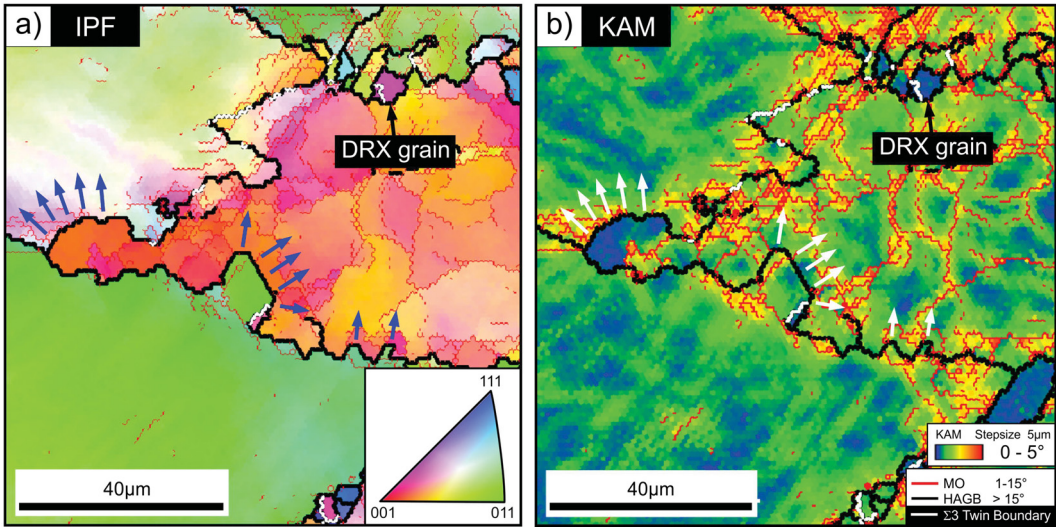

Figure 2.4.: Inverse pole figure map in compression direction (a) and KAM map (b) of austenitic steel Böhler A220 starting grain size of 120 μm; 57% strained at $0.74\,T_m$ and an $\dot{\epsilon} \approx 0.01\,s^{-1}$. High angle grain boundaries, subgrain boundaries and twin boundaries are marked as black, red, and white lines. Blue and white arrows indicates the high angle grain boundary migration.

McQueen and Jonas[3] stated in their work that there is a reduced grain boundary mobility with increasing alloying content. Whereas Prasad and Ravichandran[25] identified the formation of new moveable grain boundaries, which is slowed down due to the lower tendency to recover, to be the limiting step for DRX. Furthermore, the movement of the preexisting grain boundaries can erase the subgrain boundary before a nucleus is formed. Nevertheless both approaches regard elementary steps of the nucleation process of new grains.
The observations of the present work are comparable with the results of Prasad and Ravichandran.[25] The microstructural investigations in Fig. 2.4 of the austenitic steel, show a pro-

nounced polygonization by dynamic recovery and strong grain boundary motion of initial grain boundaries (marked with blue and white arrows). It should mentioned that plastic strains ϵ of 57% are necessary to reach the observed features in the austenite. In comparison, whenever a grain boundary underlies such an strong movement in pure nickel a new grain will easily be nucleated in this material, see Fig. D.9 b). This illustrates that the basic requirement, a movable preexisting grain boundary, is fulfilled in the austenite and the nucleation process seems to be hindered by the subgrain boundary.
The formation of a movable grain boundary is a time consuming dynamic process and clearly a function of stored deformation energy. Whenever this process is too slow, the thermally activated preexisting grain boundary moves over large distances and erases the recovered dislocation arrangement. Deformation at lower temperatures (T_h=0.74) reduces the mobility of the preexisting grain boundary (thermally activated process) and a lower strain rate delivers the necessary time to nucleate due to formation of new mobile grain boundaries. The quantitative analysis of the DRX grain fraction showed that the highest strain rate, accompanied with an higher stored energy, does not always lead to a larger DRX fraction, see material with the starting grain size of 120 μm and 205 μm in Fig. E.6. This indicates that the right choice of forming parameters for high alloyed materials is of enormous importance to make the nucleation process easier.
The effect of the initial grain size was discussed for nickel and austenitic steel previously. Based on the effect of grain size, the nucleation difficulties regarding to the high alloying content are intensified with increasing grain size. The stored deformation energy for coarser starting structures is lower and not as pronounced located at prior grain boundaries as in nickel. Additionally, the observed grain fragmentation process increases with higher alloying content. Therefore, the stored energy at grain boundaries in the austenite is lower than in pure nickel. This is based on the tendency to more planar dislocation slip for lower stacking fault energy materials. The grain boundary mobility is a function of the quantity of impurities, thus depends on the purity of the material.[26] The purity in the technical austenitic steel is certainly lower than in a pure metal. Owing to setting procedure of the starting microstructure, by static recrystallization and further grain growth, it can not fully be excluded that in coarser microstructures the pinning effects are stronger. Regarding the grain boundary impurity contents, the coarser grained materials are equivalent to technically cast structures.

2.3. Evolution and computational description of intragranular deformation heterogeneities: potential and limits of crystal plasticity finite element analyses

It is a big aim to predict the final microstructure after a hot forming process from the deformation history and the starting microstructure. This is done by using computational methods, which is a fast growing research area. Some of these simulations are growth models and use energetic approaches, without physical based modeling of the nucleation process.[27,28] When a critical energy content is reached, certain softening mechanisms act; which, in turn, determine the final microstructure. However, exact physical description of deformation processes (dislocation glide, twinning) and softening mechanisms (recovery and recrystallization) is not implemented in detail. Consequently, these models do not achieve the big aim of coupled models that implement both the calculation of deformation microstructure and accurate annealing models. This thesis shows that structural starting conditions (e.g. grain size) and forming parameters determine acting deformation processes and, consequently,

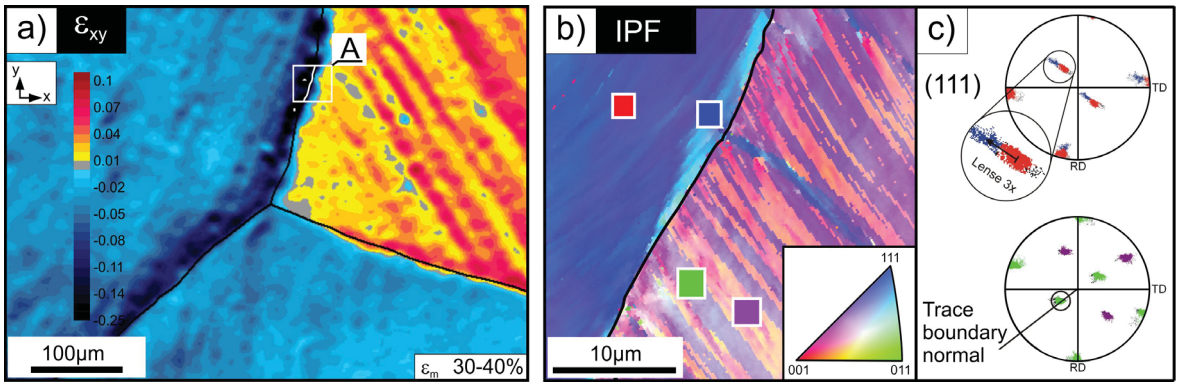

Figure 2.5.: Large strain deformation analyses inside a compression test specimen taken from Publication A, Image a) shows the local shear-strain (ϵ_{xy}) of incremental compression step from 30 to 40% macroscopic strain, the compression direction is perpendicular to the image plane; image b) shows the IPF transversal to the compression direction after 60% macroscopic deformation. The scan position is highlighted as rectangle in shear-strain map as Detail A. Image c) depicts the {111}-Pole figures of marked areas in the IPF map showing, discontinuous and continuous orientation changes. Discontinuous orientation changes are Σ3 twin related. High angle grain boundaries are marked as black lines.

the final microstructure. For example, it was observed for coarse cast structured states (Publications D and E), that intragranular nucleation becomes very relevant for DRX. This cannot be captured without detailed compilation of the microstructure.
A possibility to describe the local plastic deformation in the microstructure and the change of the local crystal orientation during the forming process is to use finite element models, based on crystal plasticity (cpFEM). These models are capable of reproducing crystal orientation changes and strain evolution during deformation. Bassani and Wu[29,30] developed the crystal plasticity model used in this work; within this model strain hardening results from slip resistance. A fact is that the stored energy is accessible on the local scale, which is especially important for intragranular nucleation appearing on deformation heterogeneities in cast structures. This offers the opportunity to test the model to see if it can depict these features. It is necessary for verification of the model to capture the deformation microstructure and the local strains experimentally and in a stepwise manner. Performing a compression split test, as it is described in Publication A, would be a good choice to follow the incremental deformation and to cross-check the results with cpFEM. Furthermore, correlations between local strains and crystal orientation changes can be made. To give an example, in the case of mechanical twinning the crystal orientation changes and the shear strain correlates well for the investigated austenitic stainless steel, see in Fig. 2.5 (a) to (c). However, for determining the model parameters that are fed into the cpFEM, it is more convenient to perform tensile tests, see Publication B. Due to friction effects between compression sample and forming die, complex stress- and strain fields appear and this complicates the determination of a material parameter set. The experimental analysis procedure consists of a combination of the measurements of the in-plane strains and the local crystal orientation during and after deformation test. The large set of model parameters was determined by minimizing the deviation of the simulated engineering stress vs. strain curves from the experimentally measured one. Doing this optimization procedure for different single-crystalline and bi-crystalline specimens ensures that the crystal plasticity framework of Bassani and Wu[29,30] can describe plasticity of the material correctly. Further details on

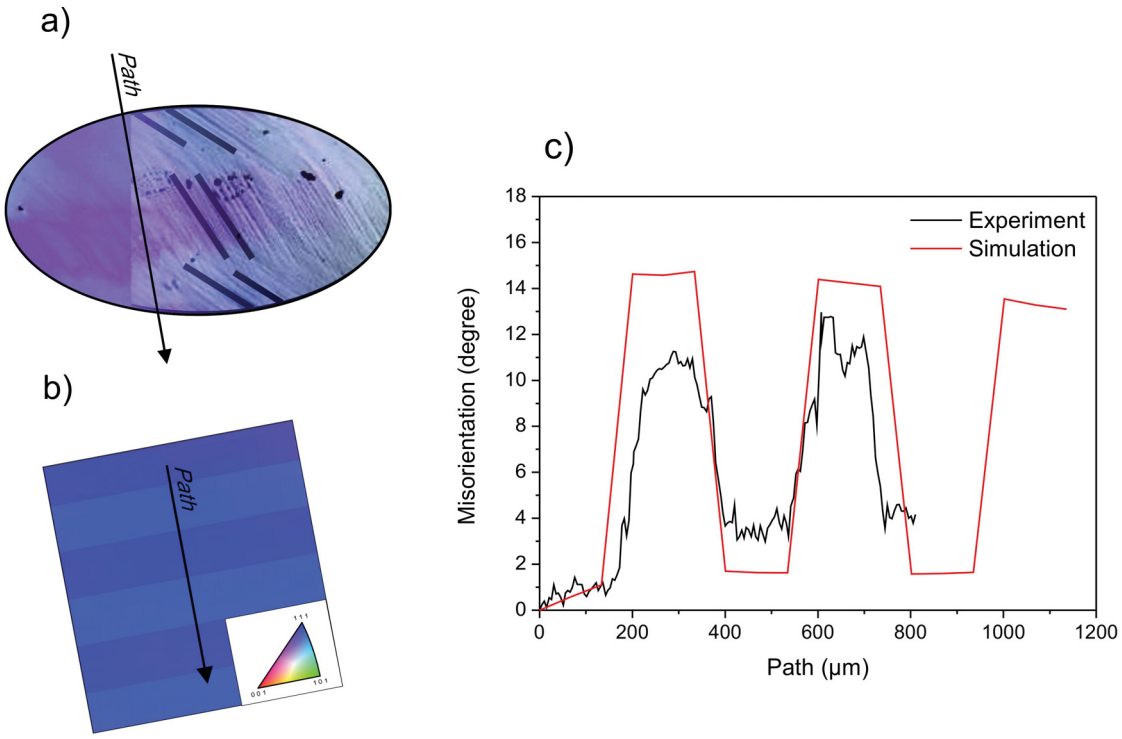

Figure 2.6.: Simulation of the crystal fragmentation process of the hard, double slip orientated crystal taken from Publication C: (a) experimental IPF; (b) simulated IPF; (c) misorientation path plots of experimental and simulated fragmentation process, paths are indicated by solid lines in (a) and (b).

model parameter determination and their quality, which is a very sensitive and difficult task, are shown in Publication C.

The influence of the forming mechanisms on microstructural evolution was checked isolated from DRX at ambient temperatures. Equal to the warm forming microstructures, continuous and discontinuous orientation changes occur during the plastic deformation. Due to different slip system activation and restrictions in the movement of dislocations (e.g. boundary conditions, sample geometry and grain boundaries) the final microstructure is determined. Hindering the movement of dislocations leads to continuous orientation changes and rigid body rotations. Such orientation changes of continuous natures are capable by cpFEM, see Publication C. In contrast, fragmentation of a crystal (Fig. 2.6 a), resulting in a lamellar structure, represents a discontinuous change in orientation and this lies beyond the capability of the cpFEM approach. The evolution of such a lamellar structure depends strongly on the activation of different slip systems, see marked slip steps in (Fig. 2.6 a). Due to the rate dependent formulation of the Schmid's law, the continuous changes of the shear stress as resulting from FE-solver will never turn off a slip system completely. However, cpFEM can be extended, by incorporating a structural length scale and selective deactivation of one slip system. As shown in Fig. 2.6 (b) and (c), the assumption reflects the experimental observation of image a) quite well. It should be mentioned here that the physical meaning of, which slip system should be switched off remains an open issue.

The present thesis demonstrates the important role of the initial and deformation microstructure on the warm forming behavior of fcc structured materials. The acting deformation mechanisms are a function of forming conditions and of the material's starting grain size. Microstructural heterogeneities (e.g. deformation bands, twins, subgrain-boundaries) which

are dependent on the deformation mechanism are created during the forming steps and act as additional potential nucleation sites to the preexisting grain boundaries. As a matter of course use of models simulating the microstructure at warm forming conditions, thermally activated softening process (DRV,DRX) must be implemented. One possibility to do so is to use a cellular automaton in the simulation, which would update the microstructural evolution due to recovery and recrystallization after each deformation increment. However, it is absolutely necessary to include these above-mentioned microstructural inhomogeneities for the correct description of break down process. The full prediction of a final dynamic recrystallized microstructure in consideration of initial and deformed state of the material is an open point. Nevertheless, the performed analyses clearly demonstrate the potential of slip resistant cpFEM to describe the microstructural evolution.

2.4. Conclusions

This thesis investigates the effects of initial grain size on the deformation behavior of different fcc structured metals. The main goal was to understand the microstructural homogenization and refinement of cast structured materials. Tests were performed on the model material pure nickel and on a technical relevant austenitic stainless steel. Different initial grain size states, in the μm- to mm range, obtained by cold rolling steps at ambient temperature of the as-received material with a subsequent thermal heat treatment as well as the initial states, were used to capture experimentally the effect of grain size on microstructural evolution. Furthermore, the potential to model the crystalline fragmentation process numerically by use of a crystal plasticity FEM model was tested.

The main forming mechanism in pure Ni is dislocation slip from ambient- to hot forming temperature. In contrast, the deformation mechanism in the high alloyed austenitic steel changes from mechanical twinning and dislocation slip at ambient temperature to pure dislocation slip at hot forming temperature. For both materials, the softening mechanisms acting at hot forming temperatures are dynamic recovery and dynamic recrystallization, whereas the intensity of each mechanism is strongly dependent on the material, the initial grain size and the forming parameters (temperature, strain rate). Any change in the grain size directly affects the stored energy per unit volume, which is a well known driving force for microstructural instability (dynamic recrystallization). Owing to the larger amount of grains in finer grained structures a higher density of geometrically necessary dislocations are stored per unit volume to achieve strain gradients at grain boundaries. Based on microstructural observations in finer grained structures, the areas of highest stored energy are close to the grain boundary, whereas in coarser grained materials the stored energy at potential nucleation sites is in general lower and more located at intragranular crystal orientation fragments. The crystalline fragmentation process is more pronounced at lower forming temperatures and coarser grain sizes.

The presented result illustrates clearly that for nickel and for the austenitic steel a coarsening in starting microstructure retards and slows down the dynamic recrystallization kinetic. These observations are explainable in terms of a nucleation problem. A coarsening in initial grain size reduces the grain boundary density and the stored deformation energy at potential nucleation sites. Therefore, it is understandable that in coarser grained structures a higher plastic strain is necessary to reach the critical values for microstructural break down. In general, new grains were formed by discontinuous dynamic recrystallization. For the finer

grained structures the initial grain boundaries, as well as triple junctions, act as potential nucleation sites. Additionally, in coarser starting structures intragranular inhomogeneities, such as deformation bands or subgrain boundaries, which originate during deformation, serve as nucleation sites. The nucleation process can be characterized by extensive grain-boundary motion and bulging on the scale of a nucleus of a new grain. In the majority of the cases annealing twinning takes part on this formation process. Alloying reduces the grain boundary mobility and despite of the reduction of stacking fault energy subgrain formation has been observed. However, the observed movement of the grain boundaries is sufficient to reduce the number of possible recrystallization nuclei. This finally results in the delayed onset of recrystallization in the alloyed state. For the first time it was shown for pure nickel that also the dynamically recrystallized grain size is dependent on the initial microstructure. Discontinuous dynamic recrystallization generates a metastable grain size, that is finer than the steady state grain size.

The evolution of intragranular crystal fragmentation (additional potential nucleation sites) is essential for the microstructural break down of very coarse grained materials. It is necessary to predict the crystalline fragmentation process to describe further on the complete recrystallization behavior. Physically based crystal plasticity models, in which dislocation slip can be handled as a plastic shear strain, were used. The crystal orientation evolution, which is strongly dependent on the initial grain orientation, sample geometry and boundary conditions and the evolution of strain gradients and rigid body rotation can be captured from the crystal plasticity model. However, the description of the substructural fragmentation process lies beyond the capability of the first model used. Slight modifications on the model by deactivation of slip systems and the implementation of a structural length scale succeed in delivering the experimentally observed substructures.

The problem with refining coarse grained materials is clearly based on a weak tendency to recrystallize. With the usage of the torsional deformation method the necessary plastic deformation energy to initiate dynamic recrystallization in coarser grained structures can be reached. For an efficient industrial forming process, a double hit forming strategy is recommended. In the first step the material is prestrained at lower temperature and recrystallizes statically. In the second step it is strained at higher forming temperature to induce dynamic recrystallization. For the described methods an excellent formability of the pre material is essential.

Bibliography

[1] D.M. Keane, C.M. Sellars, W.J. McG. Tegart, Conference on deformation under hot working conditions, Iron and Steel Institute, vol. 108, London, 1968, pp. 21-28.

[2] E. Shapiro, G.E. Dieter. Metall. Trans. 2 (1971) 1385-91.

[3] H.J. McQueen, J.J. Jonas, Recovery and recrystallization during high temperature deformation, in: Treatise on Materials science and technology, vol. 6, Academic Press, New York, 1975, pp. 393-493.

[4] F.J. Humphreys, M. Hatherley, Recrystallisation and Related phenomena, second ed., Pergamon Press, Oxford, 2003.

[5] A. Belyakov, H. Miura, T. Sakai. Mater. Sci. Eng. A 255 (1998) 139-147.

[6] C. Escher, G. Gottstein. Acta Mater. 46 (1998) 525-539.

[7] H. Miura, H. Aoyama, T. Sakai. J. Jpn. Inst. Met. 58 (1994) 267-275.

[8] S. Mahajan, C.S. Pande, M.A. Imam, B.B. Rath. Acta Mater. 45 (1997) 2633-2638.

[9] H. Miura, M. Osama, R. Mogawa, T. Sakai. Scripta Mater. 48 (2003) 1501-1505.

[10] H. Miura, T. Sakai, H. Hamaji, J.J. Jonas. Scripta Mater. 50 (2004) 65-69.

[11] H. Miura, T. Sakai, R. Mogawa, G. Gottstein. Scripta Mater. 51 (2004) 671-675.

[12] J.P. Sah, G.J. Richardson, C.M. Sellars. Met. Sci. 8 (1974) 325-331.

[13] S. Sakui, T. Sakai, K. Takeishi. Trans. Iron Steel Inst. Jpn. 17 (1977) 718-725.

[14] W. Roberts, H. Bodén, B. Ahlblom. Met. Sci., 13 (1979) 195-205.

[15] T. Sakai, J.J. Jonas. Acta Metall. 32 (1984) 189-209.

[16] M. Ohashi, T. Endo, T. Sakai, J. Japan Inst. Metals 54 (1990) 435-441.

[17] A. Belyakov, K. Tsuzaki, H. Miura, T. Sakai. Acta Mater. 51 (2003) 847-861.

[18] A.I. Fernández, P. Uranga, B. López, J. M. Rodriguez-Ibabe. Mat. Sci. Eng. A 361 (2003) 367-376.

[19] D.W. Suh, J.Y. Cho, K. Nagai. Metall. Mater. Trans. A 35 (2004) 3399-3408.

[20] A. Dehghan-Manshadi, P.D. Hodgson. Metall. Mater. Trans. A 39 (2008) 2830-2840.

[21] G. Angella, B.P. Wynne, W.M. Rainforth, J.H. Beynon. Mater. Sci. Eng. A 475 (2008) 257-267.

[22] R.J. McElroy, Z.C. Szkopiak. Int. Met. Rev. 17 (1972) 175-202.

[23] R.E. Schramm, R.P. Reed. Metall. Trans. A 6 (1975) 1345-1351.

[24] T. Magnin, C. Ramade, J. Lepinoux, L.P Kubin. Mater. Sci. Eng. A 118 (1989) 41-51.

[25] Y.V.R.K. Prasad, N. Ravichandran. Bull. Mat. Sci. 14 (1991) 1241-1248.

[26] G. Glover, C.M. Sellars. Met. Trans. 4 (1973) 765-775.

[27] A.D. Rollett, M.J. Luton, D.J. Srolovitz. Acta Mater. 40 (1992) 43-55.

[28] P. Peczak, M.J. Luton. Acta Metall. Mater. 41 (1993) 59-71.

[29] T.Y. Wu, J.L. Bassani, C. Laird. Proc. R. Soc. London A 435 (1991) 1-19.

[30] J.L. Bassani, T.Y. Wu. Proc. R. Soc. London A 435 (1991) 21-41.

3
List of appended publications

Paper A
C. Rehrl, S. Kleber, T. Antretter, R. Pippan
A methodology to study crystal plasticity inside a compression test sample based on image correlation and EBSD
Materials Characterization 62 (2011) 793

Paper B
C. Rehrl, S. Kleber, T. Antretter, R. Pippan
Experimental validation of microstructure evolution in crystalline materials
Journal of Physics: Conference Series 240 (2010) 012157

Paper C
C. Rehrl, B. Völker, S. Kleber, T. Antretter, R. Pippan
Crystal orientation changes: a comparison of crystal plasticity finite element study and experimental results
Submitted to Acta Materialia

Paper D
C. Rehrl, S. Kleber, O. Renk, R. Pippan
Effect of forming conditions on the softening behavior in coarse grained structures
Materials Science and Engineering A 528 (2011) 6163

Paper E
C. Rehrl, S. Kleber, O. Renk, R. Pippan
Warm forming of an austenitic stainless steel: the effect of grain size under different forming conditions on the microstructural evolution
Submitted to Materials Science and Engineering A

A

A methodology to study crystal plasticity inside a compression test sample based on image correlation and EBSD

C. Rehrl[a], S. Kleber[b], T Antretter[c], R. Pippan[a]

[a] Erich Schmid Institute of Materials Science, Austrian Academy of Sciences, A–8700 Leoben, Austria
[b] Böhler Edelstahl GmbH, A–8605, Austria
[c] Institute for Mechanics, University of Leoben, A–8700 Leoben, Austria

Abstract

Modified compression tests in a coarse-grained austenitic stainless steel have been carried out in order to examine the crystal plasticity behavior for large plastic deformations. The measurements of local in-plane strains provide deeper insight into the deformation process on the local scale. These measurements are performed by digital image correlation technique (DIC) in combination with local crystal orientation measurements by using the electron backscatter diffraction technique (EBSD). Split test samples are prepared to track the strong microstructural changes during deformation, which is done incrementally in 10% steps up to 60% total macroscopic strain. The clear correlation of local strains with crystal orientation changes – e.g. in the case of mechanical twinning – permits to identify the acting deformation mechanisms. Such, experimentally determined local strain maps can be used for verification of crystal plasticity finite element method simulations (CPFEM).

A.1. Introduction

Under load, the crystal anisotropy of polycrystalline metals and geometrical restrictions (grain boundaries, forming dies) cause strong inhomogeneities of stress, strain and crystal orientation changes on the micrometer-scale. Especially strain localizations and grain fragmentation during plastic deformation are of technical interest for the metal forming industry. The heterogeneities are regions of high nuclei density for phase transitions, recrystallization or starting points for damage.
In the recent years different methods to capture the plastic deformation were developed. A well-established method is the X-ray diffraction tomography which gives access to the complete strain tensor.[1–3] Furthermore the stereo imaging techniques are capable for determination of local in plane strains on free sample surfaces[4–16] or on internal surfaces of sectioned samples.[17] The local crystal orientation changes during the deformation process can be captured with the orientation imaging microscopy (OIM).
The aim of this paper is to introduce a new method to measure the local in-plane strains and local crystal orientations for large plastic strains inside a compression test specimen. This contributes to correlation of local deformation and crystal orientation changes. Furthermore the analysis provides useful data for the verification of CPFEM simulations.[6,18,19]

A.2. Preparation

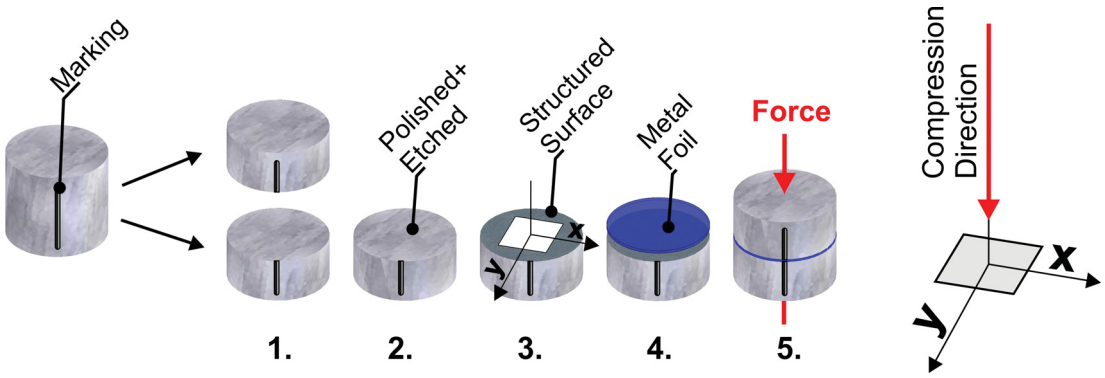

Figure A.1.: Illustration of the preparation steps 1-5 of an incremental compression test; 1) Bisection; One sample surface is polished and etched (2) marked with for example grinding paper (3); 4) sample surface is protected with an aluminium foil; 5) Combined sample parts. Scan position of strain analysis and -orientations for EBSD see coordinate system (3).

To trace the local evolution of deformation by crystal orientation, surface characteristics and local in-plane strains inside a compression test sample some modifications in comparison to a standard compression test sample are required. A schematic summary of the applied preparation steps is shown in Fig. A.1. Cylindrical standard samples with a diameter d_0 of 10 mm and a height of h_0 of 12.3 mm are used. Both end faces are mechanically ground to fulfill the requirements for a homogeneous deformation test. For an exact crystallographic assembling the split sample must be line marked at the cylindric surface before it is bisected as shown in step (1). Subsequently, in step (2) one of the surfaces is electrolytically polished and etched to remove the deformation layer from the cutting procedure and to make grain boundaries observable. To support the measurement of local strains, in step (3), a randomly distributed pattern is applied to the sample surface. Different types of surface markings, represented in Fig. A.2 are possible, whereby this list does not claim to be complete. To

achieve the necessary resolution the sample surface can be marked with a fine mist of paint or SiN (a), with SiC grinding paper imprints (granularity: P2500 and P1200) which is used in this work (b) an annealed gold coating layer (c) or a pattern produced with Ga-ions with a focus ion beam (d). Finally, in step (4) a $15\mu m$ thin, ductile aluminum foil is inserted between the assembled sample parts to protect the structured surface during the deformation test.

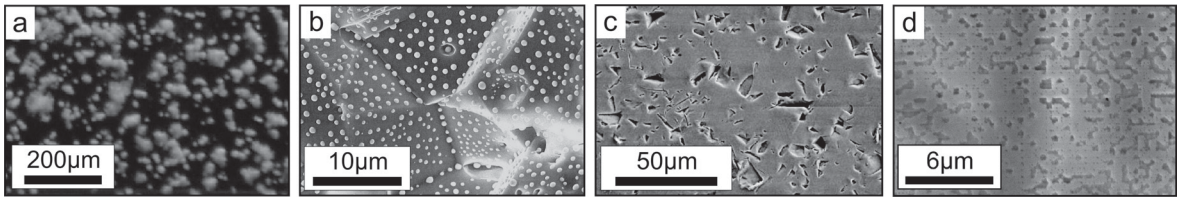

Figure A.2.: Illustration of different marking techniques. SEM micrographs of randomly distributed surface patterns for the hierarchical matching algorithms: Surface decored with boron nitride (a)[20] or gold (b),[21] imprinted with grinding paper (c) and prepared by the focus ion beam (d). Notice the different length of the micron bars.

A.3. Experimental procedure

In this work we investigate an austenitic stainless steel. The steel grade A220 produced by Böhler Edelstahl GmbH is a single phase fcc steel, which has a similar composition as steel grade 316L. The chemical composition is given in Table A.1.

Fe	Cr	Ni	Mo	Mn	Si	N	C
63.2	17.5	14.5	2.7	1.7	0.3	0.07	0.03

Table A.1.: Chemical contents (in wt%) of A220, which is very similar to 316L.

The as cast material consists of millimeter-sized columnar grains. Samples were cut out from the ingot in a way that columns are nearly parallel orientated to the compression axis. One big advantage of this arrangement is a decrease in grain boundary offset after the bisection of the sample. The samples were deformed incrementally in a uniaxial compression test by using a servohydraulic testing unit (Schenk Trebel). The experiments were conducted at ambient temperature and at a constant crosshead speed of $0.24\,mm/min$ equivalent to an average strain rate of $5 \cdot 10^{-4} s^{-1}$.
The analysis procedure consists of a combination of the measurements of the in-plane strains and the local crystal orientations. The local strains were determined by a digital image correlation, which was first introduced and developed by Davidson.[4] Using an image analysis system homologue points from high resolution SEM micrographs taken before and after each deformation step were detected. These data serve as a basis for the determination of the displacement fields (Fig. A.3) and further on the local strain calculation. In continuum mechanics the Lagrange strain tensor E can be used for a complete description of a deformation experiment. The decomposition of the tensor in a linear E_{lin} and a non linear strain gradient E_{nlin} (second-order terms) is given by

$$\mathbf{E} = \frac{1}{2}\left(\mathbf{F^T} \cdot \mathbf{F} - \mathbf{I}\right) = \mathbf{E_{lin}} + \mathbf{E_{nlin}} \tag{A.1}$$

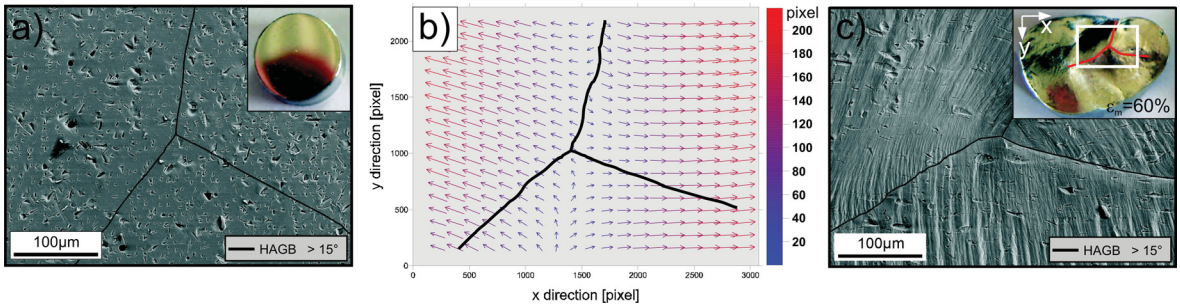

Figure A.3.: Strain analysis of A220: (a) SEM image of the marked starting microstructure, (b) displacement field as vector plot of deformation step 4 (strained from 30 to 40%), (c) SEM image of material the at a total macroscopic strain of 60%; please notice the overlayed digital images of an undeformed (a) and a 60% deformed sample part (c);

where F is the displacement gradient. For small deformation it is adequate to neglect the non-linear terms of the finite strain tensor. To use this simplification for our work, the total macroscopic strain of 60% was applied incrementally in 10% steps. From the displacement field, only the in-plane strains of the linear displacement gradients $\mathbf{E_{lin}}$ can be taken into account, illustrated by Equation (2).

$$\mathbf{E_{lin}} = \begin{pmatrix} \epsilon_{\mathbf{xx}} & \epsilon_{\mathbf{xy}} & \cdot \\ \epsilon_{\mathbf{yx}} & \epsilon_{\mathbf{yy}} & \cdot \\ \cdot & \cdot & \cdot \end{pmatrix} \tag{A.2}$$

The local strain in x-direction ϵ_{xx}, in y-direction ϵ_{yy} and the shear strain ϵ_{xy} is given by

$$\epsilon_{xx}(x,y) = \frac{\partial u_x(x,y)}{\partial x}, \qquad \epsilon_{yy}(x,y) = \frac{\partial u_y(x,y)}{\partial y} \tag{A.3}$$

$$\epsilon_{xy}(x,y) = \frac{1}{2} \cdot \left(\frac{\partial u_x(x,y)}{\partial y} + \frac{\partial u_y(x,y)}{\partial x} \right) \tag{A.4}$$

where u_x and u_y are the displacement in x- and y-direction. For details of the analysis procedure see.[14,15] The measurements on the crystal orientation were carried out with an EBSD-SEM system (an EBSD system interfaced to a LEO 1525) from the undeformed state and the final state at ϵ_m of 60%.

A.4. Results

A.4.1. Mechanical behavior

The true stress is calculated by

$$\sigma = \frac{F}{A} \tag{A.5}$$

where F is the force and A is the actual cross section. The true strain is given by

$$\epsilon = ln\frac{h}{h_0} \tag{A.6}$$

where h is the actual height and h_0 is the reference height of the sample.
In Fig. A.4, the force-strain and stress-strain curves are plotted. The deformation experiment at ambient temperature shows a typical work hardening behavior with an increase of the flow stress from 150 to 600 MPa at a strain of 60%.

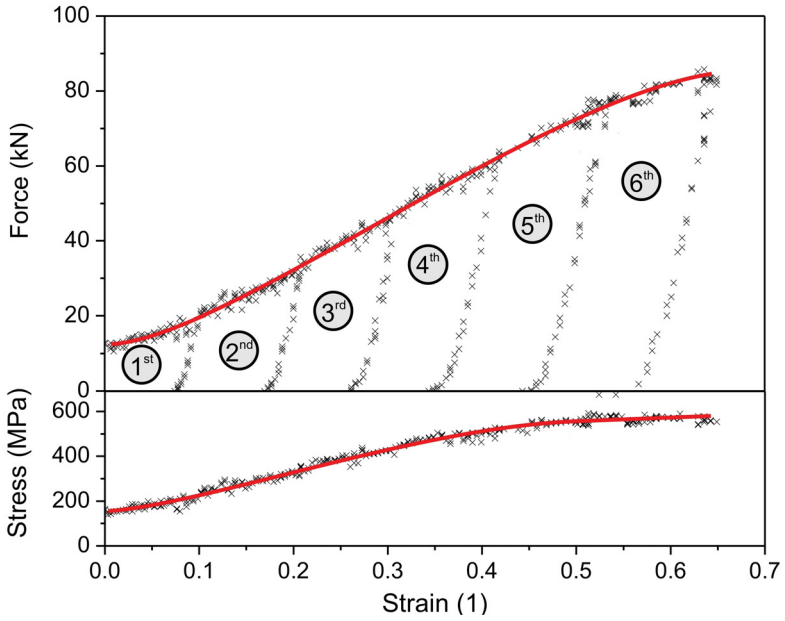

Figure A.4.: Flow behavior of an austenitic stainless steel deformed incrementally in 10% steps up to 60% total macroscopic strain. The red bold line is fitted to the overall flow behavior.

A.4.2. Local measurements of deformation

The strain maps of the compression test are shown in Fig. A.5. High angle grain boundaries with a misorientation $\geq$ 15 degree are plotted as bold black line. For a representative triple junction the local strain evolution in incremental strain steps of 10% is shown. In the present case local strains from 0 to 10% macroscopic strain could not be detected by DIC due to strong changes in the input SEM images. The unstrained state consists of imprints and the deformed state is dominated by the occurrence of slip lines which made an automatic detection of corresponding points on the deformed and undeformed micrograph impossible. Finer strain steps are required to determine these details in this state. The strain in x-direction is inhomogeneously distributed at all deformation increments. At the lowest detectable deformation increment from 10 to 20% macroscopic strains, the grain boundaries play a minor role on the arrangement of strain localization. Whereas for an increase of macroscopic strain up to 40%, a strong strain localization is present at grain boundary. For further plastic deformation the strain localizations become more pronounced and shifted into the grain interior. Surprisingly the strain in y direction is very low and sometimes negative as visualized in the strain maps in the second row. It is worth mentioning that strain localization cannot be observed in the ϵ_{yy} strain maps over the complete deformation process. In shear strain maps the appearance of heterogeneities depends strongly on the macroscopic deformation. For small plastic strain only the upper right grain undergoes a strong shearing process. A higher deformation state shows clearly an enormous shear in the vicinity of the triple junction.

A.4.3. Local crystal orientation measurements

Crystal orientation changes were captured with the EBSD-System. To correlate the local grain mechanics, scans of the initial and the final state of 60%, were taken on the same triple junction which was investigated with DIC (Fig. A.5). The EBSD data are represented as inverse pole figures (IPF) transversal to compression direction (parallel to the x direction

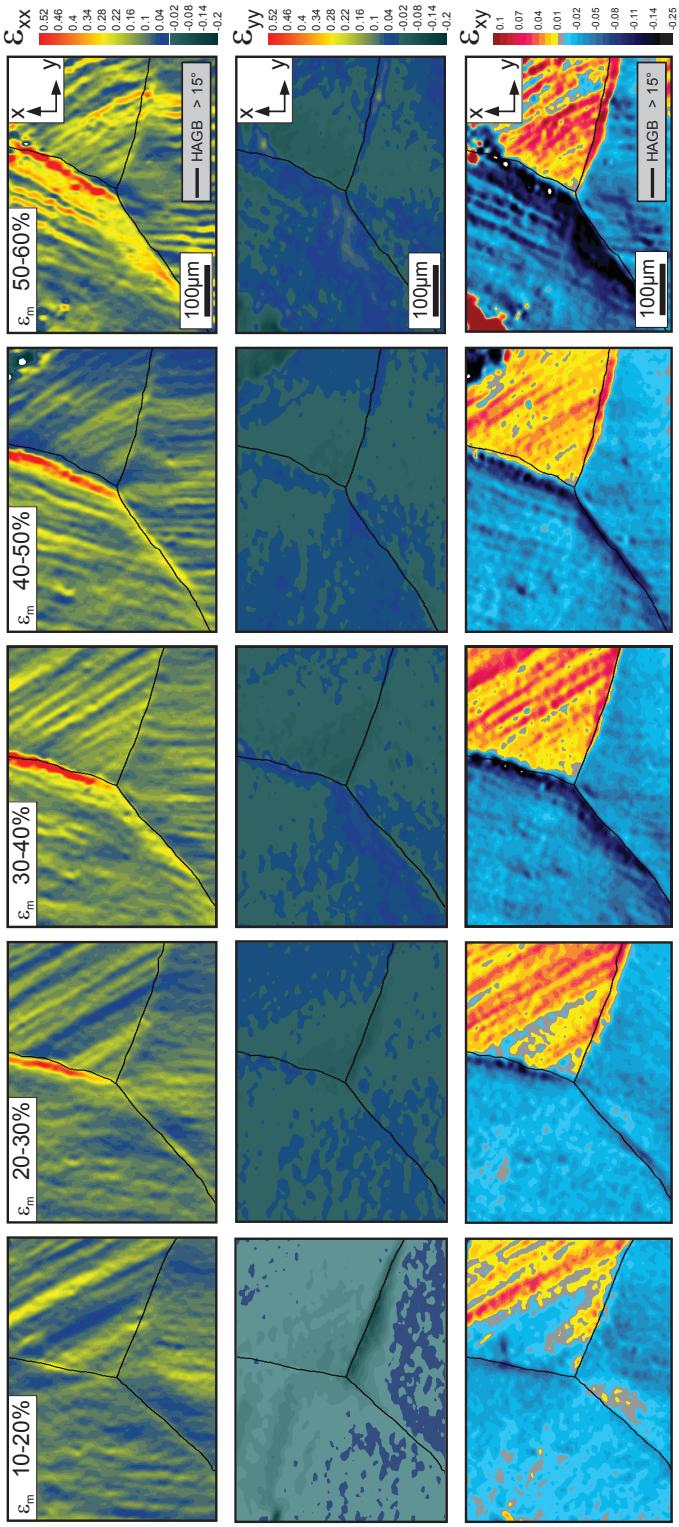

Figure A.5.: Figure 5: Local strain analysis of A220 deformed incrementally in 10% steps up to 60% total macroscopic strain. First row ϵ_{xx}, second row ϵ_{yy} and third row ϵ_{xy}; Compression direction is perpendicular to the image plane.

in the strain analysis) in Fig. A.6. The left IPF of the undeformed state shows each grain adjoining to the triple junction having a misorientation free unique orientation. After six deformation increments of 10%, strong orientation changes are present at grain boundaries and in the grain interior. A detail scan of the selected area A) and {111}-pole figures illustrate the occurrence of a continuous (red and blue squares) and a discontinuous orientation change (green and purple squares).

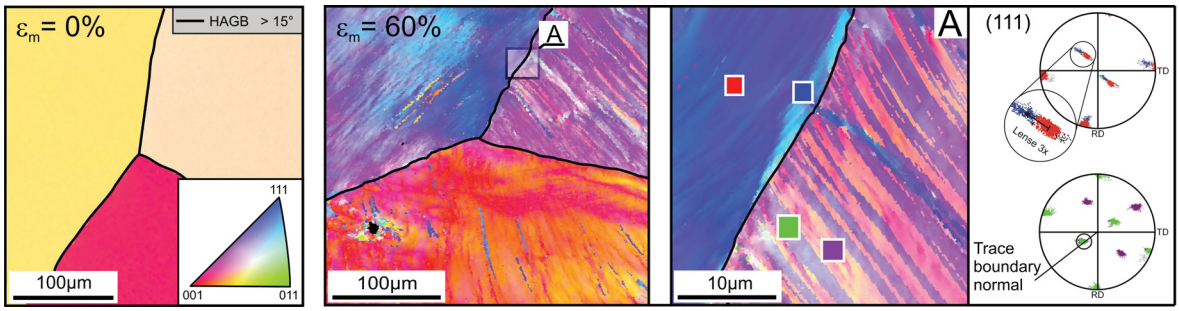

Figure A.6.: IPFs (transversal to the compression direction) of the initial state and after 60% macroscopic deformation. {111}-Pole figures of marked areas in the IPF map shows, discontinuous and continuous orientation changes. Discontinuous orientation changes are Σ3 twin related.

A.5. Discussion

In the present work a procedure to study crystal plasticity in the interior of a compression sample is introduced. During the forming experiment the deformation behavior was traced incrementally. The following discussion is organized to show the potential of the method and to clarify the deformation behavior of an austenitic stainless steel at ambient temperature.

A.5.1. Influence of the sample preparation on the deformation behavior

Effect of cutting and the alignment of sample parts

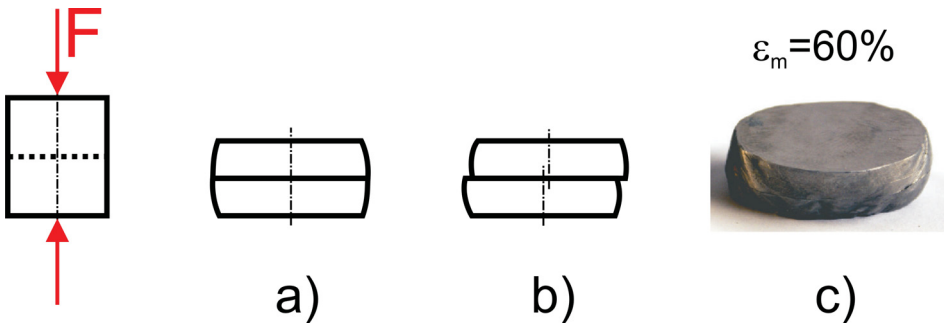

Figure A.7.: Schematic illustration of the influences of a cutting plane on the deformation process, (a) unaffected compression test (b) strong influence due to a relative movement of split sample parts; Digital image of a 60% strained compression test sample.

Fig. A.7 (a) and (b), show schematically the potential influence of the cutting plane on the deformation process. Case a) indicates typical barreling similar to that of an undivided compression test specimen. Contrary a pronounced influence of the cutting plane can be

seen in case b) as an offset of the sample contours. An individual barreling of both sample parts occurs. The experimental findings after 60% deformation shown in (c), are in strong accordance with the schematic case a) typically for a compression test sample. The influence of bisection process varied, dependent on the microstructure and the ratio of the grain size to the removed cut off layer. Grain sizes in the dimension of the width of the cut off wheel (Fig. A.8 a) lead to a strong influence of the separation step on the deformation process. As a consequence, the influence is minor for a strong difference between the coarse grain size of the material and the small cut off layer (Fig. A.8 b). The columnar grain structure used in this work has an additional positive effect in reducing the effect of the cut off layer on the local deformation behavior (Fig. A.8 c). Furthermore, the smooth stress-strain response after each deformation increment of 10% Fig. A.4 confirms that reassembling the sample parts can be performed with high accuracy.

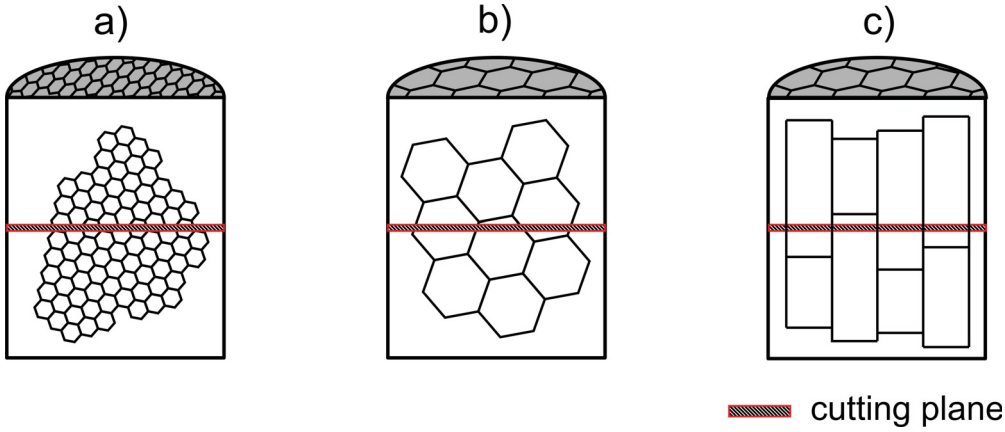

Figure A.8.: Schematic illustration of compression test samples of different initial microstructures, avg. grain size (a) in the dimension or (b) and (c) much coarser as the cut off layer; images (a) and (b) are globular grained and (c) is a columnar grained microstructure.

Determination of strain

For the determination of the strain field an algorithm from the company Alicona* was used. The digital image correlation is based on a hierarchical matching procedure, where the displacement is tracked by a randomly distributed pattern. Depending on the required resolution of the local strains different techniques to mark sample surface are possible. In Fig. A.2 the surface is a) marked with a fine mist of boron nitride,[20] b) decorated with gold,[21] c) imprinted with grinding paper and d) prepared with the focus ion beam. Important for the structuring is that it must be hierarchical and randomly distributed that means coarser objects as well as a finer substructure must be visible. This is fulfilled for all four marking techniques at different length scales. Furthermore, these techniques can be divided in nondestructive (a and b), and destructive c) and d) methods. The requirement for this work is that the markings should be visible up to 60% strain despite their direct contact with the counterpart. The imprints shown in c) are suitable. To, avoid the non detectable strain fields from the first deformation step (ϵ_m 0 to 10%), caused by a too strong change in the surface pattern due to the occurrence of slip lines, the first step should be decreased to ϵ_m of 5%. Subsequently, the same deformation increments of 10% can be used for the compression test.

* www.alicona.com

Effect of surface preparation on EBSD

The influence of these imprints used for the deformation analyses on the EBSD results has been studied and is shown in Fig. A.9. The crystal orientation of a split test sample was detected with the EBSD system, from the initial state without imprints (a), with imprints (b) and after removing a layer of 50 μm which corresponds to two times the lateral imprint dimension. Orientation data are visualized as inverse pole figures (compression direction) and grain orientation deviation maps (ODMs) from the grain average orientation. As represented in fig. 9 b) imprints produced by grinding papers of a granularity P2500 and P1200, with the dimension of 5-20 μm indicate an orientation change up to 20 degree. The orientation

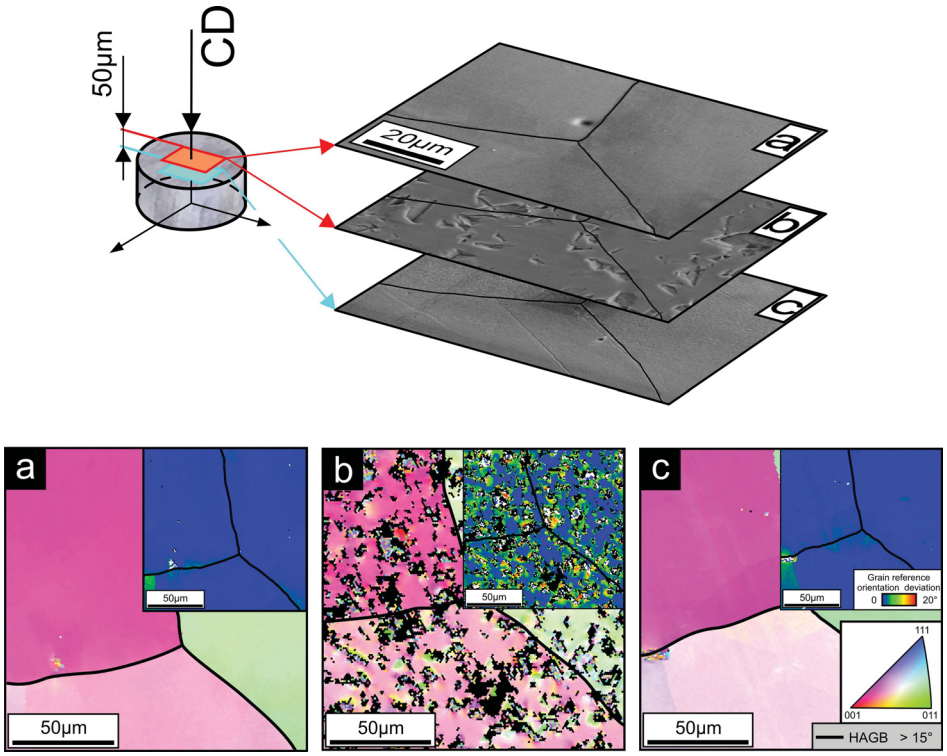

Figure A.9.: Influence of structural imprints in a split test sample on the reference crystal orientation shown as IPFs in compression direction and grain orientation deviation maps: (a) undeformed split test sample with orientation gradient free grains; (b) marked sample; (c) orientation gradients after the removement of a 50μm layer. The position of SE-scans and the corresponding EBSD-maps are shown schematically on one part of the split test sample.

deviations observed in this work are similar to what Rester et al.[22] showed in indentation experiments on Cu single crystals. From TEM observation beneath an indent, they found a higher dislocation density than in the undeformed vicinity. To locate the affected zone the imprints were removed by mechanical grinding and an electrolytical polishing process. The comparison of the ODM-maps in Fig. A.9 (a) and (c) shows clearly that the crystal orientation distribution is similar to the undeformed state a). Consequently, the influenced zone, which was hardened by imprints, was small in comparison to the sample height and can therefore be classified as insignificant for the crystal's overall plasticity behavior during the compression test. Additionally, no strain pattern like that from the imprints is visible in the local strain maps of Fig. A.5.

A.5.2. Deformation mechanism

The overlaid digital images, represented in Fig. A.3 (a) and (c) show a strong anisotropic deformation behavior. The clear change from the prior cylindrical to an elliptical shape takes place during the deformation ϵ_m to 60%. The local deformation analysis is visualized in Fig. A.5 as incremental strain maps. These maps support the observed macroscopic behavior

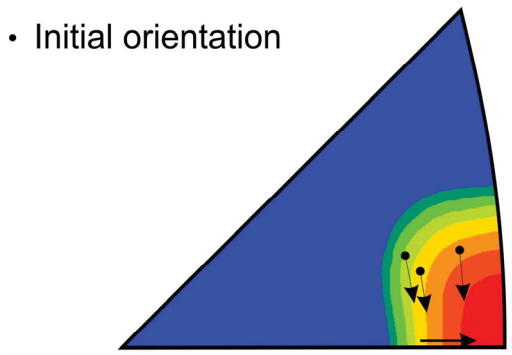

Figure A.10.: IPF in compression direction after a macroscopic strain of 60%. The initial orientation of the selected grains is marked with filled circles. Arrows illustrates theoreticall the crystal orientation change during the deformation process if a uniaxial stress state is assumed (grain to grain interactions are neglected).

with the occurrence of an extremely high x-strain and a nearly zero or slightly negative y-strain at all deformation stages. Based on the fact that a cast, coarse grained microstructure with approximately 5 grains reaching over the sample diameter (see IPF map Fig. A.10 was investigated, it is reasonable that crystal anisotropy dominates the macroscopic deformation behavior. Besides this macro observation, the methods DIC and OIM give access to the local crystal behavior inside a compression test sample even for a large plastic deformation. The authors of the paper would like to point out that the calculated in-plane strain components are not an absolute quantity. This is due to the small strain approximation on which the calculation is based, however the strain evolution is represented in a qualitative way. However, it is remarkable that macroscopic strain increments of ϵ_m of 10% lead locally to four times higher strains in x-direction as shown in Fig. A.5. The sharpening of strain localization as well as the shift into the grain interior for an increase of the macroscopic strain indicates a clear transfer of strain into non hardened regions. After a deformation of 60% the EBSD maps in Fig. A.6 show two different orientation changes. The continuous as well as the discontinuous orientation changes are based on the deformation mechanisms of crystallographic slip and mechanical twinning. From shear strain maps in Fig. A.5 it can be seen that these two different deformation mechanisms are present simultaneously from the early stages of the deformation process. It is generally accepted that the deformation mechanism of mechanical twinning can be observed by reaching a critical resolved shear stress (CRSS) similar to the Schmid law for dislocation slip.[23–25] Furthermore Christian et al. and Gil-Sevillano[23,25] reported a decrease of CRSS for twinning with increasing grain size. Thus it is obvious to find twins in coarse grained structures from the very beginning of the compression tests.
Inspite of the limitation of this method to 2D observations, it provides ideal data for accompanying micromechanical simulations, see for example.[6,18,19,26] The quality of the simulations can directly be validated by the comparison of strain fields and crystal orientation changes which are captured by DIC and EBSD. Furthermore, the access to strain and orientation data offers the opportunity to correlate deformation analyses from sample surface to the interior.

A.6. Conclusion

In this study, we presented a methodology to study large strain crystal plasticity inside a compression test sample. Based on the DIC method, the local in-plane strains were calculated and crystal orientations were measured with EBSD. Tests were performed at ambient temperatures, however it is possible to perform such tests at warm forming temperatures as well. The plastic deformation behavior of an austenitic FeCrNi-alloy at ambient temperature was observed. The physical deformation mechanism changes locally on the micrometer scale from dislocation glide to mechanical twinning. For the latter forming mechanism a clear correlation of strain analysis with the crystal orientation changes was found. Additionally, this methodology is suitable for the study of grain-grain interactions, slip system activation and grain boundary effects. For crystal plasticity FEM simulations the methodology is able to provide essential data, e.g. for the determination of model parameters or the validation of the FEM-models.

Bibliography

[1] S. F. Nielsen, H. F. Poulsen, F. Beckmann, C. Thorning, J. A. Wert, Measurements of plastic displacement gradient components in three dimensions using marker particles and synchrotron X-ray absorption microtomography, Acta Mat. 51 (2003) 2407-2415.

[2] S. F. Nielsen, F. Beckmann, H. F. Poulsen, J. A. Wert, Measurement of the components of plastic displacement gradients in three dimensions, Mater. Sci. Eng. 387-389 A (2004) 336-338.

[3] K. Haldrup, S.F. Nielsen, J.A. Wert, A general methodology for full-field plastic measurement using X-ray absorption tomography and internal markers, Exp. Menachics 48 (2008) 119-211.

[4] D.L. Davidson, The observation and measurement of displacements and strain by stereoimaging, Scanning Electron Microsc. 2 (1979) 79-86.

[5] D. Raabe, M. Sachtleber, Z. Zhao, F. Roters, S. Zaefferer, Micromechanical and macromechanical effects in grain scale polycrystal plasticity experimentation and simulation, Acta mater. 49 (2001) 3433-3441.

[6] M. Sachtleber, Z. Zhao, D. Raabe, Experimental investigation of plastic grain interaction, Mater. Sci. Eng. 336 A (2002) 81-87.

[7] D. Raabe, M. Sachtleber, H. Weiland, G. Scheele, Z. Zhao, Grain-scale micromechanics of polycrystal surfaces during plastic straining, Acta Mater. 51 (2003) 1539-1560.

[8] K. Unterweger, O. Kolednik, The local deformation behaviour of MMCs -an experimental study, Z. MetaIlkd. 96 (2005) 1063-1068.

[9] Y. Ososkov, D.S. Wilkinson, M. Jain, T. Simpson, In-situ measurement of local strain partitioning in a commercial dualphase steel, International Journal of Material Research, Z. MetaIlkd. 98 (2007) 664-673.

[10] J. Kang, M. Jain, D.S. Wilkinson, J.D. Embury, Microscopic strain mapping using scanning electron microscopy topography image correlation, J. Strain Anal. Enging. 40 (2005) 559-570.

[11] J. Kang, Y. Ososkov, J.D. Embury, D.S. Wilkinson, Digital image correlation studies for microscopic strain distribution and damage in dual phase steels, Scr. Mater. 56 (2007) 999-1002.

[12] C.C. Tasan, J.P.M. Hoefnagels, M.G.D. Geers, Microstructural banding effects clarified through micrographic digital image correlation, Scr. Mater. 62 (2010) 835-838.

[13] H. Ghadbeigi, C. Pinna, S. Celotto, J.R. Yates, Local plastic strain evolution in a high strength dual-phase steel, Mater. Sci. Eng. A 527 (2010) 5026-5032.

[14] A. Tatschl, O. Kolednik, A new tool for the experimental characterization of micro-plasticity, Mater. Sci. Eng. 265 (2003) 265-280.

[15] A. Tatschl, O. Kolednik, On the experimental characterization of crystal plasticity in polycrystals, Mater. Sci. Eng. 342A (2003) 152-168.

[16] D.P. Field, K.R. Magid, I.N. Mastorakos, J.N. Florando, D.H. Lassila, J.W. Morris Jr., Mesoscale strain measurement in deformed crystals: A comparison of X-ray microdiffraction with electron backscatter diffraction, Phil. Mag. 90 (2010) 1451-1464.

[17] J. Carroll, W. Abuzaid, J. Lambros, H. Sehitoglu, An experimental methodology to relate local strain to microstructural texture, Rev. Sci. Instrum. 81 (2010) 083703.

[18] F. Delaire, J.L. Raphanel, C. Rey, Plastic heterogeneities of a copper multicrystal deformed in uniaxial tension: experimental study and finite element simulations, Acta Mater. 48 (2000) 1075-1087.

[19] Z. Zhao, M. Ramesh, D. Raabe, A.M. Cuitio, R. Radovitzky, Investigation of three-dimensional aspects of grain-scale plastic surface deformation of an aluminum oligocrystal, Int. J. Plast. 24 (2008) 2278-2297.

[20] C. Rehrl, S. Kleber, T. Antretter, R. Pippan, Experimental validation of microstructure evolution in crystalline materials, J. Phys.: Conf. Ser. 240 (2010) 012157.

[21] H.U. Marschall. Ribrcken in Aluminiumoxid. PhD Thesis, University of Leoben, Leoben, 2001.

[22] M. Rester, C. Motz, R. Pippan, Microstructural investigation of the volume beneath nanoindentations in copper, Acta Mater. 55 (2007) 6427-6435.

[23] J.W. Christian, S. Mahajan, Deformation twinning, Prog. Mater. Sci. 39 (1995) 1-157.

[24] M.S. Szczerba, T. Bajor, T. Tokarski, Is there a critical resolved shear stress for twinning in face-centered cubic crystals, Philos. Mag. 84 (2004) 481-502.

[25] J. Gil-Sevillano, Geometrically necessary twins and their associated size effects, Scr. Mater. 59 (2008) 135-138.

[26] A. Musienko, A. Tatschl, K. Schmidegg, O. Kolednik, R. Pippan, G. Cailletaud, Three-dimensional finite element simulation of a polycrystalline copper specimen, Acta Mater. 55 (2007) 4121-4136.

B

Experimental validation of microstructure evolution in crystalline materials

C. Rehrl[a], S. Kleber[b], T Antretter[c], R. Pippan[a]

[a] Erich Schmid Institute of Materials Science, Austrian Academy of Sciences, A–8700 Leoben, Austria
[b] Böhler Edelstahl GmbH, A–8605, Austria
[c] Institute for Mechanics, University of Leoben, A–8700 Leoben, Austria

Abstract

The influence of initial grain orientation and geometrical restrictions (grain boundaries, sample geometry) on the microstructural evolution was investigated at ambient temperature. Single- and polycrystalline austenitic steel samples, strained under uniaxial tension, show pronounced orientation changes which are strongly dependent on initial orientation. The numerical simulation results from a crystal plasticity FEM model match the experimental ones.

B.1. Introduction

Under load, the crystal anisotropy of polycrystalline metals and geometrical restrictions (grain boundaries or forming dies) cause strong inhomogeneities of stress and strain and the crystal orientation changes on the local scale. Especially texture evolution and grain fragmentation during the plastic deformation are of technical interest for the metal forming industry.
A recent work[1] supported the plan to examine this structural evolution by identifying the physical processes in coarse grained crystals. With this motivation uniaxial tension tests on single (sc) and poly crystals (pc), actually a bi-crystal, were performed. The analysis was performed on a free sample surface by using EBSD-technique and stereophotogrammetric deformation analysis. Particular attention has been paid to clarify the influence of initial orientation on the structural evolution. For this study a really important advantage of coarse grained samples is the nearly columnar grain structure, which provides a bridge to validate numerical simulation results. For the simulation, a crystal plasticity finite element model was used.[2,3]

B.2. Sample preparation and experimental setup

The analysed material was a coarse pc austenitic steel, which consists of millimeter-sized grains. The chemical analysis is given in Table B.1.

Fe	Cr	Ni	Mo	Mn	Si	N	C
63.2	17.5	14.5	2.7	1.7	0.3	0.07	0.03

Table B.1.: Chemical contents (wt%) of the analysed austenitic steel Böhler A220.

Tension test samples were machined out of sheets as shown in Fig. B.1 b. The coarse grained structure makes it possible to cut out samples with a cross section of 1x1mm^2 being either sc or pc over the whole inner gauge length of 5mm (Fig. B.1 a.

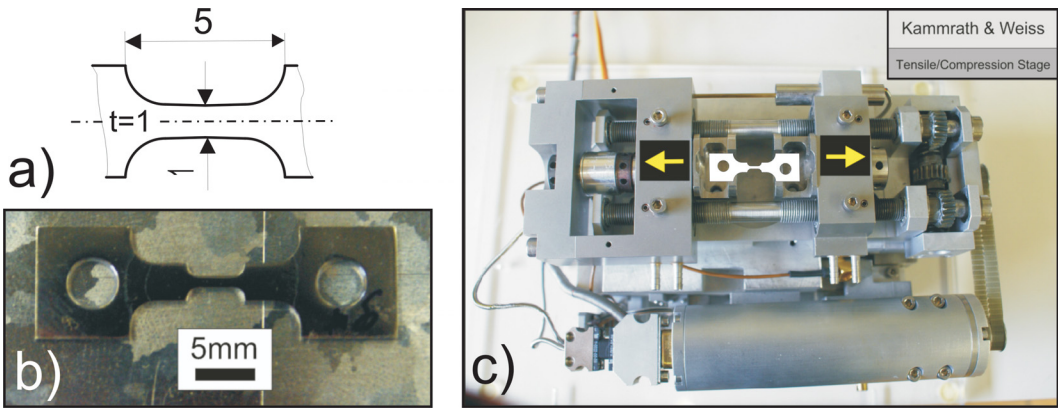

Figure B.1.: Tensile test sample fabrication out of a coarse grained sheet (a,b) and Kammrath&Weiss test unit (c) with highlighted sample position.

Subsequently, these samples were mechanically ground, polished and electrolytically polished (electrolyte A2) to remove the deformation layer from the cutting and mechanical grinding process.
The samples were deformed in an open displacement controlled mode to engineering strains of about 30% using a tension test unit (Kammrath&Weiss) as shown in Fig. B.1 c. This

equipment utilized two moveable crossheads, which held the center of the sample at a fixed position during the elongation. The experiments were conducted at a constant crosshead speed of 10μm/s and at ambient temperature.

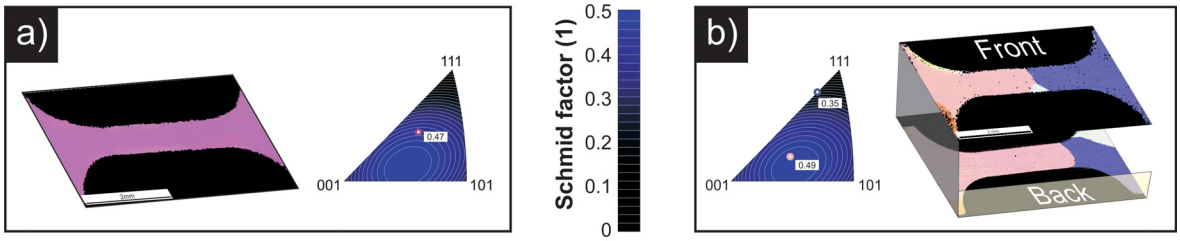

Figure B.2.: Initial Orientation of sc and pc sample in IPF Tensile test sample fabrication out of a coarse grained sheet (a,b).

The analysis procedure consists of a combination of the measurements of the in-plane strains and the local crystal orientation during and after deformation test. Measurements on the crystal orientation were carried out with an EBSD-SEM system (a TSL EBSD system interfaced to a LEO 1525). The initial crystallographic orientations and the grain boundary profile of the sc and the pc sample are plotted as Inverse Pole Figures (IPFs) related to the tension direction in Fig. B.2. The $\langle 11\,7\,20\rangle$ axis of the sc sample was parallel to the loading direction. For the pc sample the two largest grains show a soft $\langle 7\,3\,17\rangle$ and a hard $\langle 5\,5\,7\rangle$ orientation parallel to the loading direction. In-plane strains were calculated from local displacement fields by means of an in-situ stereophotogrammetric deformation analysis.[4,5] To support the measurement of the local strain, a randomly distributed pattern was applied to the sample surface by a fine mist of paint. To demonstrate the potential of crystal plasticity FEM simulations, the incremental strain in tension direction is compared to the experimental one.

B.3. Results and discussion

B.3.1. Macroscopic stress strain response

In Fig. B.3 the engineering stress vs. displacement data of the sc and pc samples are plotted. The sc sample was strained without any interruption up to an ϵ of 34%. In the case of the pc sample, the experiment was conducted incrementally in two steps to correlate the crystal orientation changes with the local strain evolution. Under normal circumstances a stage I zone is not typical for a pc sample however in our case we are analyzing a bicrystal. For both investigated samples the three hardening stages appear during the deformation. A plausible explanation for this response might be the initial crystallographic orientation and the grain boundary profile. As shown in Fig. B.2(b), the left coarse grain - having a soft single slip orientation with a Schmid factor of 0.48 - stretches over the whole inner gauge length without any grain boundary in between. In absence of constraining effects it follows that the pc sample deforms like a soft single crystal. The smaller stage I zone, the higher hardening moduli in the stage II and the more pronounced softening at stage III in comparison to the sc sample (in spite of the higher Schmid factor) is due to the constraint from the grain boundary.

B.3.2. Local microstructure evolution

Single crystalline sample

Fig. B.4 shows the crystal orientation related to the tension direction and a point to origin

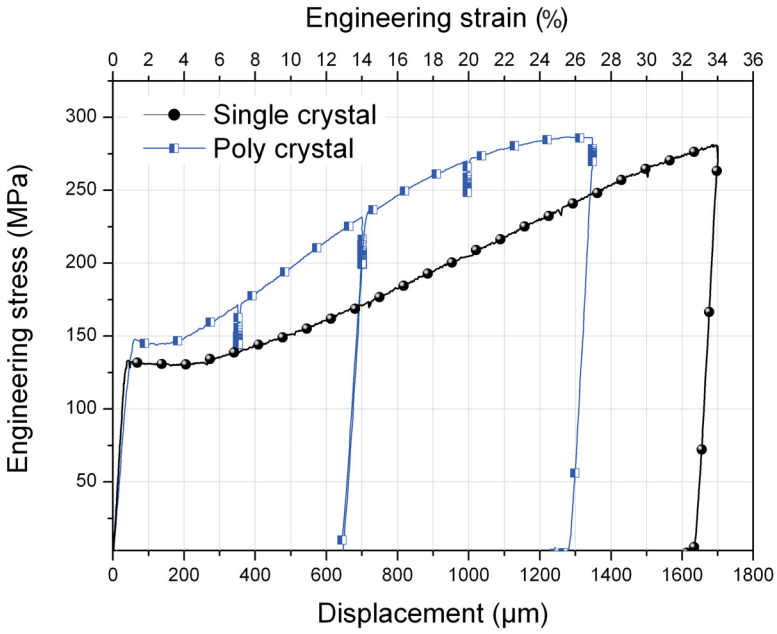

Figure B.3.: Engineering stress strain curves for sc and pc sample.

misorientation plot of the sc sample after ϵ=34%. Between the sample flanks the dislocation can move freely to the sample surface and no orientation gradient is found. Conversely, pronounced orientation changes occur at the sample flanks due to geometrical restrictions which cause a rigid body rotation of the inner area.

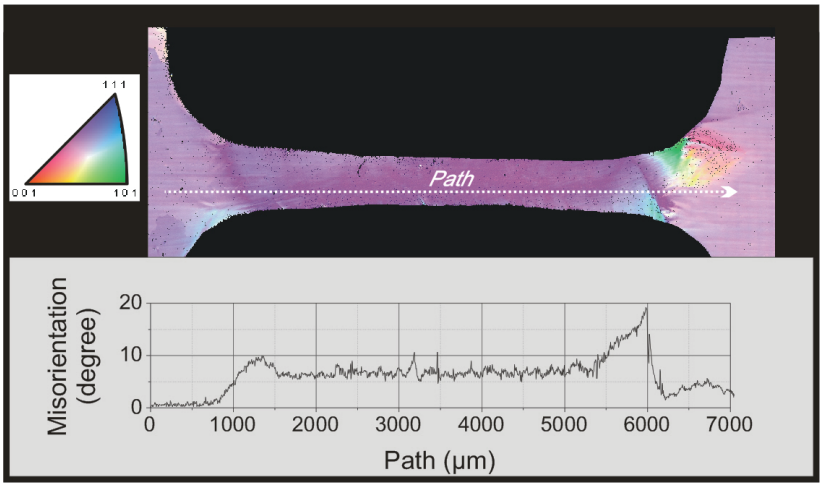

Figure B.4.: Inverse pole figure in tension direction with a point to origin misorientation plot of a 34% strained single crystalline sample.

Polycrystalline sample

As already mentioned, the strongest deformation in the pc sample is localized in the soft crystal (Fig. B.5). From comparison of incremental strain data to crystal orientation data,

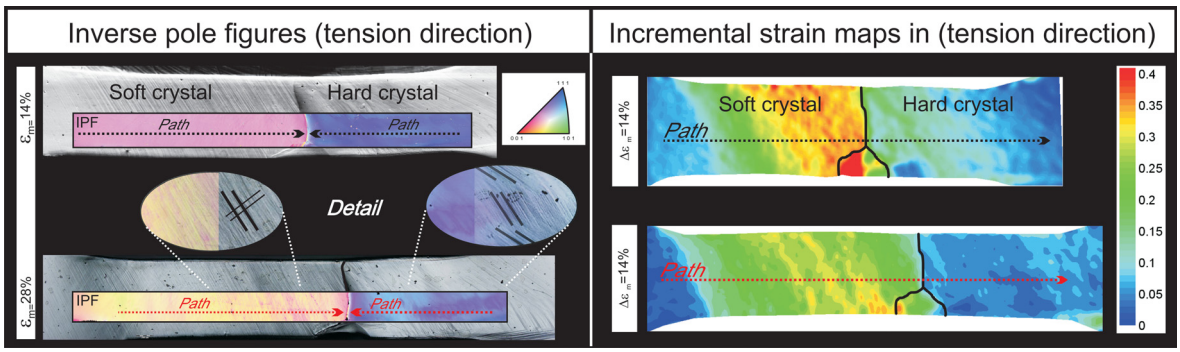

Figure B.5.: Inverse Pole Figures and incremental in-plane strain maps in tension direction illustrate the local plastic behaviour of the pc sample. The results along the paths indicated by dotted lines are compared in Fig. 6.

visualized as path plots in Fig. B.6, the following results can be presented: The first strain increment of 14% leads to a strong localization and a very heterogenous distribution of strain in the soft grain without any effect on the misorientation gradient. In spite of the small

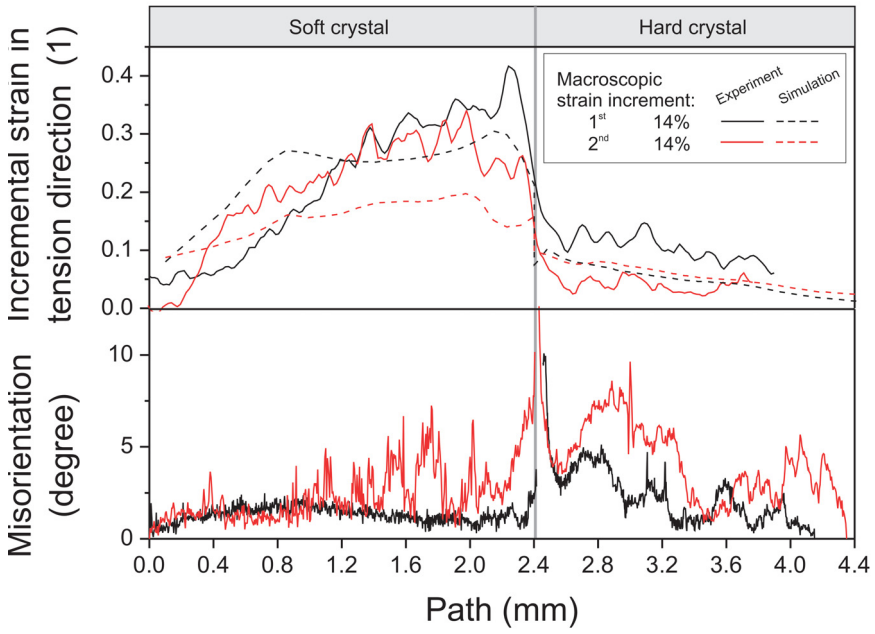

Figure B.6.: A comparison of experimentally determined and simulated incremental strain paths (dashed lines are numerical results) with misorientation paths of the pc sample. The position of the paths is plotted in Fig. 5.

strains, which appear in the hard crystal, the fragmentation process is more developed than in the soft one. With increasing ϵ the crystal fragmentation occurs in both crystals. This phenomenon motivates to investigate patterns of different slip system activation on the sample surface which are illustrated as close-up scans in Fig. B.5. A fading procedure is used to combine IPFs and digital images. In case of the soft crystal strain heterogeneities and, for

the hard crystal, different activation of slip systems cause the fragmentation process. For the soft crystal there is one major slip system with a maximum Schmid factor and, therefore, it is hard to activate a second slip system. In the hard crystal two slip systems have the same Schmid factor. That means, the resolved shear stress on each slip system is equal. As a result small orientation fluctuations or geometrical restrictions, leading to a more complex strain tensor, can favour one slip system very easily.

For the crystal fragmentation process the initial orientation has a strong influence.[6] As shown for the pc sample in Fig. B.6 the predicted local strains from the simulation model match the experimental ones.

Conclusion

Dislocation slip and shear constraints are the physical mechanisms which control the texture evolution. In double slip orientated grains, the fragmentation is more pronounced as in single slip orientated ones.

Bibliography

[1] Zhao Z, Ramesh M, Raabe D, Cuitio A.M. and Radovitzky R 2008 *Int. J Plast* **24** 2278-2297

[2] Wu T Y, Bassani J L and Laird C 1991 *Proc. R. Soc. London* A **435** 1-19

[3] Bassani J L and Wu T Y 1991 *Proc. R. Soc. London* A **435** 21-41

[4] Tatschl A and Kolednik O 2003 *Mater. Sci. Eng.* A **339** 265-280

[5] Tatschl A and Kolednik O 2004 *Mater. Sci. Eng.* A **364** 384-399

[6] Raabe D, Zhao Z and Mao W 2008 *Acta Mater.* **50** 4379-4394

C

Crystal orientation changes: a comparison of crystal plasticity finite element study and experimental results

C. Rehrl[a], B. Völker[a], S. Kleber[b], T. Antretter[c], R. Pippan[a]

[a] Erich Schmid Institute of Materials Science, Austrian Academy of Sciences, A–8700 Leoben, Austria
[b] Böhler Edelstahl GmbH, A–8605, Austria
[c] Institute for Mechanics, University of Leoben, A–8700 Leoben, Austria

Abstract

Tension tests on single crystalline and bi crystalline austenitic stainless steel samples at ambient temperature and constant crosshead speed have been carried out. To understand the limits of crystal plasticity models to predict the microstructural evolution process, simulation data were compared to experimentally observed crystal orientation evolution and strain analyses. The microstructure was captured after deformation by using electron backscatter diffraction technique (EBSD) and local strain analyses by the digital imaging correlation technique (DIC). The initial grain orientation, sample geometry, boundary conditions and high angle grain boundaries have enormous influences on the crystal orientation evolution. Strain gradients and rigid body rotation can be captured from the crystal plasticity model of Bassani&Wu. However, the description of the substructural fragmentation process lies beyond the capability of the used model. Slight modifications on the model by activation of slip systems and the implementation of a structural length scale delivers the experimentally observed substructures.

C.1. Introduction

Crystal plasticity of metals is an extensively researched field. Since Taylor[1] has introduced the dislocation concept many advances in the understanding of slip systems, work hardening[2–6] and texture evolution have been made. Based on these findings, crystal plasticity models are developed by many authors and implemented in commercial FEM environments.[7–22] Concerning the strain hardening nature crystal plasticity models can be classified in two major types. In the first type, hardening results from slip resistance, e.g.[12–16,18,19] and in the second type from an increase of the dislocation density, e.g.[20–23] The literature reports that both approaches can be used for the prediction of stresses and strains, but only models of the second type can capture the intragranular substructure evolution. The present work examines the influence of geometrical restrictions, e.g. grain boundaries and sample geometry, on the evolution of structural inhomogeneities. Tensile tests performed at ambient temperature are analyzed with local strain analysis by the digital imaging correlation technique (DIC)[24–28] and with orientation imaging microscopy (OIM)[29]. These investigations serve as basis for a deeper understanding of the underlying physical mechanism. In order to understand the limits in capturing the evolution of intragranular structures of type one models, a detailed comparison of the model from Bassani&Wu[13,14] with experimental results is performed.

C.2. Experimental procedure

The analyzed material was an austenitic steel, which consists of millimeter-sized grains. The chemical analysis is given in Table C.1.

Fe	Cr	Ni	Mo	Mn	Si	N	C
63.2	17.5	14.5	2.7	1.7	0.3	0.07	0.03

Table C.1.: Chemical contents (wt%) of the analysed austenitic steel Böhler A220.

Single-crystalline and bi-crystalline tension test samples with a cross section of 1x1mm^2 and a reduced inner section length of 5mm were machined out of sheets, see Fig. C.1. The initial

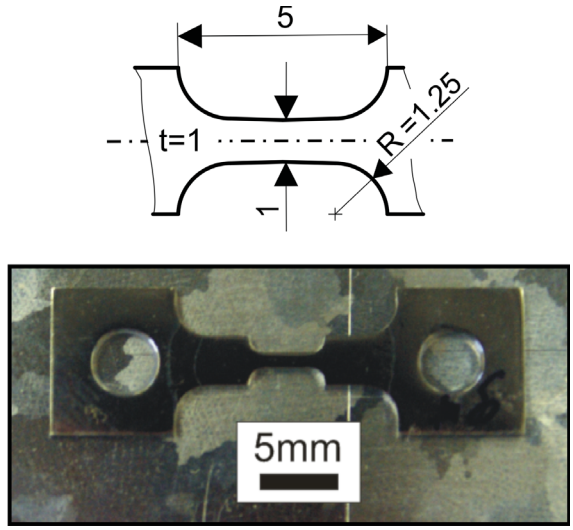

Figure C.1.: Tensile test sample fabricated out of a coarse grained sheet.

crystallographic orientations related to the tension direction and the grain boundary profile of the single-crystalline and the bi-crystalline sample are plotted as Inverse Pole Figures (IPFs) in Fig. C.2. The ⟨11 7 20⟩ axis of the soft single-crystalline sample was parallel to the loading direction. For the bi-crystalline sample the two largest grains in the reduced inner section show a soft ⟨7 3 17⟩ and a hard ⟨5 5 7⟩ orientation parallel to the loading direction.
The samples were deformed, with a constant crosshead speed of 10 μm/s, to engineering strains of about 30% using a tension test unit (Kammrath&Weiss). The experimental analysis procedure consists of a combination of the measurements of the in-plane strains[27,28,30] and the local crystal orientation during and after deformation test. For details of the surface preparation, the testing and analyzing procedure see.[30]
The FEM simulations are done on a real 3d sample geometry using 2^{nd} order tetrahedral C3D10 element meshes which are available in ABAQUS.[31] The crystal plasticity model is taken from Bassani&Wu,[13,14] implemented by Huang[32] in the user-material of ABAQUS, as described in the next section C.3. To demonstrate the potential of crystal plasticity FEM simulations, the incremental strain in tension direction and the crystal orientations after the plastic deformation are compared to the experimental one.

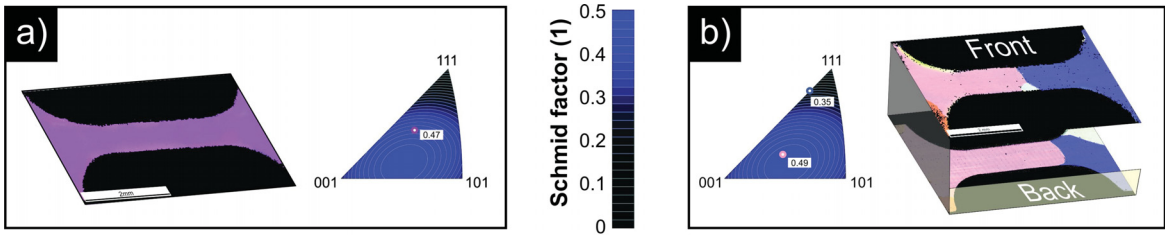

Figure C.2.: Initial Orientation of single-crystalline and bi-crystalline sample in IPF Tensile test sample fabricated out of a coarse grained sheet (a,b).[30]

C.3. Crystal plasticity model

The main physical mechanism for plastic deformation of metals at ambient temperatures is dislocation slip. The movement of dislocations is restricted to closely packed planes or directions. In the fcc case there is one set of twelve closely packed slip systems, {111} <110>. The activation of each slip system obeys Schmid's law,[33] that means the resolved shear stress on a slip system acts as driving force for the dislocation movement and slip occurs by reaching a critical value well known as Schmid stress.
In physically based crystal plasticity models, dislocation slip can be handled as a plastic shear strain. The resolved shear stress $\tau^{(\alpha)}$ on the slip system α can be calculated from

$$\tau^{(\alpha)} = \sigma_{ij}\, \mu_{ij}^{(\alpha)} \tag{C.1}$$

where σ_{ij} is the stress tensor and $\mu_{ij}^{(\alpha)}$ the Schmid tensor. According to the viscoplasticity approach of Schmid's law the shear rate $\dot{\gamma}^{(\alpha)}$ on the slip system α is a function of the resolved shear stress $\tau^{(\alpha)}$

$$\dot{\gamma}^{(\alpha)} = \dot{a}\, f^{(\alpha)} \left(\frac{\tau^{(\alpha)}}{g^{(\alpha)}} \right) \tag{C.2}$$

where the constant $\dot{a}$ is the reference strain rate, $g^{(\alpha)}$ the current strength (Schmid stress). To consider rate sensitivity in this formulation a simple power law function from Hutchinson[34]

is used

$$f^{(\alpha)}(x) = x\,|x|^{n-1} \tag{C.3}$$

where x=$\tau^{(\alpha)}/g^{(\alpha)}$. A high rate sensitivity factor n with the limit $n \to \infty$ describes a rate-independent material. The evolution of strength $g^{(\alpha)}(\gamma)$ for each slip system is given as a sum over the product at the hardening moduli $h_{\alpha\alpha}$ with the shear strain on the corresponding slip system, where $h_{\alpha\alpha}$ is the self hardening modulus and $h_{\alpha\beta}$ are the corresponding latent hardening moduli:

$$\dot{g}^{(\alpha)} = \sum_{\beta} h_{\alpha\beta}\,\gamma^{(\beta)} \tag{C.4}$$

In this work the strain hardening model of Bassani&Wu (BW)[13,14] was taken. The model was incorporated in the user material subroutine (UMAT) of the finite element solver ABAQUS[31] by Huang[32] and modified by Kysar.[35] All three hardening stages of crystalline materials can be captured by the model. For the evolution of material hardness the shear strains $\gamma^{(\alpha)}$ of all slip systems are taken into account. The self hardening moduli $h_{\alpha\alpha}$ are given by

$$h_{\alpha\alpha} = \left\{ (h_0 - h_s) sech^2 \left[\frac{(h_0 - h_s)\gamma^{(\alpha)}}{\tau_s - \tau_0} \right] + h_s \right\} G\left(\gamma^{(\beta)}; \beta \neq \alpha\right) (no\,sum\,on\,\alpha) \tag{C.5}$$

where h_0, h_s, τ_0 and τ_s are hardening moduli and shear stresses describing the easy glide of stage I. The function G associated with cross hardening is determined by

$$G\left(\gamma^{(\beta)}; \beta \neq \alpha\right) = 1 + \sum_{\beta \neq \alpha} f_{\alpha\beta} \tanh\left(\gamma^{(\beta)}/\gamma_{(0)}\right) \tag{C.6}$$

where $\gamma_{(0)}$ and $f_{\alpha\beta}$ are parameters which describe the interaction between slip systems. The amount of slip to reach the peak strength of the material is controlled by $\gamma_{(0)}$ and $f_{\alpha\beta}$ gives the interaction strength of the slip system. The latent hardening moduli are given by

$$h_{\alpha\beta} = q \cdot h_{\alpha\alpha} \quad (\beta \neq \alpha) \tag{C.7}$$

where q is a constant. For further details of the modeling, see Bassani&Wu[13,14] and Huang.[32]

The anisotropic elastic constants C_{11}, C_{12} and C_{44} were taken from the literature[36] for a 18-14 CrNi stainless steel. The inelastic coefficients in Table C.2 are identified by an optimization procedure, where the deviation of the simulated engineering stress from the experimentally measured one was minimized. This procedure was performed for different single-crystalline and bi-crystalline specimens with different crystalline orientations to ensure that a material parameter set will be determined, see Table C.2.

C.4. Results

C.4.1. Macroscopic stress strain response

The engineering stress is calculated by

$$\sigma = \frac{F}{A_0} \tag{C.8}$$

elastic constants			inelastic coefficients		
C_{11} in GPa	C_{12} in GPa	C_{44} in GPa	h_0 (MPa)	τ_S	τ_0 (MPa)
198	125	122	6000	53	38

inelastic coefficients					
h_s (MPa)	γ_0	f_0	q	$\dot{a}\,(s^{-1})$	n
14	0.3	70	0.02	0.005	10

Table C.2.: Single crystal anisotropic elastic constants of Fe 18%Cr 14%Ni alloy[36] and inelastic coefficients of the austenitic steel A220 at room temperature identified by an optimization procedure.

where F is the force and A_0 the initial cross-sectional area. The engineering strain is given by

$$\epsilon = \frac{\Delta l}{l_0} \tag{C.9}$$

where Δl is the elongation and l_0 the initial length of the inner reduced section of the sample. In Fig. C.3 a) experimental and in b) simulated stress-strain curves of single-crystalline and bi-crystalline samples are plotted. Additionally, the stress strain behavior of a polycrystalline sample was added into the diagram. In the case of the bi-crystalline sample, the experiment

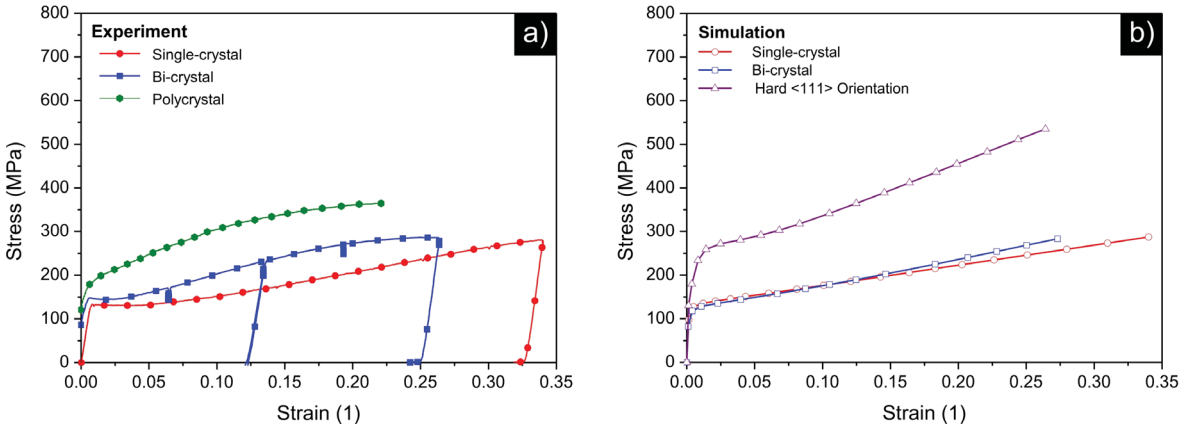

Figure C.3.: Engineering stress-strain curves of experimental (a) and simulated tension tests (b) of an austenitic steel A220. Additionally, a true stress-true strain curve of a polycrystalline sample deformed under compression is plotted in (a).

was conducted incrementally in two steps to correlate the crystal orientation changes with the local strain evolution. For the experimentally investigated single-crystalline and bi-crystalline samples three hardening stages appear during deformation. The bi-crystalline sample showed a smaller stage I zone, a higher hardening in the stage II and a more pronounced softening at stage III in comparison to the single-crystalline sample. The polycrystalline sample showed a typical hardening stage II and stage III at higher plastic strains. The simulated stress-strain curves, represented in Fig. C.3 b), indicates a higher hardening for stage II for the bi crystalline sample compared to the single-crystalline one. The hardening stages I and III could not be observed for these samples. The simulated hard $\langle 1\,1\,1 \rangle$ orientated single-crystalline sample showed the highest hardening and of course flow stress.

C.4.2. Microstructure evolution on the local scale

Single-crystalline sample

The crystal orientation of a single-crystalline sample in soft orientation, after a plastic strain of 34%, is shown as IPF-map in Fig. C.4. The observed slip lines on the sample surface illustrate that dislocation slip is the main deformation mechanism. Both, the experiment as well as the simulation showed that the inner section of the sample rotates rigidly during the plastic deformation and no orientation gradient was found. Conversely, pronounced orientation changes occur at the sample shoulders.

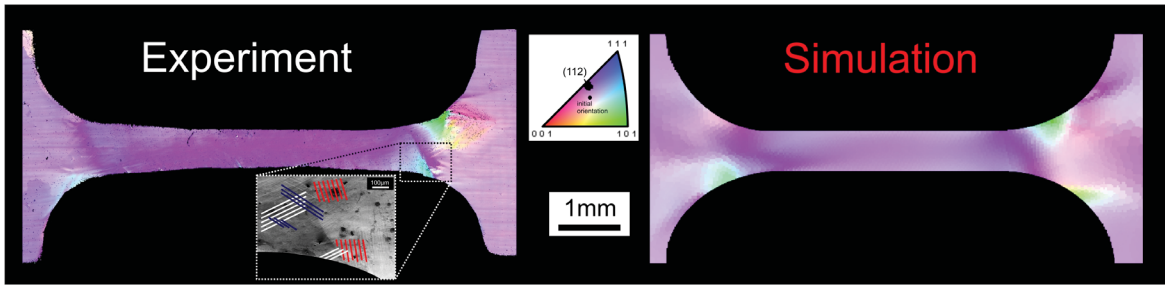

Figure C.4.: Comparison of IPFs (tension direction) of an experimental (left image) and a simulated (right image) tension tested sample in a soft orientated single-crystalline sample, ϵ=34%. The used color code, is also depicted and initial orientation and the orientation at ϵ=34% are indicated.

Bi-crystalline sample

The strain analysis in Fig. C.5a) shows the deformation behavior of the bi-crystalline sample for two incremental deformation steps. The first strain increment of 14% lead to a strong localization and a very heterogeneous distribution of strain in the soft orientated grain with only a slight deformation of the hard crystal. The second strain increment deformation is already localized in the soft grain but slightly shifted from the grain boundary to the grain interior. The experiment as well as the simulation showed nearly the same strain behavior, a small difference is that strain localizations are a little bit sharper and more pronounced in the experiment.
From the OIM analysis of the experimental sample it can be clearly seen that after the second strain increment crystal fragmentation is present in the soft grain, see Fig. C.5b). In the hard orientated crystal, the fragmentation is already present after the first deformation step. The simulated crystal orientations evolution shows more homogeneous and softer orientation change after deformation, see Fig. C.5b).

C.5. Discussion

Crystal orientation changes and the evolution of substructures during plastic deformation[37–40] are strongly dependent on the initial crystal orientation[41–43] and on the restrictions of dislocation movement. Obstacles, e.g. grain boundaries, sample geometry and the degree of freedom of the gripper impede this movement and play an enormous role on the final structure. In the following discussion, the results from crystal plasticity simulations will be validated and used to describe the experimental findings of single-crystalline and bi-crystalline tension tests. Further on, a modification to extend a strain hardening based type I model to the numerical description of the substructural crystal fragmentation will be suggested.

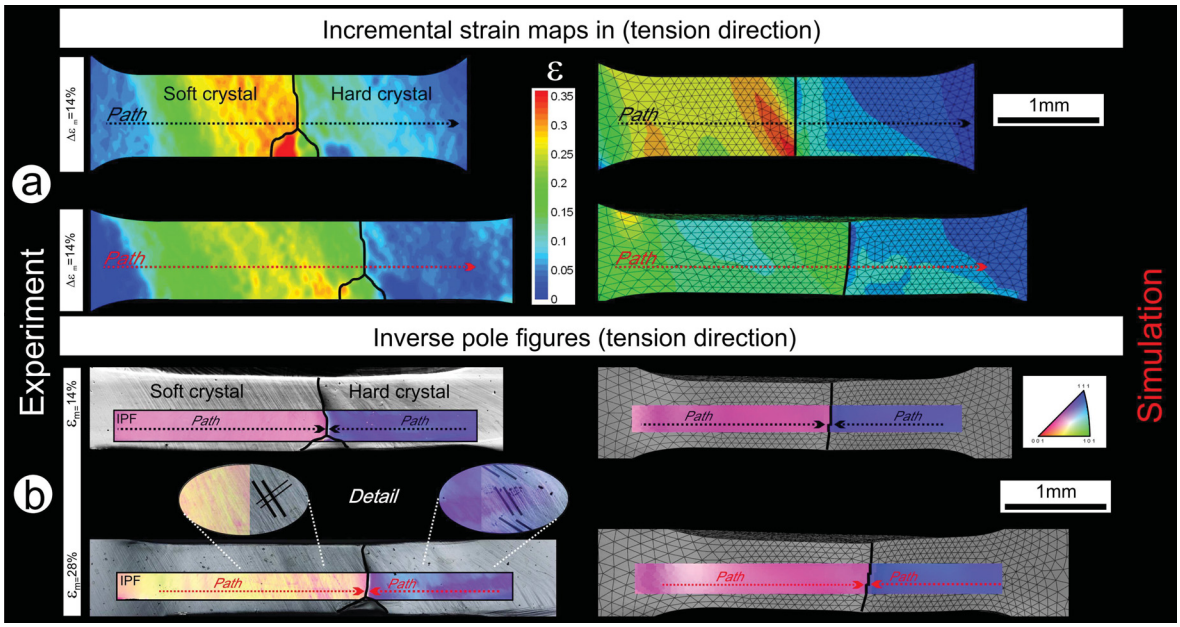

Figure C.5.: Comparison of local true strain maps (a) and IPFs in tension direction (b) of an experimental (left images) to a simulated (right images) tension tested bi-crystalline sample, ϵ=28%. The results along the paths indicated by dotted lines are compared in Fig. C.7.

C.5.1. Determination of the model parameter set

In this work, the identification of the model parameters was carried out on different crystal orientations in single-crystalline and bi-crystalline samples, respectively. This ensures that our determined set can describe the plasticity of material correctly in the framework of the crystal plasticity model of Bassani&Wu model.[13,14] The comparison of experimental to the simulated stress-strain response (Fig. C.3 a) and (b)) illustrates that the general hardening tendencies can be captured well by this model. Therefore, it is worth mentioning that a simulation of the hardest 111-oriented single-crystalline sample clearly has a higher hardening and flow stress than the experimental polycrystalline sample. The deviation in the hardening stage I illustrates that this stage cannot be reproduced correctly from the model. The slip system activation from simulation data, plotted in Fig. C.6, shows that the onset of a secondary slip system is in accordance with the experimental observation at the beginning of stage II. In spite of the correct activation of the second slip system, the stage I is not present in the simulated engineering stress-strain curves. This illustrates the complexity to find the right set of material parameters. Therefore, the small deviations appearing in the hardening stage I are acceptable; the activation of slip-systems and the overall hardening behavior of the material is described in a correct way.

C.5.2. Microstructural evolution of a single-crystalline and a bi-crystalline sample

Influence of sample geometry and the boundary condition

The experimental and the simulated IPF of a 34% strained single-crystalline tension test sample are presented in Fig. C.4. Owing to the high accordance of the simulated crystal orientations with the experimental ones, we take also the simulation results for the discussion

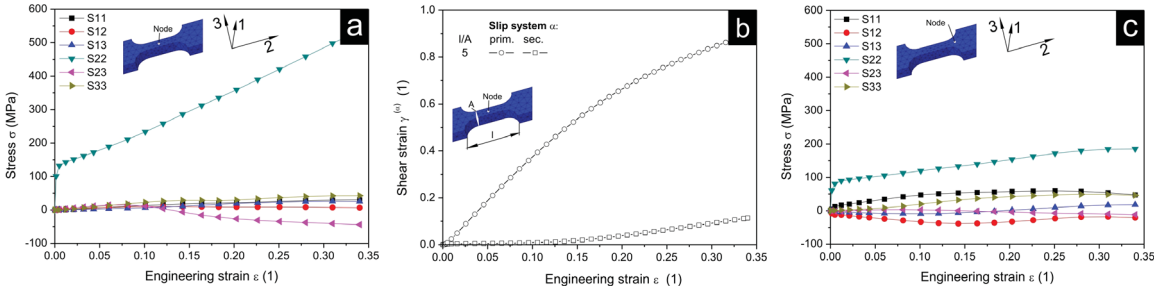

Figure C.6.: Simulated stress tensor components- (a, c) and shear strain $\gamma^{(\alpha)}$ versus engineering strain maps (b) of a Gauss point in the sample center (a, b) and at the sample shoulders (c), for the soft orientated single-crystalline sample. For clarity the Gauss points are marked on the sample surface however, the evolution took place at a Gauss point in the midsection of the specimen, i.e. inside the material.

of crystal plasticity into account and explicitly point out any deviation from the experiment. The analysis of the stress tensor in Fig. C.6 a) clarifies that the inner section of the tension test sample is under uniaxial stress state and shear is carried to 90% of the primary slip system, see Fig. C.6 (b). The fixation of the tension axis leads to rigid body rotation of the the inner sample section, of about 7 degrees from $\langle 11\ 7\ 20 \rangle$ to the stable $\langle 1\ 1\ 2 \rangle$ orientation. To compensate this lattice rotation at the sample shoulders, geometrically necessary dislocations (GNDs) are stored. In IPFs this can be seen by the strong orientation gradient in this region. On closer examination of orientation changes at the sample shoulders, different slip systems are activated, see detail back-scattered-electron-image and IPFs of Fig. C.4. This results from a reduction in cross-sectional area, which leads to an multi axial stress state as shown Fig. C.6 (c). Thus, it is reasonable that other slip systems are activated compared to the inner section of the sample.

Influence of grain boundaries

It is well known that the plastic deformation of polycrystals cause strain gradients and crystal orientation changes. Especially in the vicinity of high angle grain boundaries (HAGB), which can be characterized by the discontinuity of crystalline lattice, strain incompatibilities can be found. The incremental strain- and the misorientation path plots in Fig. C.7 confirm this fact. The strain-path plots of the bi-crystalline sample show a pronounced strain gradient in the vicinity of the HAGB. The highest strains in the soft crystal, shown on the left side in Fig. C.7, occur in the closer vicinity to the grain boundary for the first strain increment of 14%. In the second deformation step, the strain maximum is shifted to the grain interior, as a consequence of work the hardening of grain boundary region. From the analysis of the simulation data it can be concluded that the values found in the experiment match the simulated ones quite good. This indicates that the crystal plasticity model can reproduce grain – grain interactions in consideration with crystal orientation and anisotropic elastic behavior.

Influence of the initial crystal orientation on the structural evolution

The dependency of microstructural evolution on the initial grain orientation, has been investigated by many authors from an experimental as well from the simulation side of view.[41–43] As mentioned in section C.5.2, plastic straining of the soft single slip oriented grains leads to a rigid body rotation, see Fig. C.4, Fig. C.5(b) (left grain) and its pole figure. Slight fluctu-

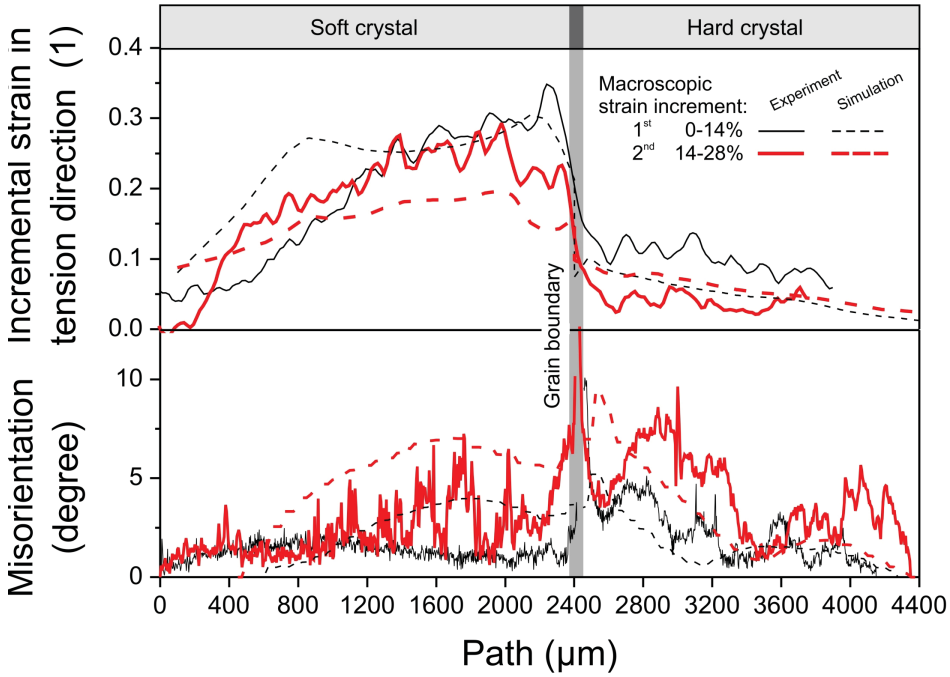

Figure C.7.: A comparison of experimentally determined to simulated incremental true strain paths and misorientation paths (dashed lines are numerical results). The position of the paths is plotted in Fig. C.5.

ations of the crystal orientation in the inner rotated section are presented due to interaction of the slip systems with the grain boundary or the sample surface roughness, originating from the manufacturing of the sample. The different density of slip lines, observable in the soft grain on the bi-crystalline sample surface in Fig. C.5b) (left grain), confirms the effect of these interactions. In the quantitative analysis shown in Fig. C.7 (left grain), this can be seen as a fluctuation of incremental strain and the intragranular crystal orientation. In contrast to the experimental observation, the simulation predict the strain and orientation evolution in a more homogenized form.

The evolution of deformation structures in a double slip, or multislip orientated crystal, a so called hard crystal, is more complex than in single slip orientated ones. In such crystals two slip system have the same Schmid factor relative to a given uniaxial stress state. As expected from Schmid's theory the crystal plasticity simulation results confirm that these two slip systems are activated simultaneously. Conversely, the experimental observations show a strong subdivision of the crystal by favoring one of the primary slip systems, see Fig. C.5b) (right grain). It will be assumed that a small initial orientation scatter or geometrical constraint of the sample can explain such a behavior.[30] An analysis of the simulation data, represented as shear-strain path plot in Fig. C.8, demonstrates that no pattern in slip system activation in the same wavelength as experimentally observed, can be found. Owing to the used rate dependent formulation of the Schmid law the slight differences in the resolved shear stress can only reduce or increase the shear strain on this slip system and cannot switch it off. A higher power law exponent n, see Equation C.3, would give a better approximation of the discontinuous Schmid behavior, but can result in a numeric instability in the FEM solving algorithms. In the next section, some slight modifications of the type I model to include the substructural crystal fragmentation process will be suggested.

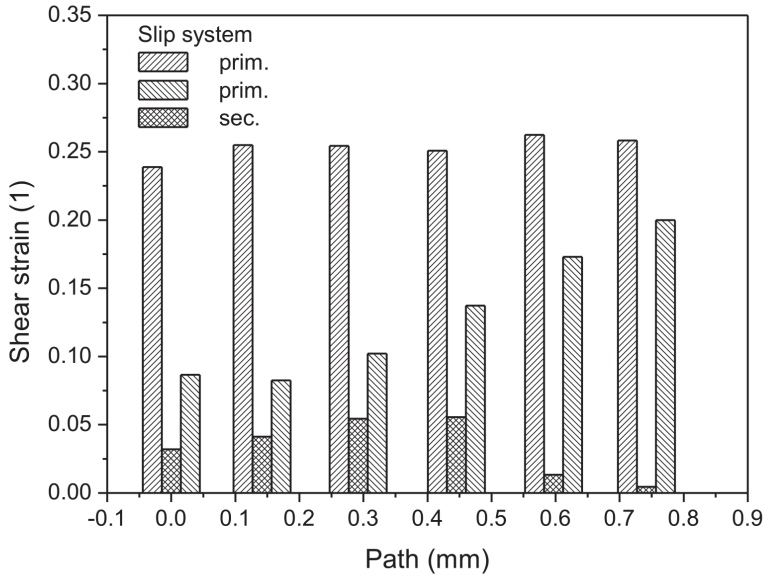

Figure C.8.: Slip activity perpendicular to the tension direction see path Fig. C.9 a).

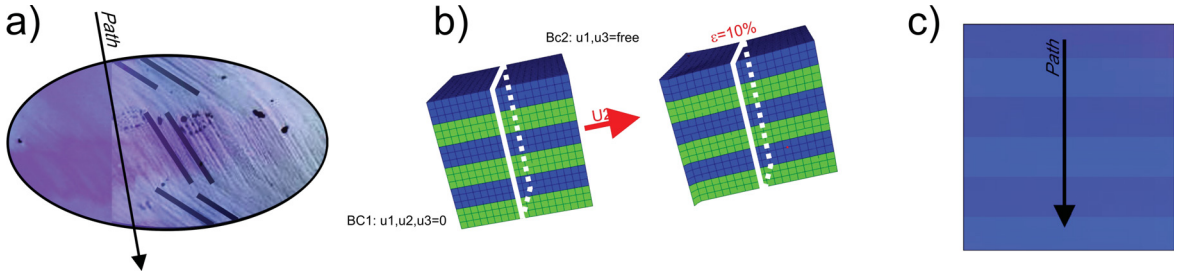

Figure C.9.: Simulation of the crystal fragmentation process of the hard orientated crystal in the bi-crystalline sample: (a) experimental IPF; (b) undeformed and ϵ =10% the deformed state of the lamellar structured cube; (c) IPF of the deformed state, highlighted as rectangle (b). The results along the paths indicated by solid lines are compared in Fig. C.10.

C.5.3. Incorporating a structural length scale in the Bassani&Wu cp-FEM model

Motivated by the work of Leffers[44,45] in which the crystalline subdivision of aluminum was modeled by a lamellar structure and the different activation of slip systems the Bassani&Wu[13,14] model is modified. The modifications in our work will be explained with the help of the previously described hard double slip orientated bi-crystalline sample. The observation of periodic fluctuations with alternate activation of one primary slip system, see Fig. C.9(a), are approximated as lamellarly structured cube. Each lamella has the same orientation, but in alternation one of the two primary slip systems is switched off. This can be realized in the user material subroutine by generating a material with 11 instead of 12 slip systems of the {111} <110> family. The results from a tension test on the lamellar cube after an ϵ=10% is shown in Fig. C.9 b) and c). From the comparison of the experimental misorientation to the simulated one, the capability to describe the fragmentation can be

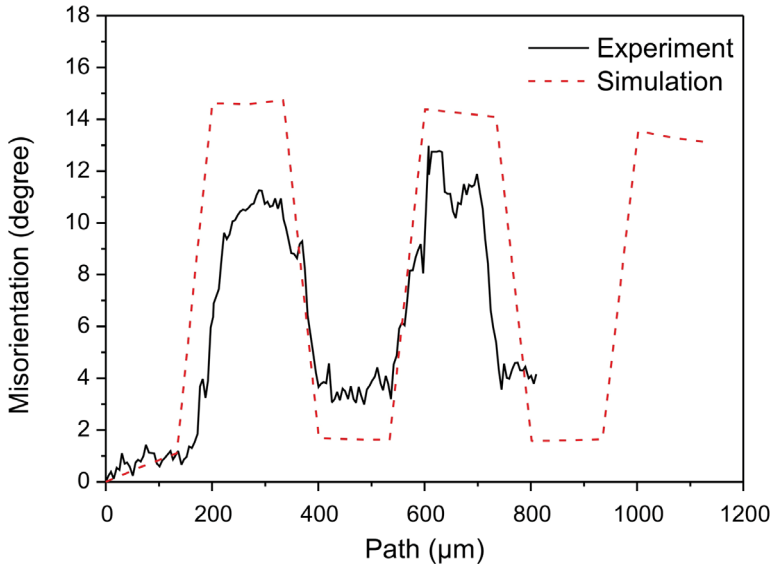

Figure C.10.: Comparison of misorientation path plots from experiment and simulation of a bi-crystalline tension test sample. The position of the path is plotted in the hard orientated grain, see Fig. C.9.

deduced, see Fig. C.10. This indicates that the implementation of a structural length scale and activation of a slip system, can be used to study the crystal fragmentation process. On the one hand, one may argue that the switching off of one slip system with a high Schmid factor is a very arbitrary assumption, on the other hand it reflects the experimental observations quite well. We tested other possibilities like the introduction of small fluctuations of the initial orientation, but these simulations were not successful in displaying the experimentally observed fragmentation. The physical conditions for the proper choice of the lamellar spacing and the selection of a slip system, which should be switched off however remains an open issue.

C.6. Conclusion

Single crystalline and bi crystalline austenitic stainless steel A220 samples were deformed under tension, with a constant crosshead speed of $10\,\mu$m/s, to engineering strains of about 30%. Crystal plasticity FEM simulations with the Bassani&Wu[13,14] model were performed and validated. The identification of the Bassani&Wu model parameter set is a sensitive process. Due to the underlying mechanisms it cannot be seen directly in the overall stress strain response. Therefore, slip system activity of differently orientated crystals must be taken into account for the determination of inelastic material parameters. The sample geometry, boundary conditions and high angle grain boundaries have an enormous influence on the crystal orientation evolution during plastic deformation. These restrictions hinder the dislocation movement and influence the storage of geometrical dislocations. The orientation changes at sample shoulders or grain boundaries can be captured from the simulation model. The fragmentation of a crystal is strongly dependent on the initial orientation and on the boundary conditions. Different activation of slip systems in a crystal is identified to control the structural evolution of a lamellar substructure. The description of such a structural evolution lies beyond the capability of the crystal plasticity FEM approach. Owing to the numerical description of a rate dependent Schmid's law, any change in the resolved shear

stress on a slip system reduces or increases the crystallographic shear. However, this change will never turn off a slip system completely. A slight modification of the model and the implementation of a structural length scale delivers the experimentally observed substructure.

Bibliography

[1] Taylor GI. The mechanism of plastic deformation of crystals. Part I. Theoretical. Proc. R. Soc. Lond. A 1934;145:362.

[2] Seeger A, Schök G. The splitting of dislocations in metals with close-packed lattices. Acta Metall. 1952;1:519.

[3] Nabarro FRN, Basinski ZS, Holt DB. The plasticity of pure single crystals. Adv. Phys. 1964;13:193.

[4] Mecking H, Kocks UF. Kinetics of flow and strain-hardening. Acta Metall. 1981;29:1865.

[5] Estrin Y, Mecking H. A unified phenomenological description of work hardening and creep based on one-parameter models. Acta Metall. 1984;32:57.

[6] Kocks UF, Mecking H. Physics and phenomenology of strain hardening: the fcc case. Prog. Mater. Sci. 2003;48;171.

[7] Taylor GI. Plastic strain in metals. J. Inst. Metals 1938;62:307

[8] Rice JR. Inelastic constitutive relations for solids: an internal-variable theory and its application to metal plasticity. J. Mech. Phys. Solids 1971;19:433.

[9] Hill R, Havner KS. Perspectives in the mechanics of elastoplastic crystals. J. Mech. Phys. Solids 1982;30:5.

[10] Asaro RJ. Micromechanics of crystals and polycrystals, in: Hutchinson JW, Wu TY (Eds.). Advances in Applied Mechanics, vol. 23. New York: Academic Press; 1983.

[11] Havner KS. Finite Plastic Deformation of Crystalline Solids (Cambridge Monographs on Mechanics), Cambridge: Cambridge University Press; 1992.

[12] Peirce D, Asaro RJ, Needleman A. An analysis of nonuniform and localized deformation in ductile single crystals. Acta Metall. 1982;30:1087.

[13] Wu TY, Bassani JL, Laird C. Latent hardening in single crystals I. Theory and experiments. Proc. R. Soc. London. A 1991;435:1.

[14] Bassani JL, Wu TY. Latent hardening in single crystals II. Analytical characterization and predictions. Proc. R. Soc. London. A 1991;435:21.

[15] Kalidindi SR, Bronkhorst CA, Anand L. Crystallographic texture evolution in bulk deformation processing of FCC metals. J. Mech. Phys. Solids 1992;40:537.

[16] Bronkhorst CA, Kalidindi SR, Anand L. Polycrystalline plasticity and the evolution of crystallographic texture in fcc metals. Phil. Trans. R. Soc. Lond. A 1992;341:443.

[17] Bassani JL. Plastic flow of crystals, in: Hutchinson JW, Wu TY (Eds.). Advances in Applied Mechanics, vol. 30. New York: Academic Press; 1994.

[18] Beaudoin AJ, Dawson PR, Mathur KK, Kocks UF, Korzekwa DA. Comput. Methods Appl. Mech. Eng. 1994;117:49.

[19] Musienko A, Tatschl A, Schmidegg K, Kolednik O, Pippan R, Cailletaud G. Three-dimensional finite element simulation of a polycrystalline copper specimen. Acta Mater. 2007;55:4121.

[20] Evers LP, Parks DM, Brekelmans WAM, Geers MGD. Crystal plasticity model with enhanced hardening by geometrically necessary dislocation accumulation. J. Mech. Phys. Solids 2002;50:2403.

[21] Cheong KS, Busso EP, Arsenlis A, A study of microstructural length scale effects on the behaviour of FCC polycrystals using strain gradient concepts. Int. J. Plasticity 2005;21:1797.

[22] Ma A, Roters F, Raabe D. Studying the effect of grain boundaries in dislocation density based crystal-plasticity finite element simulations. Int. J. Solids Struct. 2006;43:7287.

[23] Alankar A, Mastorakos IN, Field DP. A dislocation-density-based 3D crystal plasticity model for pure aluminum. Acta Mater. 2009;57:5936.

[24] Davidson DL. The observation and measurement of displacements and strain by stereo imaging. Scanning Electron Microsc. 1979;2:79.

[25] Raabe D, Sachtleber M, Zhao Z, Roters F, Zaefferer S. Micromechanical and macromechanical effects in grain scale polycrystal plasticity experimentation and simulation. Acta Mater. 2001;49:3433.

[26] Sachtleber M, Zhao Z, Raabe D. Experimental investigation of plastic grain interaction. Mater. Sci. Eng. 2002;336:81.

[27] Tatschl A, Kolednik O. A new tool for the experimental characterization of micro-plasticity. Mater. Sci. Eng. A 2003;339:265.

[28] Tatschl A, Kolednik O. Erratum to "On the experimental characterization of crystal plasticity in polycrystals" [Materials Science and Engineering A 342 (1-2) (2003) 152-168]. Mater. Sci. Eng. A 2004;364:384.

[29] OIM Analysis 5 User Manual, TexSEM-Labs. Inc; 2008.

[30] Rehrl C, Kleber S, Antretter T, Pippan R. Experimental validation of microstructure evolution in crystalline materials. J. Phys.: Conf. Ser. 2010;240:012157.

[31] ABAQUS/Standard Version 6.8-2, Providence, RI, USA: Dassault Systmes Simulia Corp.; 2008.

[32] Huang Y, A User-material subroutine incorporating single crystal plasticity in the ABAQUS finite element program, in: Mech Report 178, Division of of Engineering and Applied Sciences, Harvard University, Cambridge, MA;1991.

[33] Schmid E, Boas W. Plasticity of Crystals with Special Reference to Metals. London: Hughes & Co Limited; 1950.

[34] Hutchinson JW. Bounds and self-consistent estimates for creep of polycrystalline materials. Proc. R. Soc. Lond. A 1976;348:101.

[35] J.W. Kysar, Addendum to A User- Material Subroutine Incorporating Single Crystal Plasticity In the ABAQUS Finite Element Program, in: Mech Report 178, Division of Engineering and Applied Sciences, Harvard University, Cambridge, MA, 1997.

[36] Mangalick ME, Fiore NF. Trans. Metall. Soc. AIME 1968;242:2363.

[37] Malin AS, Hatherly M. Microstructure of cold-rolled copper. Metal Sci. 1979;13:463.

[38] Hughes DA, Nix WD. Large plastic deformation of some fcc metals at low and intermediate temperature. Met. Trans. A 1988;19:3013.

[39] Hansen H, Juul Jensen D, Hughes DA. Textural and microstructural evolution during cold-rolling of pure nickel. Mater. Sci. Forum 1994;157-162:693.

[40] Hansen H, Hughes DA. Analysis of large dislocation populations in deformed metals. Phys. Stat. Sol. b 1995;149:155.

[41] Raabe D. Simulation and experimental examination of the evolution of orientation gradients in single grains during rolling of body centered cubic polycrystals. Phys. Stat. Sol. B 1994;181:291.

[42] Raabe D, Zhao Z, Roters F. Study on the orientational stability of cube-oriented fcc crystals under plane strain by use of a texture component crystal plasticity finite element method. Scr. Mater. 2004;50:1085.

[43] Raabe D, Ma D, Roters F. Effects of initial orientation, sample geometry and friction on anisotropy and crystallographic orientation changes in single crystal microcompression deformation: A crystal plasticity finite element study. Acta Mater. 2007;55:4567.

[44] Leffers T. A model for rolling deformation with grain subdivision. Part I: The initial stage. Int. J. Plast. 2001;17:469.

[45] Leffers T. A model for rolling deformation with grain subdivision. Part I: The subsequent stage. Int. J. Plast. 2001;17:491.

D

Effect of forming conditions on the softening behavior in coarse grained structures

C. Rehrl[a], S. Kleber[b], O. Renk[a], R. Pippan[a]

[a] Erich Schmid Institute of Materials Science, Austrian Academy of Sciences, A–8700 Leoben, Austria
[b] Böhler Edelstahl GmbH, A–8605, Austria

Abstract

Polycrystalline nickel with a purity of 99.99 wt% and different starting grain sizes of 240 μm and 770 μm has been investigated. The effects of the initial grain size on the hot deformation behavior were studied by compression tests at various forming conditions. The microstructure was captured after deformation, using electron back scatter diffraction technique (EBSD). A variation of the initial grain size has unexpected effects on the acting softening mechanisms. A coarsening in the starting microstructure leads to a higher flow stress and a remarkable higher hardening at elevated temperatures. Furthermore, the nucleation of dynamic recrystallized grains is enormously retarded due to the less pronounced grain boundary bulging in a coarser grained microstructure compared to a finer one. As a consequence, discontinuous dynamic recrystallization generates a metastable grain size, that is finer than the steady state grain size.

D.1. Introduction

The refinement processes during warm forming of coarse grained structured metallic materials are of technical interest to improve the mechanical properties and to generate a well defined microstructure. Dynamic recrystallization during and after warm forming is the unique process that can be used to refine the microstructure of metals without phase transformations (Ni, Cu, Al, γ-iron). Dynamic as well as static recovery and recrystallization are the dominant processes controlling the final microstructure.
The main characteristics of dynamic recrystallization and recovery under different forming conditions have been analyzed by numerous authors, see for example.[1–10] In low to medium stacking fault energy materials, such as austenitic stainless steels, copper and nickel, discontinuous dynamic recrystallization (DDRX) is the main recrystallization mechanism. The microstructural evolution is characterized by the formation of new equiaxed grains at preexisting grain boundaries[11–15] or deformation heterogeneities which have a high local misorientation.[16–18] Furthermore, it has been shown that the forming conditions, temperature and strain rate have a pronounced effect on the transition from single to multiple peak behavior in the stress-strain response. In addition to the forming parameters, this transition in flow behavior is strongly influenced by the initial grain size and has been extensively investigated by Sakui et al., Sakai and Jonas.[19,20] These experimental observations clearly show that the shape of the flow curve is determined by the nucleation density of grains. Sakai et al. proposed in their model that grain boundary sliding and annealing twinning are the basic steps required for DRX nucleation.[21,22] Miura et al. pointed out the particular importance to previous grain-boundary serration and grain-boundary migration mechanisms, which can be accompanied with the twinning process.[12,23] In marked contrast to the clear relation between grain boundary mobility and nucleation of new grains, which has already been investigated by many authors, there are only a few publications on the influence of grain boundary mobility and grain size on the stress-strain response. In the work of Angella et al., performed on an austenitic stainless steel 316L, strong strain induced boundary migration (SIBM) events helped to trigger the nucleation process.[24] Additionally, they reported from an anomalous flow behavior, caused by SIBM, where a coarser grained material had a higher hardening response as a finer grained one.
The present work examines the influence of initial grain size on the flow behavior and microstructural evolution of coarse grained nickel. Compression tests at various forming conditions analyzed with the orientation imaging microscopy technique, serve as the basis for the understanding of the underlaying mechanism. In order to better understand the phenomena controlling the dependence of the structural evolution and flow stress during hot forming on the initial grain size a detailed analysis, using the EBSD technique is performed.

D.2. Experimental procedure

Pure nickel (99.99 wt%) polycrystalline samples were deformed by compression tests at different warm forming temperatures to investigate the influence of initial grain size on the structural refinement process. The compression test samples, with a diameter of 10 mm and a height of 12 mm, were machined from plates. The specimens were deformed in an displacement controlled mode with constant cross-head speeds of 5 mm/min or 50 mm/min, equivalent to an average strain rates of $\dot{\epsilon} \approx 0.01\,s^{-1}$ and $\dot{\epsilon} \approx 0.1\,s^{-1}$. A compression test unit "Schenck-Trebel" was used. Temperature was held constant at ambient temperature, 450°C, 830°C, 1000°C or 1180°C during the compression. To minimize static- and post-dynamic softening processes, the samples were water quenched after the deformation step

within one second. Two sets of specimens having different initial grain sizes of D_0=240 μm and D_0=770 μm were used. The different microstructural features of the finer grained and the coarser grained sample are shown in Fig. D.1. Both structures consist of equiaxed grains. One distinctive feature of the coarser grained material is the occurrence of few annealing twins.

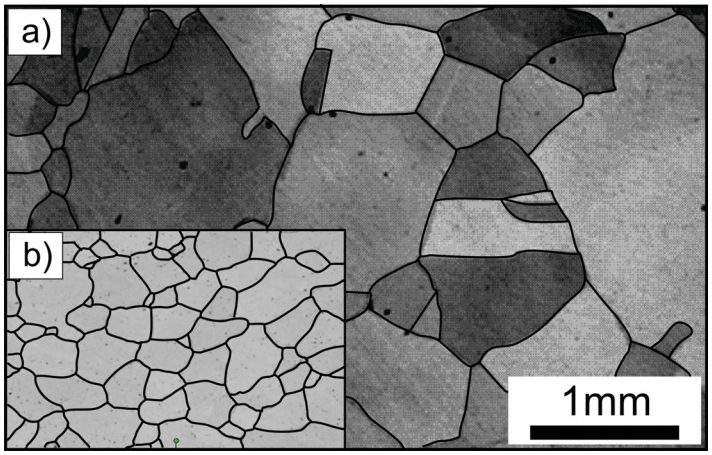

Figure D.1.: Initial microstructure of nickel 45% cold worked and annealed at 1180°C (a) for 48h with D_0=770 μm and (b) for 1h with D_0=240 μm.

$$\Delta g_k = \frac{1}{12} \sum_{i=1}^{12} \Delta g_i \tag{D.1}$$

The structural analysis of undeformed and deformed material is based on the measurements of the local crystal orientation. These measurements were carried out with an EBSD-SEM system (a TSL EBSD system interfaced to a LEO 1525). To get rid of any preparation artifacts the sample surfaces were polished mechanically as well as electro-chemically. The grain boundary profile and differences in crystallographic orientation of the samples after the forming process are plotted as Inverse Pole Figure (IPF) maps and Kernel Average Misorientation (KAM) maps. Fig. D.2 represents the kernel used for misorientation calculation. In

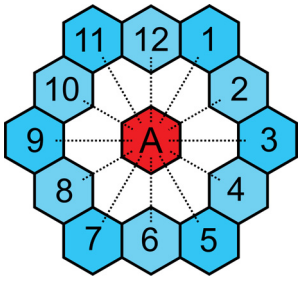

Figure D.2.: Kernel based misorientation calculation

this mode, the misorientation between the center point and all points at the perimeter of the kernel are measured. The local misorientation value Δg_k assigned to the center point is the average of these misorientations Δg_i as given in equation D.1.[25] The procedure is similar as in the analyses proposed by Vorhauer et al.[26]. The second neighbors at the perimeter were taken to weaken the influence of single erroneous data points on the results.

D.3. Results

D.3.1. Stress-strain behavior

In Fig. D.3 a), the stress-strain curves and in Fig. D.3 b) the corresponding hardening curves of different initial microstructures are plotted. The samples were deformed at different temperatures with a constant crosshead speed equivalent to a strain rate of about $\dot{\epsilon} \approx 0.1\,s^{-1}$. Stress-strain curves for the finer grained samples are represented by dashed lines and those for the coarser grained specimens are visualized by solid lines. For deformation experiments at ambient temperature and 450°C a plateau stress could not be reached due to the limitation in forming capacity. Several differences in the shape of the curves, when comparing the influence of initial grain size were, found. The deformation experiments at ambient temperature show a "typical" cold working behavior. In the forming temperature range from 450°C to 1000°C the coarser grained material has a higher flow-stress and a higher hardening than the finer grained material for strains larger than few percents. At a deformation temperature of 1180°C this effect is retarded and does not become visible before the peak strain in the finer grained material was reached. Forming at elevated temperatures results in a typical warm forming flow curve showing a peak stress, a slight stress drop and a steady state region. As a general trend, a coarser initial grain size reduces the stress drop and shifts the peak stress and strain to higher values. Contrary, the stress-strain behavior at ambient temperature experiments is characterized by strain hardening and dynamic recovery.

The strain hardening versus stress curves in Fig. D.3 b) illustrate the change in hardening

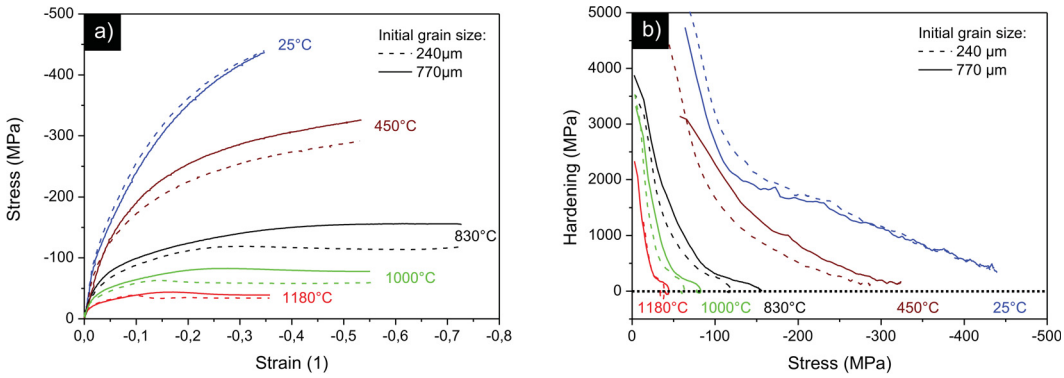

Figure D.3.: Stress-strain curves (a) and hardening-stress curves (b) of nickel with different initial grain sizes deformed at constant crosshead speed of 50 mm/min ($\dot{\epsilon} \approx 0.1\,s^{-1}$) at different temperatures.

behavior in more detail. At the beginning of deformation equivalent to small yield stresses, a higher hardening for the finer grained material was observed. Further straining changes the hardening behavior in the opposite direction, i.e. the finer grained material shows the stronger hardening for the 25°C temperature. With increasing forming temperature this change is shifted to a smaller plastic strain or flow stress.

Fig. D.4 shows the influence of the strain rate on the stress-strain behavior at higher forming temperatures. Generally, for a lower strain rate a reduced flow-stress and a shift of the peak strain and -stress to smaller values was observed. Differences in peak stresses and strains resulting from the initial grain size diminish with a slower strain rate and a higher forming temperature. A variation of deformation parameters to a lower Zener-Holloman parameter Z [temperature corrected strain rate ($Z = \dot{\epsilon} \cdot exp(Q/RT)$, where Q is the activation energy for warm forming and R the universal gas constant)] as well as a finer initial grain size changed the whole stress-strain kinetic from a single- to a multi peak flow behavior.

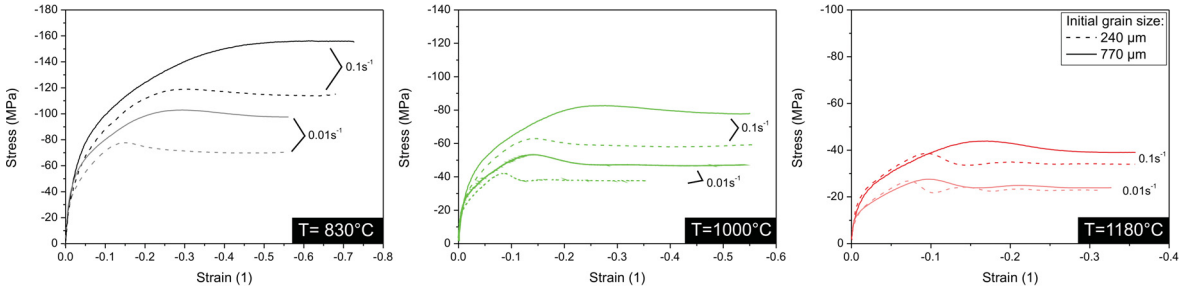

Figure D.4.: Stress-strain curves of nickel with different initial grain sizes deformed at constant temperature of 830°C, 1000°C or 1180°C and different crosshead speeds of 5mm/min ($\dot{\epsilon} \approx 0.01\,s^{-1}$) and 50 mm/min ($\dot{\epsilon} \approx 0.1\,s^{-1}$).

The hardening versus stress curves of Fig. D.5 clearly show that the stage III of hardening

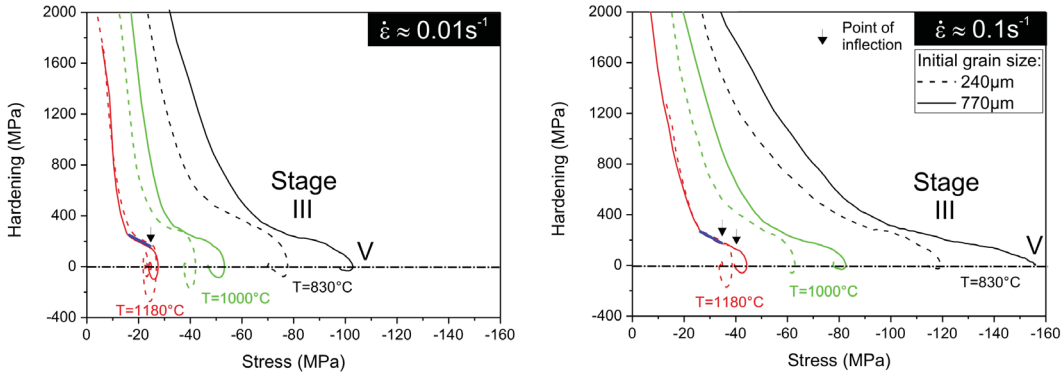

Figure D.5.: Hardening-stress plots of nickel with different initial grain sizes deformed at constant temperature of 830°C, 1000°C or 1180°C and different crosshead speeds of 5mm/min ($\dot{\epsilon} \approx 0.01\,s^{-1}$) and 50 mm/min ($\dot{\epsilon} \approx 0.1\,s^{-1}$).

and the point of inflection (Stage III-V) is strongly influenced by the strain rate. At the point of inflection critical conditions (critical stress σ_c and strain ϵ_c) for a microstructural instability are reached. Extensive subboundary motion and bulging as well as annealing twinning promotes DRX.[27] At the highest forming temperature of 1180°C and the lowest strain rate a congruent hardening stage III was found, indicated by blue bold lines in Fig. D.5. This is independent of grain size. The point of inflection from stage III-V occurred nearly at the same flow stress. A higher strain rate of $\dot{\epsilon} \approx 0.1\,s^{-1}$ shifted this point of inflection in the coarser grained material to a higher flow stress.

D.3.2. Microstructural evolution

Influence of forming parameters on the microstructural evolution

The influence of forming temperature on the microstructural evolution of nickel with initial grain sizes of 770 μm and 240 μm and deformed to a flow stress plateau is shown in Figs. D.6 and D.7. Different strain rates of $\dot{\epsilon} \approx 0.01\,s^{-1}$ and $\dot{\epsilon} \approx 0.1\,s^{-1}$ are taken into account. The compression test samples shows the typical barreling and the characteristic forging cross. For that reason the discussion refers to the uniformly strained sample center from Figs. D.6 and D.7. Additionally, proper KAM-maps, taken as detail scans from the center of the sample, are also plotted in the figures. In the IPFs, black solid lines illustrate high angle grain boundaries with a misorientation greater than 15°. A typical feature of

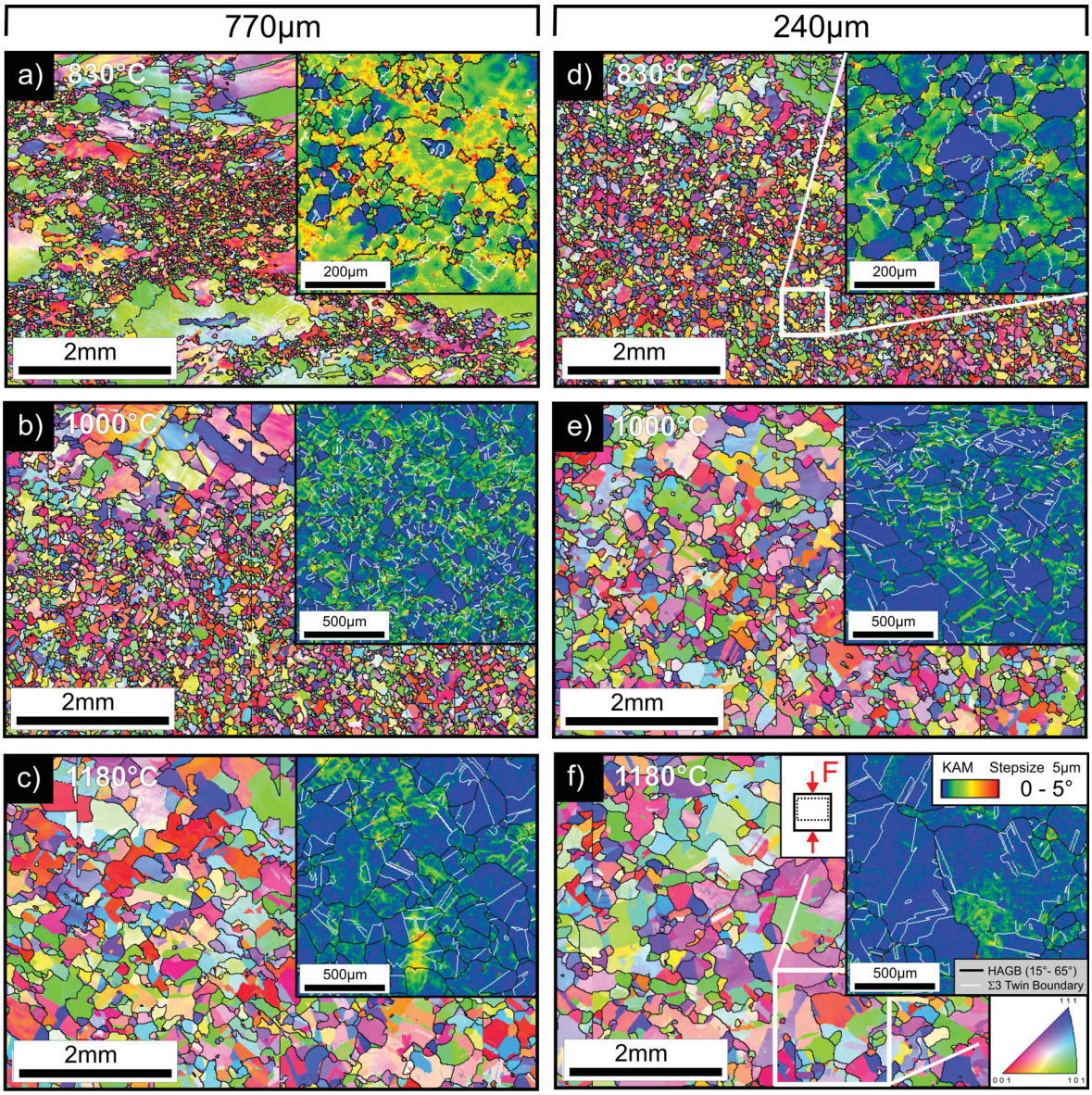

Figure D.6.: Microstructural evolution of samples, shown as IPF(compression direction) overlayed with KAM-maps, deformed with an $\dot{\epsilon} \approx 0.01\,s^{-1}$ at 830°C: (a) ϵ=0.57 (770 μm) and (d) ϵ=0.57 (240 μm), at 1000°C: (b) ϵ=0.57 (770 μm) and (e) ϵ=0.38 (240 μm) and at 1180°C: (c) ϵ=0.38 and (f) ϵ=0.38 (240 μm). High angle grain boundaries and twin boundaries are marked as black and white lines.

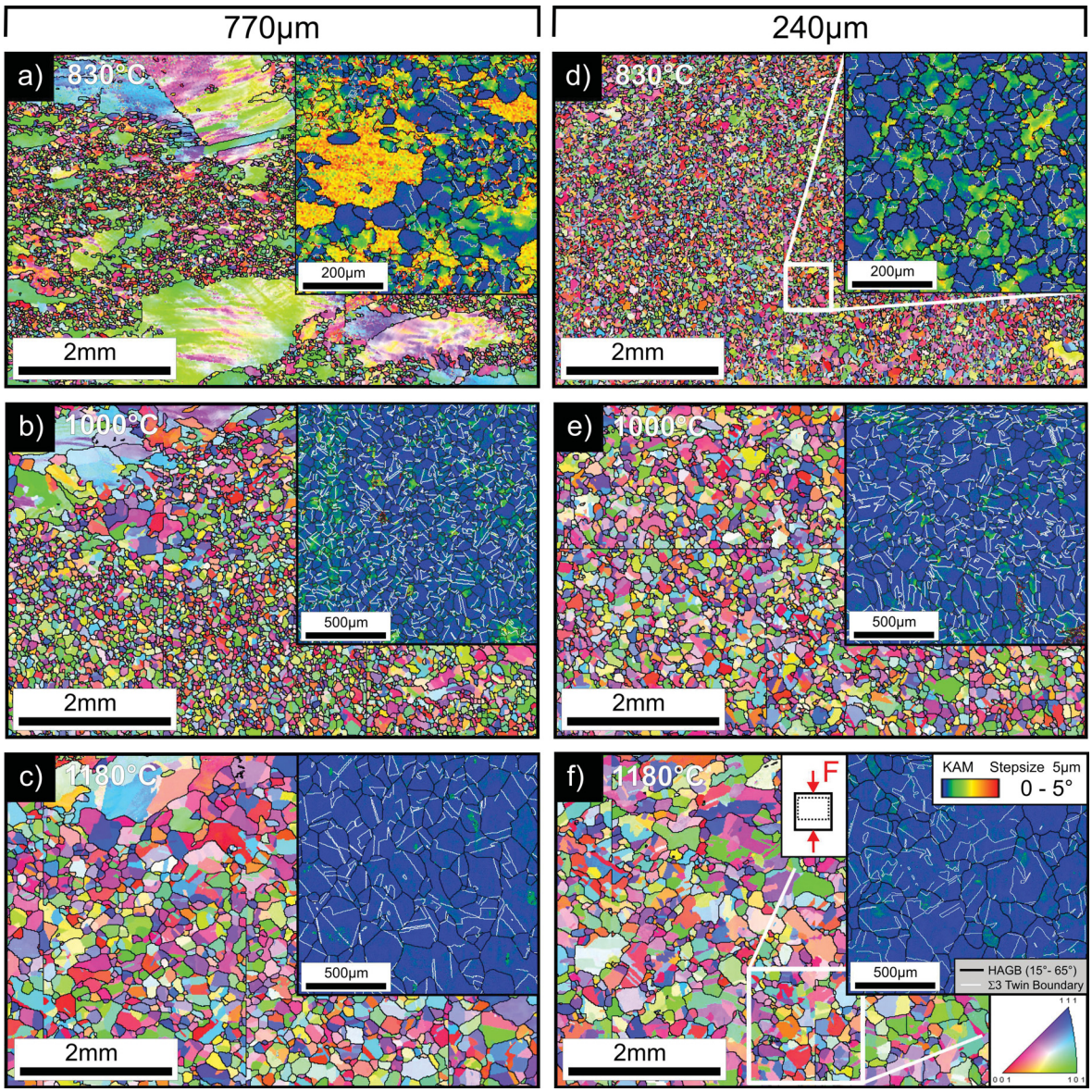

Figure D.7.: Microstructural evolution of samples, shown as IPF(compression direction) overlayed with KAM-maps, deformed with an $\dot{\epsilon} \approx 0.1\,s^{-1}$ at 830°C: (a) ϵ=0.74 (770 μm) and (d) ϵ=0.74 (240 μm), at 1000°C: (b) ϵ=0.57 (770 μm) and (e) ϵ=0.57 (240 μm) and at 1180°C: (c) ϵ=0.38 (770 μm) and (f) ϵ=0.38 (240 μm). High angle grain boundaries and twin boundaries are marked as black and white lines.

recrystallized grains are annealing Σ3 twins, marked in KAM maps as solid white lines. By using the KAM, a qualitative criterion to distinguish recrystallized and non-recrystallized matrix was found.
Figs. D.6 a) and D.7 a) present a partly recrystallized inhomogeneous microstructure, of the 770 μm grained material deformed at 830°C to a strain of 57 % and 74 %. Discontinuous dynamic recrystallization (DDRX) starts at the old grain boundaries, shown in Fig. D.9 b. Furthermore, grain boundaries of newly formed grains act as nucleation sites and so a typical necklace structure is formed. The non recrystallized areas store a high amount of energy. In particular cases, intragranular nucleation occurs at microstructural heterogeneities like deformation bands, which are visualized in KAM maps. The size of intragranularly nucleated grains is much larger compared to the grains formed in the necklace. For the initially finer grained materials (240 μm) (Figs. D.6 d) and D.7 d) deformed to the strain level of 57 % and 74 %, a nearly fully recrystallized homogeneous grained microstructure was observed.
The increase of deformation temperature from 830°C to 1000°C and 1180°C, presented in Fig. D.6(b-c,e-f) and Fig. D.7(b-c,e-f), leads for all the different initial grained materials to a fully recrystallized microstructure after straining to the stress plateau.
The grain size distribution of the warm formed samples, shown in fig. D.8, as well as the average recrystallized grain size, in Table D.1 are taken from the center of the sample. The material with an average initial grain size of 770 μm was refined at all forming temperature whereas the material with the finer starting structure was refined at lower temperatures and coarsened for the higher temperatures. In other words the microstructure refines at higher Z values and coarsen at lower Z values. For a decrease in the strain rate from $\dot{\epsilon} \approx 0.1\,s^{-1}$ to $\dot{\epsilon} \approx 0.01\,s^{-1}$ the microstructure is clearly characterized by a well defined substructure.

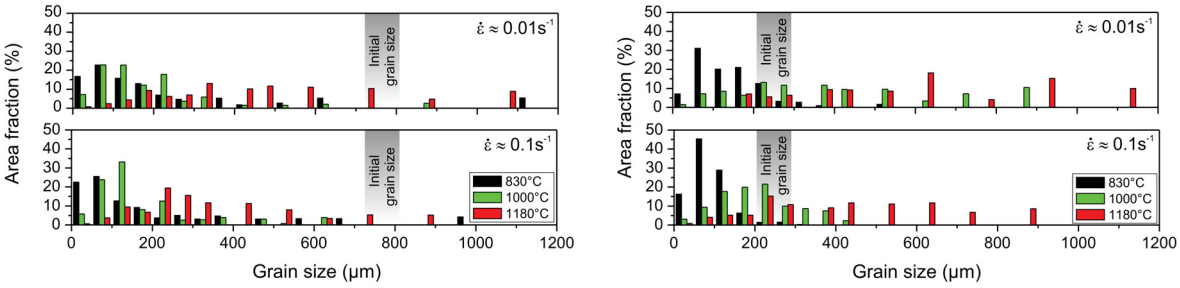

Figure D.8.: Grain size distribution of nickel warm formed at 830°C, 1000°C, 1180°C at strain rates of $\dot{\epsilon} \approx 0.1\,s^{-1}$ and $\dot{\epsilon} \approx 0.01\,s^{-1}$.

Temperature	830°C		1000°C		1180°C	
Initial grain size:	240 μm	770 μm	240 μm	770 μm	240 μm	770 μm
$\dot{\epsilon} \approx 0.01\,s^{-1}$	161 μm	62 μm	289 μm	134 μm	485 μm	417 μm
$\dot{\epsilon} \approx 0.1\,s^{-1}$	76 μm	56 μm	187 μm	106 μm	399 μm	261 μm

Table D.1.: Mean recrystallized grain size taken at the center of the compression sample.

Influence of initial grain size on the microstructural evolution

At lower strains, far away from the critical strain ϵ_c, the microstructural evolution is strongly affected by the initial grain size. Compression test samples were deformed up to ϵ=12% with a strain rate of $\dot{\epsilon} \approx 0.1\,s^{-1}$ at 830°C to investigate the nucleation process.

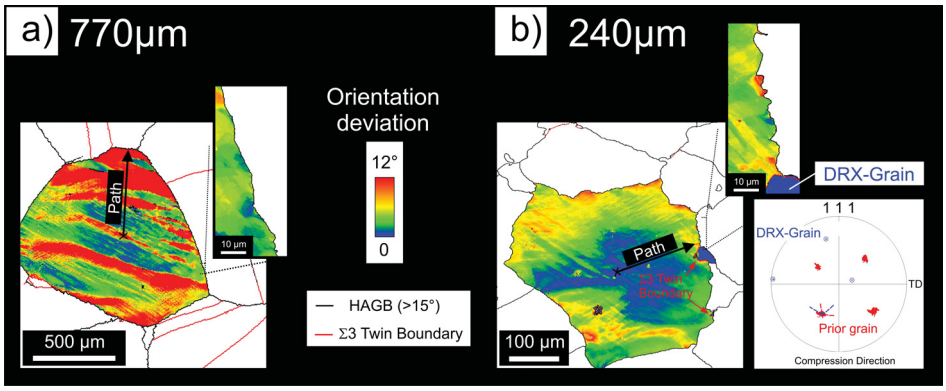

Figure D.9.: Orientation deviation maps of different initial grain sizes taken from the material (a) 770 μm and (b) 240 μm deformed with a strain rate of $\approx 0.1\,s^{-1}$ at 830 °C to an ϵ of 12%. Pole figure of the Σ3 twin orientation relation between parental and DRX grain.

The EBSD-maps in Fig. D.9 represent two selected grains, taken from the material with initial grain sizes of 770 μm (a) and 240 μm (b). The maps were highlighted with the grain orientation tolerance mode to illustrate the developed substructure. Fig. (a) shows, deformation bands along the whole grain which are a distinctive feature of the coarser grained materials. In misorientation path plots, shown in Fig. D.10, intragranular orientation

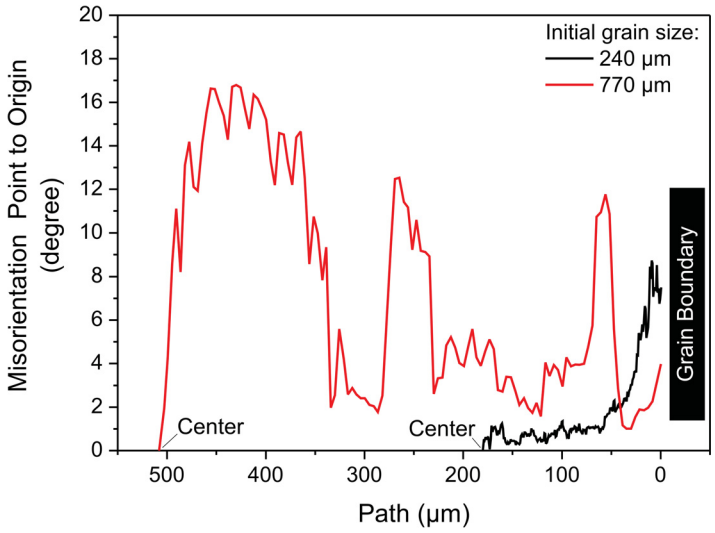

Figure D.10.: Comparison of misorientation paths of different initial grain sizes deformed with a strain rate of $\approx 0.1\,s^{-1}$ at 830 °C to an ϵ of 12%. The position of the paths is plotted in Fig. D.9.

differences of about 14° occur frequently. It is worth to mention here that the developed intragranular spacing (distance between deformation heterogeneities) has nearly the same size as the initial smaller grained material. For the finer initial grain size, pronounced orientation gradients occurred at the initial grain boundaries, whereas intragranular deformation bands were rare. Additionally, the grain boundaries in the smaller grained material were strongly serrated. Serrations as well as bulging out of the grain boundary, which takes place on a subgrain length scale, are more pronounced with a decrease in the starting grain size. The nucleation of grains took place at initial grain boundaries. In most of the cases, these new crystals are Σ3 twin orientated to the parent grain.

D.4. Discussion

The presented results illustrate the significant influence of the initial grain size on the mechanical properties during hot deformation and the microstructural evolution. The discussion is organized according to the softening mechanisms which act at different strain states:

- anomalous grain size effects on the stress-strain response;
- onset of dynamic recrystallization;
- microstructural evolution during the DRX process.

D.4.1. Anomalous grain size effects on the stress-strain response

The analysis of the flow curves, represented in Fig. D.3, illustrates an unusual change in flow behavior. At the beginning of deformation a typically higher flow stress for the finer grained material was observed. Further straining changed the flow stress behavior in the opposite direction. This change occurred at a strain of approximately 3% for the deformation experiments at 450°C. With increasing forming temperature this change was shifted to a smaller plastic strain, or flow stress, and diminishes at the highest forming temperature of 1180°C. Furthermore, the differences in flow stress are also persistent at plastic deformation larger than the critical strain, ϵ_c, where DRX is already evident in the microstructure. It is interesting to note that for $\epsilon < \epsilon_c$ DRX acts to a minimal extent and therefore an additional grain size dependent softening mechanism must cause the decrease in work hardening. This hypothesis is supported by the results of static recovery double hit deformation experiments at 450°C, which are represented in Fig. D.11. In the first hit compression test samples were prestrained to $\epsilon = 15\%$, smaller than ϵ_c, halted for 10 s and subsequently deformed to 50% strain. The initial finer grained material undergoes a 1.6 times higher stress drop at the same strain, despite the lower flow stress. This is equivalent to a higher recovery rate. Accordingly, strain induced boundary migration (SIBM) seems to be the mechanism which fulfills this experimental observation.

The model for describing the unusual hardening behavior of an austenitic stainless steel A316L, proposed by Angella et al.,[24] is used in this work for nickel. The hardening Θ can by described by

$$\Theta = \Theta_0 - (\Theta(T, \dot{\epsilon}) + \Theta_{SIBM}) \tag{D.2}$$

where Θ_0 is the athermal hardening level,[28] $\Theta(T, \dot{\epsilon})$ is a dynamic recovery term and Θ_{SIBM} the additional softening term. The externally applied stress during deformation and the differences in strain energy in the vicinity of the grain boundary, common for polycrystals, act as driving forces for SIBM.[8,29] The movement of boundaries directly minimizes the dislocation accumulation in the vicinity of grain boundaries and leaves behind areas of lower dislocation densities.[24] The influence of the grain boundary region on flow stress can be seen in the composite flow stress model as in[30,31] given by

$$\sigma = A_i\sigma_i + A_b\sigma_b \tag{D.3}$$

where σ_i, σ_b, A_i and A_b are the corresponding stresses and fractions of the grain interior region (i) and grain boundary region (b). From the microstructural point of view, a coarsening of the initial grain size leads to a reduction of grain boundary density and additionally, shown in Fig. D.9, to slight differences in grain boundary motion. The displacement of grain boundary migration in the depicted case is about 10-15 μm in both the coarse and the fine grained material. It might be somewhat smaller in the coarser than in the finer, however it is not

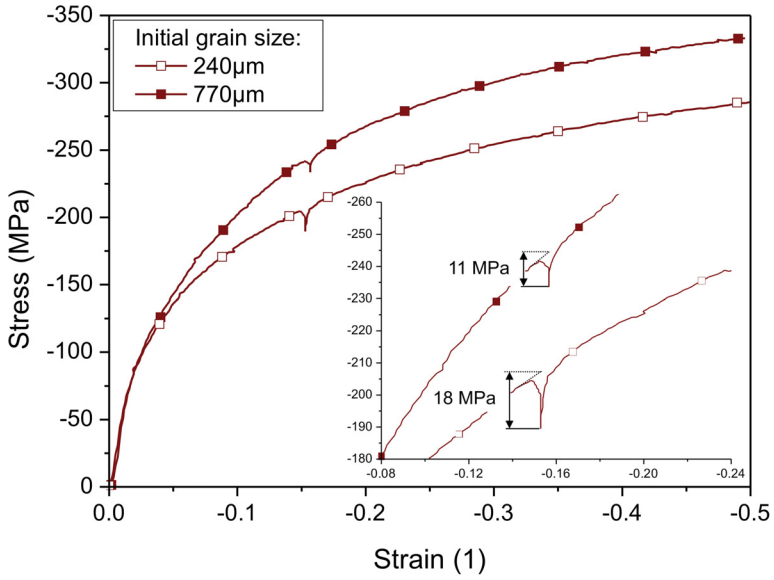

Figure D.11.: Stress-strain behavior of a double hit deformation experiments at 450°C. Prestrained to an $\epsilon = 15\%$, halted for 10 s and subsequent strained to $\epsilon = 50\%$.

easy to quantify. A simple estimation of the affected volume is based on the assumption of cubic grains, where the grain boundaries move 15 μm due to SIBM. The affected volume is given by the half of the grain boundary area times the moved distance and therefore, it is about 5.8% of the volume in the 770 μm grained material and about 18.8% in the 240 μm grained material. The movement of the grain boundary reduces the harder grain boundary area A_b. Consequently, it seems to be obvious that SIBM leads to a softer material response in the finer grained starting structure.
Depending on the forming condition, the hardening stages III and V are affected by SIBM. A decrease of the forming temperature minimizes the grain boundary mobility due to a lower thermal activation. In this case, SIBM acts in a minimal extent and typical hardening behavior was observed. At 1180°C forming temperature the flow stress behavior is mainly dominated by dynamic recovery and SIBM again plays a minor role. Only the point of inflection (σ_c, ϵ_c) from stage III to V, well known as the point where extensive DRX starts, is very sensitive on SIBM events, as described in the next section.

D.4.2. Onset of dynamic recrystallization

Several authors have reported about the important role of grain boundaries as the most preferential nucleation site for DRX, see for examples.[11,13,15,23] In these studies, the formation of new crystals was frequently initiated by grain boundary sliding and annealing twinning mechanism. Miura et al.[12] attached particular importance to grain-boundary serration and grain-boundary migration mechanisms, which can be accompanied by the twinning process. The experimental results of the present study confirmed that DRX is primarily initiated by grain-boundary bulging and subsequent annealing twinning at grain boundaries and triple junctions see Fig. D.9 b. It is clear that the density of the initial grain boundaries must affect the DRX kinetics enormously, as shown in stress-strain curves in Fig. D.4 and hardening versus stress plots of Fig. D.5. The clear lengthening of stage III, accompanied by the shift of the critical stresses, σ_c, and strains, ϵ_c, to higher values, allows one to conclude that in the coarser grained structures a higher energy density is necessary to nucleate new grains. The differences in grain boundary motion discussed in the previous section D.4.1 have an effect on

the hardening behavior but for the nucleation process the grain boundary morphology must be seen on a scale of the size of a nucleus of a new grain. In the following, the morphology will be described by a wavy boundary. Detail scans of the grain boundary after deformation of 12%, represented in Fig. D.9, show that the amplitude is nearly unaffected from the initial grain size, while the wavelength decreases for a finer starting structure of 240 μm. The coarser grained microstructure must deform to higher strain levels to reach the same grain boundary serration and bulging necessary for the nucleation process, thus influencing DRX behavior. The grain size dependent difference in grain boundary motion seems to result from the restriction to fulfill forming compatibility during the deformation process. The coarser grained material balanced the forming compatibility by an intragranular structural fragmentation, as represented in Fig. D.9(a). Contrary in Fig. D.9(b), the initial finer microstructure forming compatibility is achieved by the storage of geometrically necessary dislocation (GNDs), which were partly reduced by the strain induced movement of the grain boundary and developed waviness of the boundary.

Referring to DRX in the coarser grained microstructure, nucleation also starts at initial

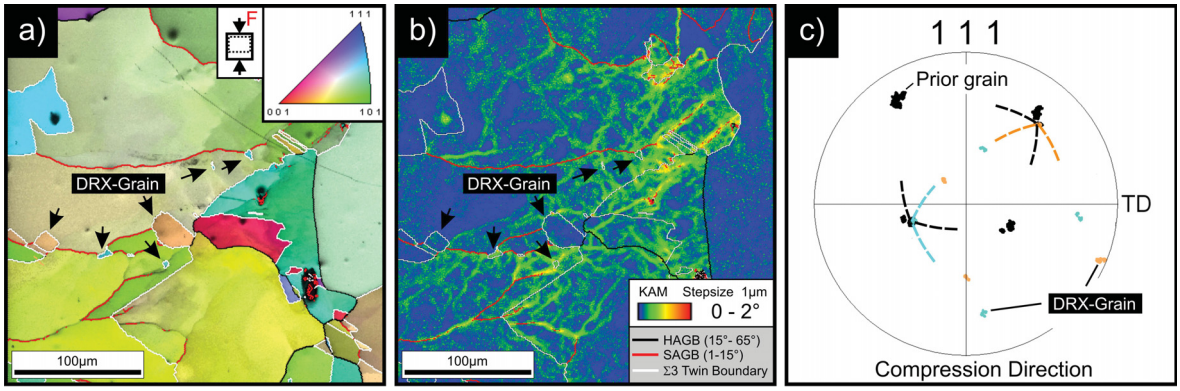

Figure D.12.: Nucleation in 770 μm grained material, deformed at 1000°C with a strain rate of $\dot{\epsilon} \approx 0.1\,s^{-1}$ to an ϵ of 18%. (a) IPF in compression direction and (b) KAM map; high angle (black lines), small angle (red lines) and twin boundaries (white lines) are highlighted in these maps. (c) Pole figure of the Σ3 twin orientation relation between parental and DRX grain. The color of nucleated grains corresponds to the orientations in the IPF.

grain boundaries. However, if the grain boundary is saturated nucleation will also take place inside the initial grains.[16] There, microstructural inhomogeneities such as deformation bands for high Z values or subgrain boundaries, formed during compression, for lower Z values, act as nucleation sites, shown in Fig. D.12 as IPF and KAM maps. The {111}-polfigures in Figs. D.9 and D.12 show that the first nucleated grains are mostly twin orientated to their parent grains.

D.4.3. Microstructural evolution during the DRX process

Sah et al.[16] reported that in nickel the steady state grain size occurs after few percent recrystallization due to the rapid growth of new grains to their final size. The characteristic of a full DRX microstructure is the occurrence of three dynamic structures: The nucleus (A, fine grains), the growing grain (B, medium grains) and the critical work hardened grain (C, large grains). At the steady state, these grain fractions are uniformly distributed over the whole matrix.[20,32,33] According to Sakui et al. and Sakai and Jonas[19,20] a qualitative microstructural mechanism map for DRX of nickel, based on Table D.1, is plotted in

Fig. D.13. This map schematically illustrates that the steady state grain size D_s, plotted as black bold line, only depends on the forming parameters, whereas the subsiding DRX mechanism is additionally affected by the initial grain size D_0. On the left side of D_s the starting microstructure will be coarsened by a multiple peak flow behavior and on the right side refined by a single peak behavior. The performed experiments and the investigated

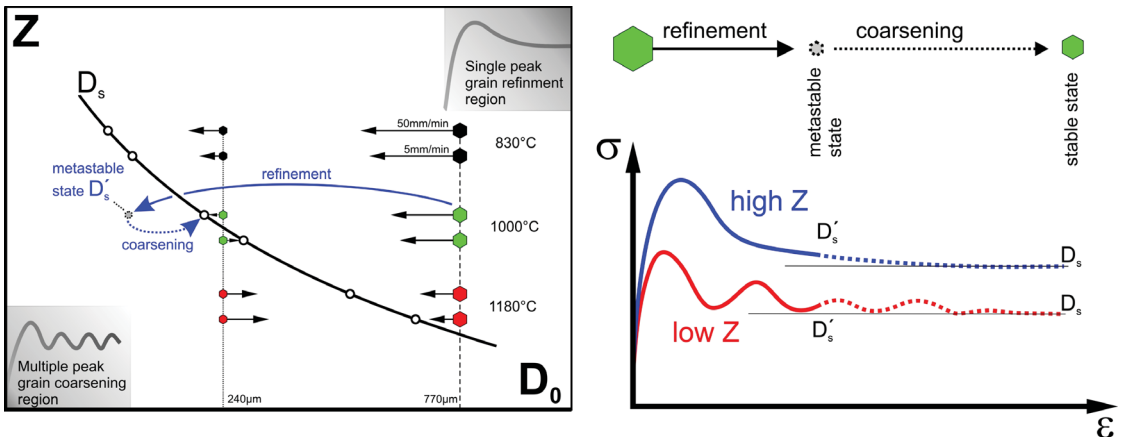

Figure D.13.: Left image: Double-logarithmic Z-D_0 plot illustrating the schematic microstructural mechanism map for distinguishing single and multiple peak two dynamic recrystallization behavior; Right image: Schematic flow behavior and the microstructural evolution for different Z parameters of the 770 μm grain sized material. The dashed lines illustrate the estimated transition from metastable to stable microstructural state.

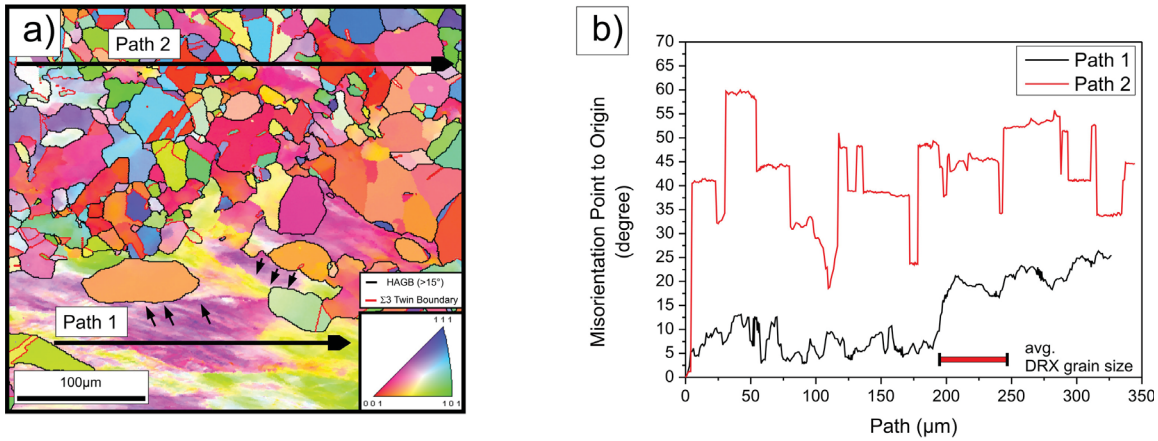

Figure D.14.: IPF in compression direction (a) with misorientation path plots (b) from a deformed (path 1) and a recrystallized section (path 2) from a 770 μm grain sized material deformed with a strain rate of $\dot{\epsilon} \approx 0.1\,s^{-1}$ at 830°C to an ϵ of 74%. Black arrows indicate the restriction in grain boundary movement due to deformation heterogeneities.

microstructures are indicated in this schematic diagram. At the lowest Z value (T=1180°C and $\dot{\epsilon} \approx 0.01\,s^{-1}$), the coarser grained structure was refined by a slight multi peak flow behavior. This higher synchronization of the DRX process clearly shows that nucleation is a time consuming process and the density of new grains is certainly a function of temperature and strain rate. In contrast to the observation of Sah et al.[16], the initially 770 μm grained material was refined to a metastable DRX grain size D'_s smaller than the steady state grain

size. While, for the 240 μm grain sized material the microstructural steady state seems to be nearly reached. The observed dependency of the DRX grain size on the initial microstructure is clearly related to the stress-strain behavior of the material, shown in Fig. D.4. From the microstructural point of view, presented as misorientation path plots in Fig. D.14, a clear correlation of the intragranular orientation changes to the *metastable* DRX grain size was found.

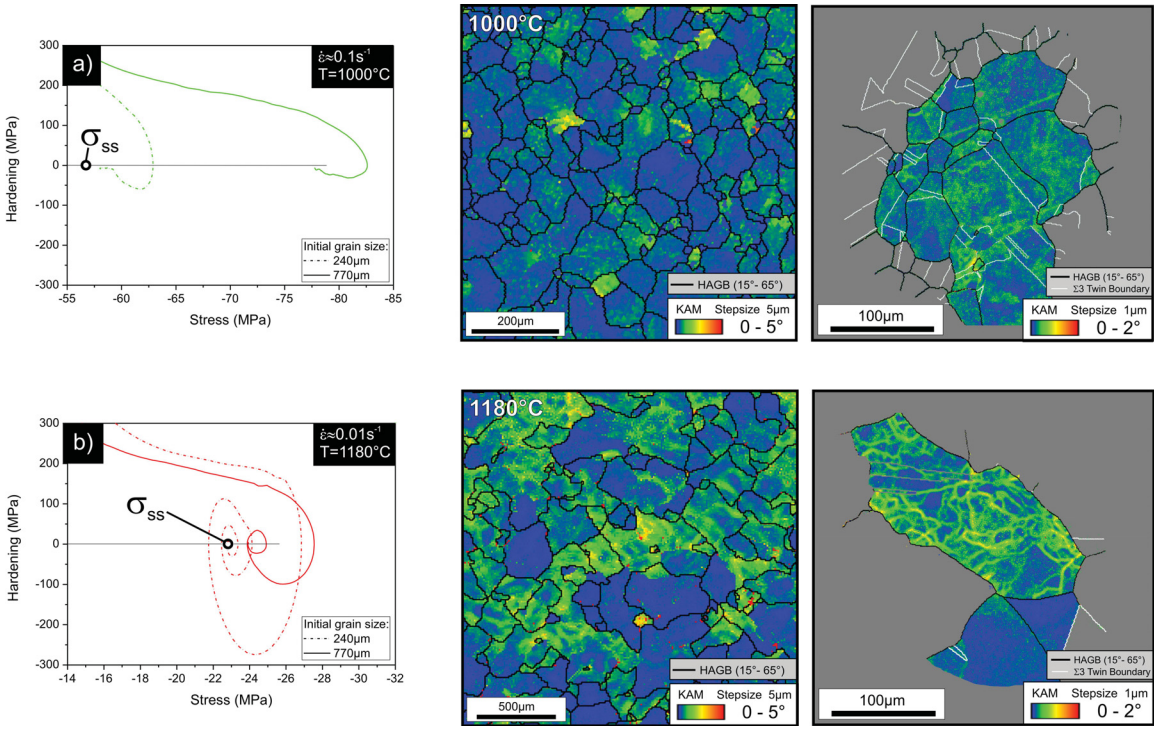

Figure D.15.: Hardening-stress curves of nickel with an initial grain size of 240 μm and 770 μm deformed at different strain rates and temperatures: (a) $\dot{\epsilon} \approx 0.1\,s^{-1}$ at 1000°C, and b) $\dot{\epsilon} \approx 0.01\,s^{-1}$ at 1180°C. KAM maps of the metastable microstructure of nickel with an initial grain size of 770 μm, deformed (a) to an ϵ of 57% and (b) to an ϵ of 35%, at the given forming parameters.

In contrary, without the intragranular substructure the *steady state* DRX grain size was observed due to the unrestricted grain boundary movement. The growth of a DRX grain stops when the current deformation of recrystallized grains decreases the driving force for grain boundary migration, or at deformation heterogeneities (marked with arrows in Fig. D.14), where a new grain will be frequently nucleated[8]. In other words, a large difference in dislocation density causes a fast motion of grain boundaries. However, by reaching an upper critical value, new grains nucleate, i.e. the first mechanism leads to a coarser the later one to a finer grained structure. An increase in forming temperature and a decrease in strain rate, which leads to a more homogeneous deformation, weakens the orientation gradients and decreases the influence of initial grain size on DRX grain size, as can be seen in Table D.1. From the comparison of the metastable stable to the steady state microstructure (taken from the initial finer grained material) and the hardening behavior, some tendencies for the further structural evolution process can be deduced. At higher Z parameters, the microstructure is characterized by the dominant occurrence of type A and type B grains, as shown in the misorientation maps of Fig. D.15 a). For these grains a small amount of homogeneously distributed misorientation in the grain interior was found. The absence of pronounced crystal

orientation gradients at grain boundaries, a typical feature of type C grains, shows that the material is far away from a further recrystallization cycle. From the extrapolation of the hardening behavior at the metastable state it can be estimated that the steady state will be reached by a slight softening of the material. On the basis of these facts, we assume that continuous grain coarsening of the existing metastable A and B structures significantly contributes to reaching the microstructural steady state. Whereas a lower Z parameter leads to a completely different behavior. All three grain structures(A,B,C) are present and nearly equally distributed in the metastable state (Fig. D.15 b). The used forming conditions provide the evolution of a well developed substructure due to pronounced dynamic recovery. The high misorientation at grain boundaries as well as the cyclic hardening behavior observed up to the metastable state argue for a highly synchronized process which is based on a high nucleation density. Therefore, at lowest Z parameters the necessary coarsening of the microstructure will be governed by nucleation and growing of new grains. As a consequence of the above mentioned structural evolution for both low and higher Z values, the resulting flow stress characteristics to reach the steady state flow stress σ_{ss}, are plotted as dashed line in Fig. D.13.

D.5. Conclusion

Polycrystalline nickel with different starting grain sizes of 240 μm and 770 μm was deformed in compression in the temperature range from 25°C-1180°C, at strain rates of $\dot{\epsilon} \approx 0.01\, s^{-1}$ and $\dot{\epsilon} \approx 0.1\, s^{-1}$. The material showed an abnormal flow behavior at forming temperatures from 450°C to 1000°C. At the beginning of the deformation a higher flow stress for the finer grained material was observed. Further straining changed the flow stress behavior in the opposite direction. With increasing forming temperature this change was shifted to a smaller plastic strain or flow stress. Furthermore, these differences are also persistent at larger plastic deformations, after DRX occurred as the main softening mechanism. An outstanding microstructural feature is that the initial coarser grained material results in a finer DRX grain size than the material with the finer starting microstructure. These differences were smaller for the lowest strain rate and diminish at the highest forming temperature of 1180°C. Based on these experimental results the following conclusion can be made:

- The anomalous flow behavior results from SIBM. In finer grained material the softening process due to the higher grain boundary density and therefore the higher affected volume – responsible for the reduction of dislocation density in the vicinity of grain boundaries – is stronger than in the coarser grained material.
- The onset of DRX is shifted to higher strains and stresses for an increase in starting grain size. This observation can be reduced to a simply nucleation problem. On the one hand the decrease in grain boundary density is equivalent to a reduction of potential nucleation sites and on the other hand it simultaneously reduces the fluctuation of the driving force of grain boundary motion, which is identified as a necessary step to trigger the nucleation process by bulging out of grain boundaries and annealing twinning.
- Contrary to the literature, the recrystallized microstructure shows a strong dependence on the starting microstructure. In fact, an increase of the initial grain size decreases the DRX grain size. Owing to the problematic nucleation in coarser grained materials, much more energy is stored before nucleation starts. In spite of all of these deviations at the metastable state, it is expected that a larger deformation will lead to the stable state grain size.

Bibliography

[1] H.J. McQueen, J.J. Jonas, Recovery and recrystallization during high temperature deformation, in: Treatise on Materials science and technology, vol. 6, Academic Press, New York, 1975, pp. 393-493.

[2] C.M. Sellars. Phil. Trans. R. Soc. Lond. A 288 (1978) 147-158.

[3] C.M. Sellars. Met. Forum 4 (1981) 75-80.

[4] H.J. McQueen. Met. Forum 4 (1981) 81-91.

[5] R.D. Doherty, D.A. Hughes, F.J. Humphreys, J.J. Jonas, D.J. Jensen, M.E. Kassner, W.E. King, T.R. McNelley, H.J. McQueen, A.D. Rollett. Mater. Sci. Eng. A 238 (1997) 219-274.

[6] H.J. McQueen, Dynamic recovery and recrystallization, in: K.H.J. Buschow, et al.(Eds.), Encyclopedia of Materials: Science and Technology, Elsevier Science Ltd. Oxford, 2001, pp. 2375-2381.

[7] H.J. McQueen. Metall. Mater. Trans. A 33 (2002) 345-362.

[8] F.J. Humphreys, M. Hatherley, Recrystallisation and Related phenomena, second ed., Pergamon Press, Oxford, 2003.

[9] F. Montheillet. Rev. Metall. 9 (2002) 767-776.

[10] H.J. McQueen, C.A.C. Imbert. J. Alloys Compd. 378 (2004) 35-43.

[11] H. Miura, M. Osama, R. Mogawa, T. Sakai. Scripta Mater. 48 (2003) 1501-1505.

[12] H. Miura, T. Sakai, R. Mogawa, G. Gottstein . Scripta Mater. 51 (2004) 671-675.

[13] H. Miura, T. Sakai, H. Hamaji, J.J. Jonas. Scripta Mater. 50 (2004) 65-69.

[14] C. Escher, G. Gottstein. Acta Mater. 46 (1998) 525-539.

[15] S. Mahajan, C.S. Pande, M.A. Imam, B.B. Rath. Acta Mater. 45 (1997) 2633-2638.

[16] J.P. Sah, G.J. Richardson, C.M. Sellars. Met. Sci. 8 (1974) 325-331.

[17] R.D. Doherty, in: F. Haessner (Ed.), Recrystallization in Metallic Materials, Dr. Riederer Verlag, Stuttgart, 1978 pp. 2361.

[18] L. Blaz, T. Sakai, J.J. Jonas. Met. Sci. 17 (1983) 609-616.

[19] S. Sakui, T. Sakai, K. Takeishi. Trans. Iron Steel Inst. Jpn. 17 (1977) 718-725.

[20] T. Sakai, J.J. Jonas. Acta Metall. 32 (1984) 189-209.

[21] In: T. Sakai, in: S. Yue and E. Essadiqi (Eds.), Thermomechanical Processing of Steels (J.J. Jonas Symp.), TMS-CIM, Montreal, 2000, pp. 47-62.

[22] A. Belyakov, H. Miura, T. Sakai. Mater. Sci. Eng. A 255 (1998) 139-147.

[23] H. Miura, H. Aoyama, T. Sakai. J. Jpn. Inst. Met. 58 (1994) 267-275.

[24] G. Angella, B.P. Wynne, W.M. Rainforth, J.H. Beynon. Mater. Sci. Eng. A 475 (2008) 257-267.

[25] OIM Analysis 4.5, User Manual, TexSEM-Labs. Inc., 2004.

[26] A. Vorhauer, T. Hebesberger, R. Pippan. Acta Mater. 51 (2003) 677-686.

[27] G. Gottstein, E. Brünger, M. Frommert, M. Goerdeler, M. Zeng. Z. Metallk. 94 (2003) 628-635

[28] U.F. Kocks, H. Mecking. Prog. Mater Sci. 48 (2003) 171-273.

[29] O.N. Senkov, J.J. Jonas, F.H. Froes. Mater Sci. Eng. A 255 (1998) 49-53.

[30] H. Margolin, M.S. Stanescu. Acta Metall. 23 (1975) 1411-1418.

[31] Z. Jiang, J. Lian, B. Baudelet. Acta Metall. Mater 43 (1995) 3349-3360.

[32] T. Sakai, M. Ohashi. Mater. Sci. Technol. 6 (1990) 1251-1257.

[33] T. Sakai, Y. Nagao, M. Ohashi, J.J. Jonas. Mater. Sci. Technol. 2 (1986) 659-665.

E

Warm forming of an austenitic stainless steel: the effect of grain size under different forming conditions on the microstructural evolution

C. Rehrl[a], S. Kleber[b], O. Renk[a], R. Pippan[a]

[a] Erich Schmid Institute of Materials Science, Austrian Academy of Sciences,
A–8700 Leoben, Austria
[b] Böhler Edelstahl GmbH,
A–8605, Austria

Abstract

The influence of initial grain size on the dynamic recrystallization behavior has been investigated in a technical austenitic stainless steel. Compression tests were performed at different warm forming conditions. In order to capture the microstructural evolution after the deformation the electron back scatter diffraction technique (EBSD) was used. The results show that nucleation of new grains is strongly grain size dependent. Increasing the size of the starting microstructure lowers the grain boundary density per unit volume and furthermore it reduces the stored energy, well known as driving force for structural instability dynamic recrystallization. This leads to the problem of grain refinement in coarse structured materials. Applying large plastic strains or using static recrystallization in a double hit forming process sounds promising for an efficient refinement strategy.

E.1. Introduction

Warm- and hot forming of metals and alloys have been extensively studied in the last decades.[1–15] Many investigations were motivated by improving understanding of the grain refinement process to enhance the mechanical properties. In medium to low stacking fault energy materials, such as austenitic stainless steels, the final microstructure in the majority of cases is controlled by the occurrence of discontinuous dynamic recrystallization (DDRX). In this context new grains evolve by the serration of preexisting grain boundaries and pronounced recovery.[6,16–20] The migration and sliding of the grain boundary accompanied by annealing twinning mechanisms are the essential steps for the formation of a new nucleus.[6,18,21,22]
Several authors investigated the effect of coarser starting grain size and reported of slowing down on the dynamic recrystallization (DRX) kinetics.[23,30–35] They all agree that the reduction of available nucleation sites by decreasing the grain boundary area per unit volume is responsible for the observed change in the dynamic recrystallization (DRX) behavior. Due to this lack of grain boundaries in coarser grained structures (e.g. materials in the cast state) the intragranular nucleation process becomes predominant. Therefore, structural heterogeneities such as deformation bands, twins and high angle grain boundaries, which are formed during plastic deformation process, serve as nucleation sites.[23–25] These studies stated that the preexisting grain boundary fraction determines the nucleation density. The role of the stored energy and the deformation substructure on the dynamic nucleation process, which are both clearly grain size dependent, has not been investigated.
The present work examines the influence of initial grain size and the applied forming parameters on the nucleation process of new grains. Compression tests at hot forming temperatures using a technical relevant austenitic stainless steel are carried out in order to better understand the microstructural refinement- and homogenization-process in coarse grained materials. The as-deformed microstructure is captured by EBSD-analyses on different length scales. The characterization of the mechanisms controlling the structural evolution should give inputs for new efficient forming strategies.

E.2. Experimental procedure

In this study the influence of different forming parameters on an austenitic stainless steel were investigated. The steel grade A220 produced by Böhler Edelstahl GmbH is a single phase fcc steel which has a similar composition to the steel grade 316L. The chemical constitution is given in Table E.1.

Fe	Cr	Ni	Mo	Mn	Si	N	C
63.2	17.5	14.5	2.7	1.7	0.3	0.07	0.03

Table E.1.: Chemical contents (in wt%) of the stainless steel A220.

Cold worked	Heat treatment	Microstructure	Grain size
	commercial available state	globular	16 μm
125%	1080°C/1 min	globular	26 μm
45%	1180°C/1 min	globular	120 μm
45%	1180°C/90 min	globular	205 μm
	cast state	columnar	mm-sized mm

Table E.2.: Heat treatment and microstructure features.

To understand the influence on grain size, several sets of specimen with different initial grain size D_0 of 16, 26, 120, 205 μm (globular structured) and a cast material with mm-sized grains (columnar structured) were used. To obtain this large range of grain sizes a cold rolling step at ambient temperature with a subsequent thermal heat treatment on the cast structured material was performed. Table E.2 shows the used forming and annealing parameters and the resulting grain size with the corresponding microstructure. As grain size, the internal grain boundary spacing was determined by a linear interception method, excluding the twin boundaries.
The compression test samples with a diameter of 10 mm and a height of 12 mm were machined out from the preprocessed material. To prevent misalignment of the compression axis during testing, plane parallel top faces were produced by a mechanical grinding procedure. The samples were deformed at a constant crosshead-speed of 5 or 50 mm/min (average strain rate $\dot{\epsilon}$ of $0.01s^{-1}$ or $0.1s^{-1}$) at constant temperatures of 810, 980 or 1150°C by using a compression test unit (Schenck-Trebel). The forming conditions temperature T and strain rate $\dot{\epsilon}$ are described by a single parameter, the Zener-Holloman parameter Z

$$Z = \dot{\epsilon} \cdot exp(Q/RT), \tag{E.1}$$

where Q is the activation energy for warm forming and R the universal gas constant. After the forming step the samples were water quenched to prevent the material from metadynamic- and static softening processes. It should be pointed out that deformation experiments on the material with the smallest grain size of 16 μm (commercial available state) were only performed at 810 and 980°C due to stability problems of the grain structure at 1150°C forming temperature.
The structural analysis of the deformed material is based on the measurements of the local crystal orientation, carried out with an TSL EBSD-SEM system interfaced to a LEO 1525. The sample surfaces were polished mechanically as well as electro-chemically to remove the cold working layer of the mechanical preparation step. The rearrangement of crystallographic orientation and the estimation of the microstructural stored energy after the forming process are plotted as Inverse Pole Figure (IPF) maps and as Kernel Average Misorientation (KAM) maps.

$$\Delta g_k = \frac{1}{12} \sum_{i=1}^{12} \Delta g_i \tag{E.2}$$

The kernel misorientation between the center point and all points at the perimeter of the kernel are measured. The local misorientation value Δg_k assigned to the center point is the average of these misorientations Δg_i as given in equation E.2. To weaken the influence of single erroneous data points on the results, the second neighbors at the perimeter were taken for the determination of KAM. The determination of KAM is similar to the analyses proposed by Vorhauer et al.[27], for details see OIM user manual.[26]

E.3. Results

E.3.1. Stress-strain behavior

In Fig. E.1 (a) to (c), the stress-strain curves of the different initial microstructures are plotted. The samples were deformed at different temperatures with a constant crosshead speed equivalent to a strain rate of about $\dot{\epsilon} \approx 0.01\, s^{-1}$ and $\dot{\epsilon} \approx 0.1\, s^{-1}$. Generally, for a lower strain rate a reduced flow-stress was observed. This influence of the strain rate on

the stress-strain behavior weakens at lower forming temperatures, where the flow stress is more effected by the initial grain size. The variation of deformation parameters to a lower

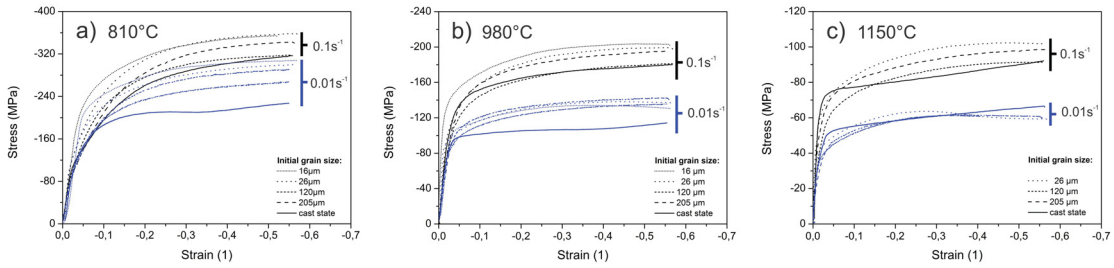

Figure E.1.: Stress-strain curves of A220 with different initial grain sizes deformed at constant temperature of 810°C, 980°C or 1150°C and different crosshead speeds of 5mm/min ($\dot{\epsilon} \approx 0.01\,s^{-1}$) and 50 mm/min ($\dot{\epsilon} \approx 0.1\,s^{-1}$).

Zener-Holloman parameter Z as well as a finer initial grain size changed the whole stress-strain kinetic into a typical parabolic warm forming flow curve showing a peak stress, a slight stress drop and a steady state region. In contrast, with increasing forming temperature the stress-strain behavior of the cast material shifts from parabolic to an elbow like shape.
At the beginning of deformation, a higher hardening-rate for the finer grained material was observed. Further straining changed the stress-strain behavior in the opposite direction, i.e. the coarser grained material showed a higher hardening. With increasing forming temperature this change is shifted to a smaller plastic strain or flow-stress.

E.3.2. Microstructural evolution

Influence of the forming parameter on the microstructural evolution

The influence of deformation temperature on the microstructural evolution of an austenitic stainless steel with an initial grain size of 120 μm, deformed to ϵ=57% with a strain-rate of $\dot{\epsilon} \approx 0.1\,s^{-1}$ is shown in Fig. E.2. Notice that at the used forming conditions the steady state stress plateau could not be reached. In general for initially coarser grained materials, deformed at higher Z parameter, the structural steady state could not be reached by a compression test. The friction conditions during the compression test lead to the typical barreling and an inhomogeneous deformation. For that reason the discussion refers to the more uniform strained sample center. In the IPFs, black lines illustrate high-angle grain boundaries, red and blue lines show the intragranular misorientation greater than 15° and between 3 to 15° respectively. A typical feature of recrystallized grains are annealing Σ3 twins, marked in KAM maps as solid white lines. Fig. E.2 a) presents a microstructure with pronounced intragranular orientation gradients of 15° and more. The increase of the deformation temperature from (a) 810°C to (b) 980°C and to (c) 1150°C leads to a partly recrystallized microstructure with an annealed polygonized substructure inside the non re-crystallized deformation structure. This is quantitatively illustrated in Fig. E.2 d) as a decrease of the intgranular misorientation for increasing forming temperature.

Influence of the initial grain size on the microstructural evolution

IPFs in Fig. E.3 (a) to (c), illustrate the effect of initial grain size on the final microstructure. The samples were deformed to ϵ=57% ($\dot{\epsilon} \approx 0.1\,s^{-1}$) at a forming temperature of 810°C. For the 26 μm grain sized material (image E.3(a)), the observed microstructure at 810°C indicates

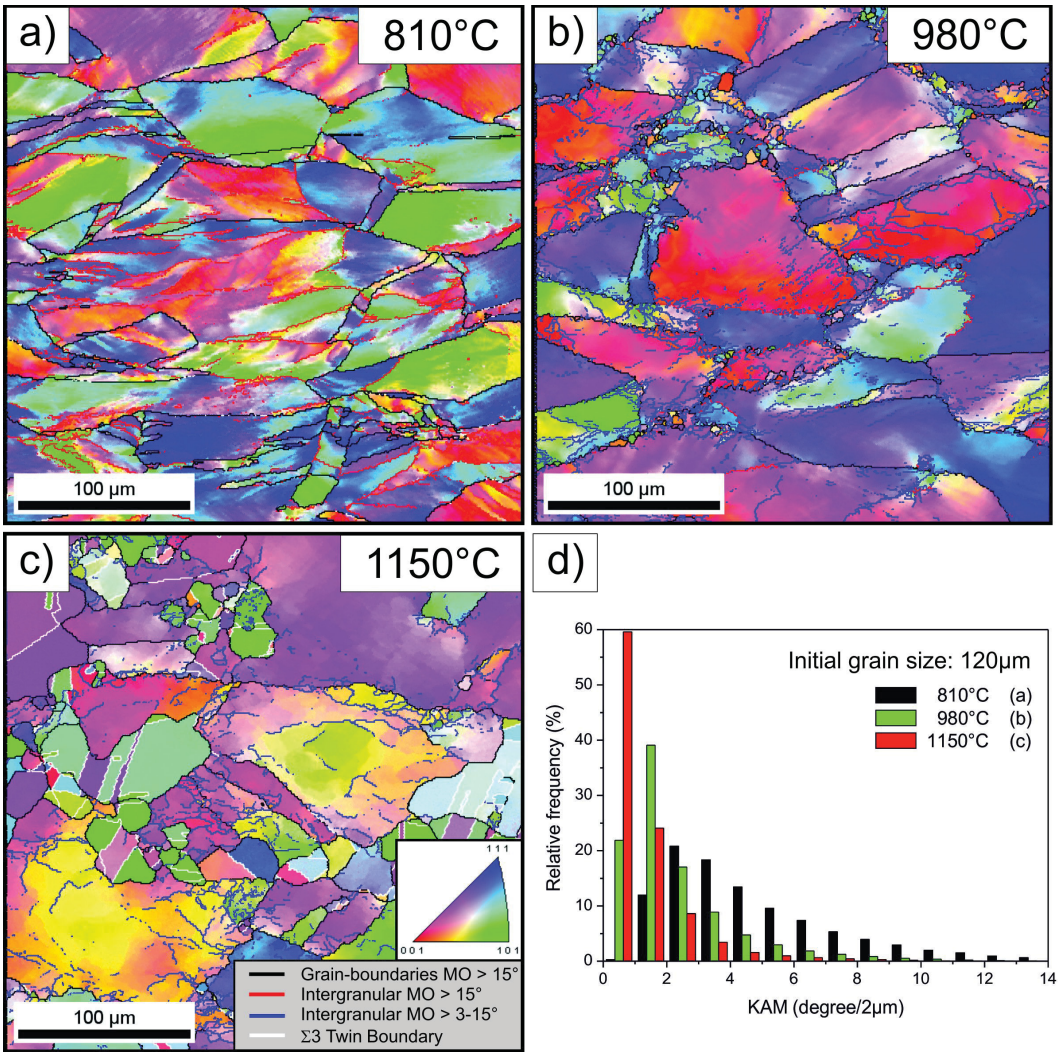

Figure E.2.: Microstructural evolution of an initially 120 μm grain sized material, shown as IPF (perpendicular to compression direction), strained ϵ=57% with an $\dot{\epsilon} \approx 0.1\,s^{-1}$ at (a) 810°C, (b) 980°C and (c) 1150°C. Grain boundaries and intragranular orientation gradients are marked with solid lines, see color code, (d) relative frequency of intragranular kernel average misorientation from 0 to 15°. In image a) intragranular misorientations from 3-15° are blanked to keep clarity.

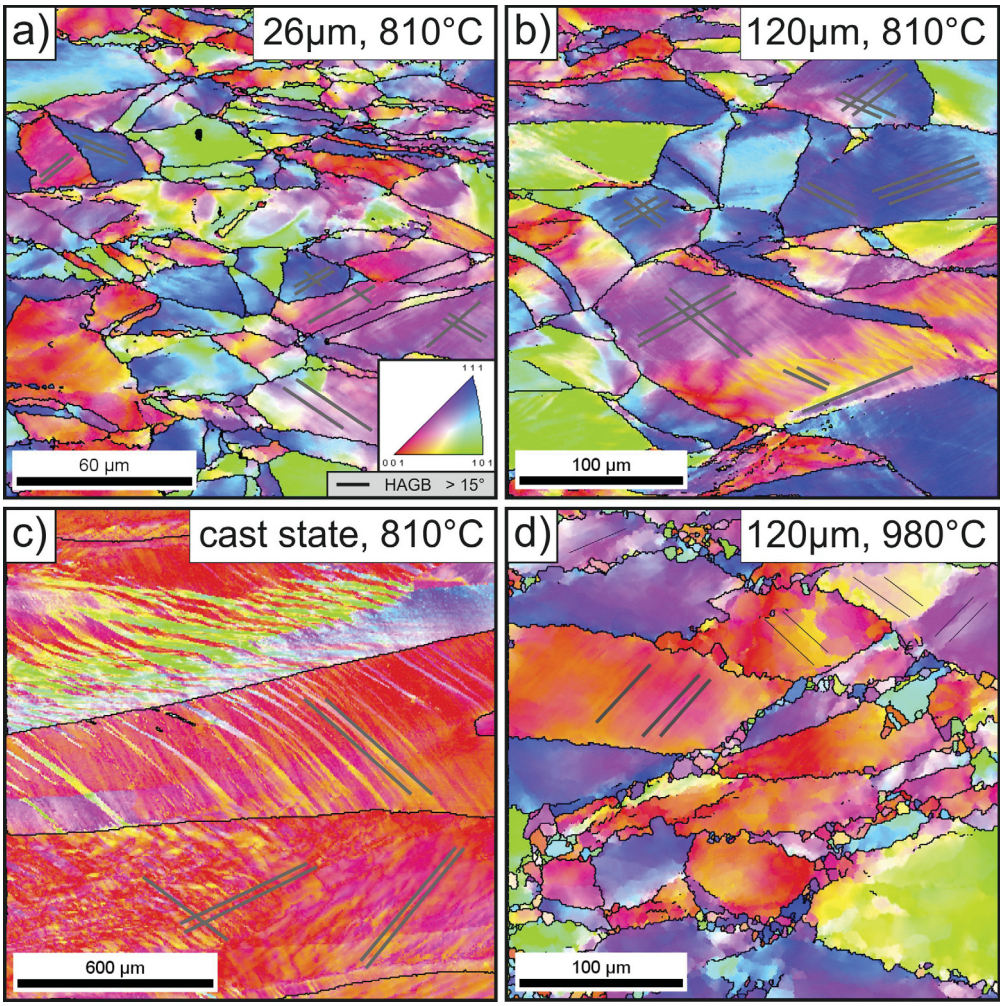

Figure E.3.: Microstructural evolution of samples with different initial grain sizes strained to an ϵ of 57%, are shown as IPFs (perpendicular to the compression direction). Images (a-c) deformed at 810°C with an $\dot{\epsilon} \approx 0.1\,s^{-1}$ and image (d) at 980°C with an $\dot{\epsilon} \approx 0.01\,s^{-1}$. High angle grain boundaries are marked as black lines and structural fragments are indicated with gray lines.

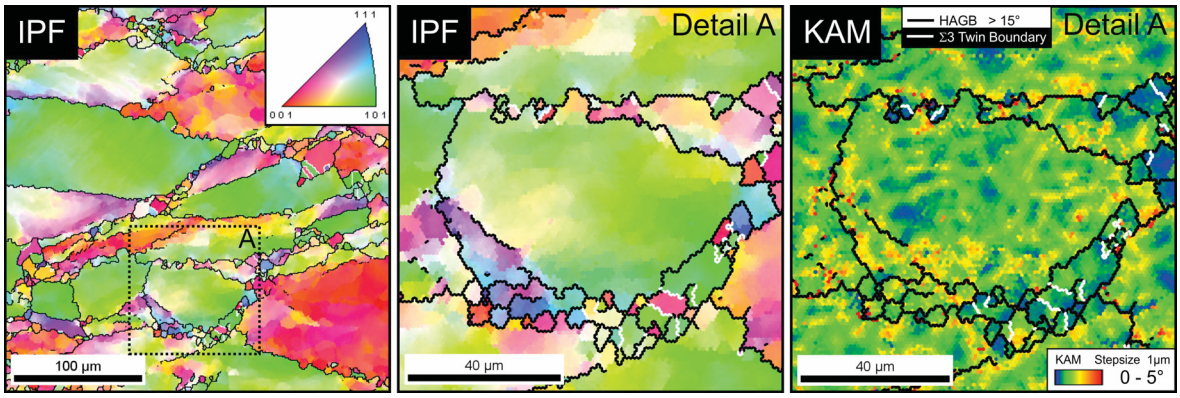

Figure E.4.: Nucleation of new grains in 120 μm grained material, deformed at 980°C with a strain rate of $\dot{\epsilon} \approx 0.01\,s^{-1}$ to an ϵ of 57%. IPFs in compression direction and the KAM of the selected area are taken from the sample center; high angle grain boundaries (black lines) and $\Sigma 3$ twin boundaries (white lines) are highlighted in these maps. The kernel average misorientation (KAM) is derived from Equation E.2. The kernel point contains information on the average misorientation of the perimeter at a radius of twice the step size.

a homogeneously deformed structure with slight orientation gradients (highlighted with dark gray lines). For the initially coarser grained materials of 120 μm grain size (image E.3 b)) and the cast structured one (image E.3 c)), these gradients are more pronounced and sharper developed compared to the 26 μm grain sized material. The IPF in image E.3 d) illustrates a 120 μm grain sized material deformed at 980°C and a strain rate of $\dot{\epsilon} \approx 0.01\,s^{-1}$. This decrease of Z value leads to a partly recrystallized microstructure, whereas in the remaining grains recovered polygonal substructures are present. In spite of the pronounced recovery process, a slight alignment of superstructural elements to prior structural fragmentation is already evident. Detail scans of image E.3 d) shown in Fig. E.4 illustrate the nucleation process of new grains in consideration of proper KAM maps. By using the kernel average misorientation it can easily be distinguished between recrystallized and non-recrystallized areas. Fig. E.4 clearly shows that strong grain boundary motion (displacement of the grain boundary in the size of a subgrain) and recovery took place before recrystallization started. Zones of high stored energy – as structural inhomogeneities such as old grain boundaries or new grain boundaries formed during the deformation process by recovery or shear strain localization – served as potential nucleation sites. As an outstanding feature, recovered subgrains with misorientations of more than 15° are formed during the plastic deformation process. KAM of this detail illustrates that these recovered regions have a higher misorientation and are free of annealing twins compared to the recrystallized grains. In Fig. E.5, the microstructural evolution of materials with initially different grain sizes, deformed at 980°C to ϵ=57% with $\dot{\epsilon}$ of $\approx 0.01\,s^{-1}$ and $\dot{\epsilon} \approx 0.1\,s^{-1}$, is shown. For a decrease in grain size, the microstructure changes from partly to nearly fully recrystallized. DDRX is the main nucleation process. The deformed microstructure is changed by the necklace mechanism, where new grain boundaries act as further nucleation sites, see Fig. E.5 for the 26 μm grain size.

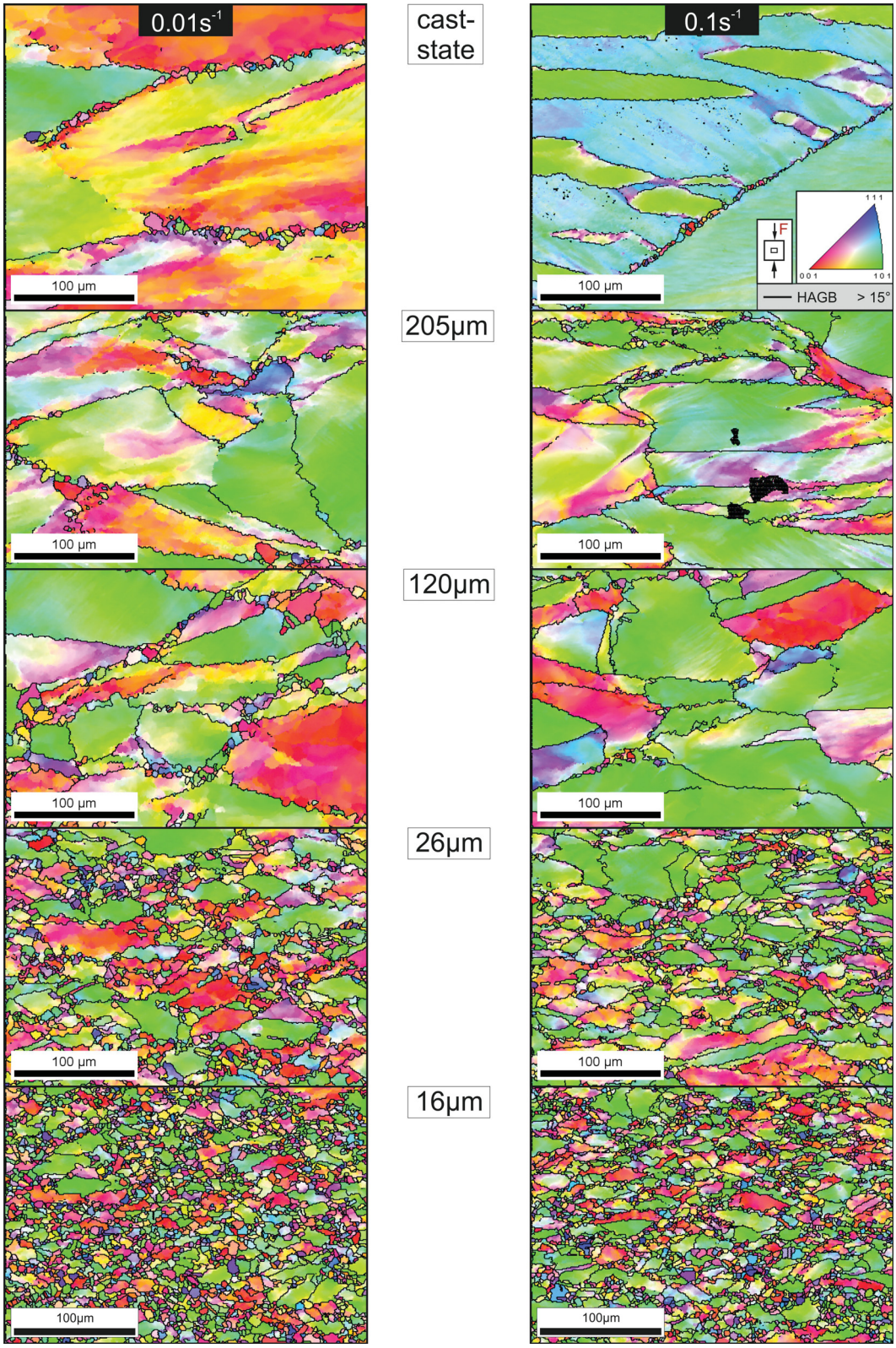

Figure E.5.: Microstructural evolution of different inital grain sizes, shown as IPF-maps in the compression direction, 57% strained at 980°C with an $\dot{\epsilon} \approx 0.01\,s^{-1}$ (left column) and $\dot{\epsilon} \approx 0.1\,s^{-1}$ (right column). High angle grain boundaries are marked as black lines.

E.4. Discussion

E.4.1. Effects of grain size on the mechanical behavior

The differences in flow stress at constant Z level, shown in Fig. E.1, confirmed the enormous influence of the starting grain size on the warm forming behavior of the material A220. This can be understood by using current work hardening theories, where grain boundaries act as main obstacles for dislocation slip. Based on the stronger dislocation pile up, or in other words the higher strain gradient, for initially finer grained materials the amount of geometrically necessary dislocations (GNDs) increases. The dependency of the intragranular average misorientation on the initial grain size captures this fact, see Fig. E.6. Deviations from classical hardening behavior – where finer grained material has a higher plastic flow stress than a coarser one – are present at larger plastic deformation (Fig. E.1). As shown in IPFs in Fig. E.3 the structural fragmentation process is more pronounced for coarser grained materials. The fragmentation induces intragranular dislocation pile up on a much smaller length scale as the initial grain size and leads to a harder material response. Additionally, at higher forming temperature (equivalent to a lower Z value) enhanced DRV and DRX for finer starting grain sizes are responsible for a softer material response, see Fig. E.6. The constant hardening rate with an elbow like shape for the coarse grained cast structured material can be explained by pronounced recovery with the suppression of DRX, see recovered microstructure in IPF in Fig. E.5 and the low density of the DRX grain fraction in Fig. E.6 of the cast structured material at 1150°C.

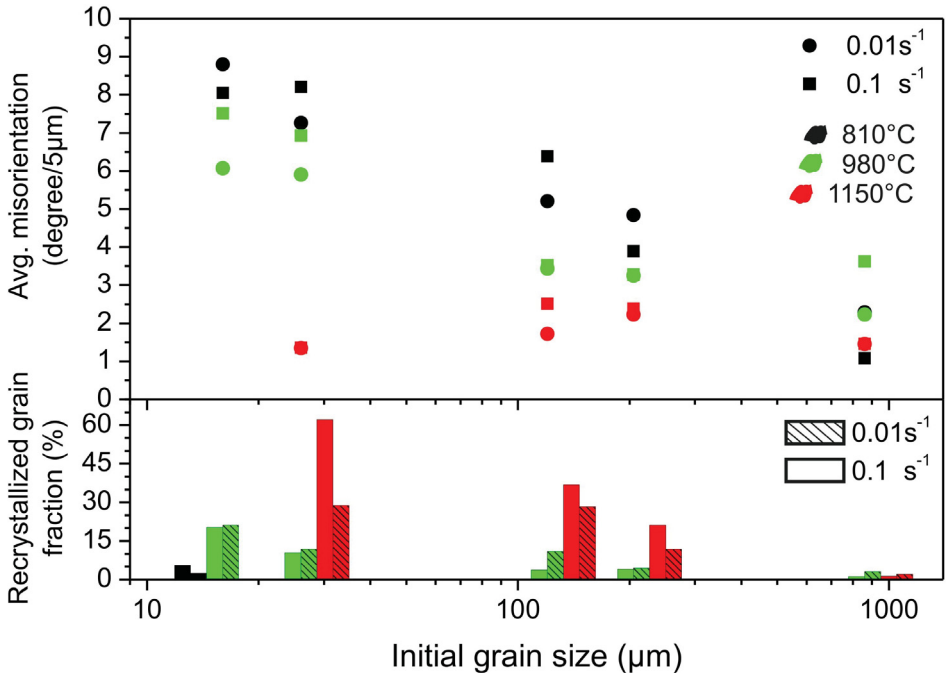

Figure E.6.: Grain size dependency of the recrystallized grain fraction and grain average misorientation for different Zener-Holloman parameters. Materials are 57% strained in the temperature range from 810°C-1150°C with an $\dot{\epsilon} \approx 0.01\,s^{-1}$ and $\dot{\epsilon} \approx 0.1\,s^{-1}$. The marked decrease in average misorientation, which is most pronounced for the small grain sized material deformed at 1150°C is due to the high amount of new recrystallized grains.

E.4.2. Effects of grain size on the nucleation process and the microstructural evolution

Warm forming of austenitic stainless steels is an extensively studied field, see for example.[1,6,11–15,29] In several publications, performed on different fcc structured materials, the influence of starting grain size on the DRX behavior was investigated. All these studies illustrate that for coarser microstructures a retardation and slowing down of the DRX kinetic was observed.[23,30–36] IPF-maps in Fig. E.5 and the corresponding quantitative analysis in Fig. E.6, illustrate the strong influence of the initial grain size on the recrystallized grain fraction. This observation can be explained in terms of a nucleation problem. A simple estimation of the dependency of grain boundary fraction on the grain size demonstrates a reduction of potential nucleation sites by a factor of 13 by increasing the grain size from 16 to 205 μm. On the one hand any change in grain size changes the grain boundary density per unit volume and on the other hand it directly effects the stored plastic energy, well known as the driving force for the the onset of the structural instability DRX. This is confirmed by the evolution of the intragranular average misorientation in Fig. E.6, which can be seen as a part of the total stored energy. A detailed observation from the microstructural point of view clearly shows that for finer grained structures the areas of highest stored energy are close to the grain boundary, where normally nucleation of new grains will take place. As already mentioned, in coarser grained materials the stored energy is in general lower (Fig. E.6) and more located at intragranular crystal orientation fragments. The sharpness, the lateral width and the misorientation between these fragments increase for a coarsening in starting grain sizes and with increasing Z parameter, see Fig. E.3. This observation can be explained by a strong crystalline texture with unfavorable crystal orientations to the macroscopic shear strain of the compression test. To fulfill the macroscopic plastic strain, crystal deformation with strong shear localizations instead of continuous straining of the whole crystal occurs. In finer, randomly distributed, crystalline structures few different orientated grains can more easily fulfill the macroscopic deformation and therefore shear localization is less pronounced. Decreasing the Z value DRV becomes more pronounced and intragranular misorientations will be reduced by the development of a well defined polygonized substructure, as shown in Fig. E.2 and Fig. E.3 d).
Returning to the nucleation process, new grains are formed by discontinuous dynamic recrystallization (DDRX), see Fig. E.4 IPF and KAM maps. The present study confirms that recovery triggers the nucleation process due to the formation and mobilization of subgrain boundaries. As reported in the literature, extensive grain-boundary motion and bulging on the scale of a nucleus of a new grain determine the nucleation process.[14,18,21] In the majority of the cases $\Sigma 3$ annealing twins take a part in the formation of new grains. Additionally, in coarser starting structures intragranular structural inhomogeneities formed during the deformation process serve as nucleation sites.

E.4.3. Grain refinement strategies in cast structured materials

Concerning, the problem of refining coarse grained materials, the following section is dedicated to efficient forming strategies. As mentioned in the sections E.4.1 and E.4.2, the initiation of DRX is retarded due to difficulties in the formation process of new grains. Owing to lower densities of high angle grain boundaries and the small amount of stored deformation energy in comparison initially finer grained structures, a weaker tendency to recrystallize results, see Fig. E.6. Therefore, the main objective is to increase the stored energy and to enhance the present density of potential nucleation sites by structural fragmentation processes:

Method A (compression test)

Based on the experimental observations in this work a combined forming process is recommended. In the first deformation step the coarse grained material will be prestrained at high Z values to induce a high density of nucleation sites for static recrystallization. The second forming step has to be performed at lower Z values to induce DRX.

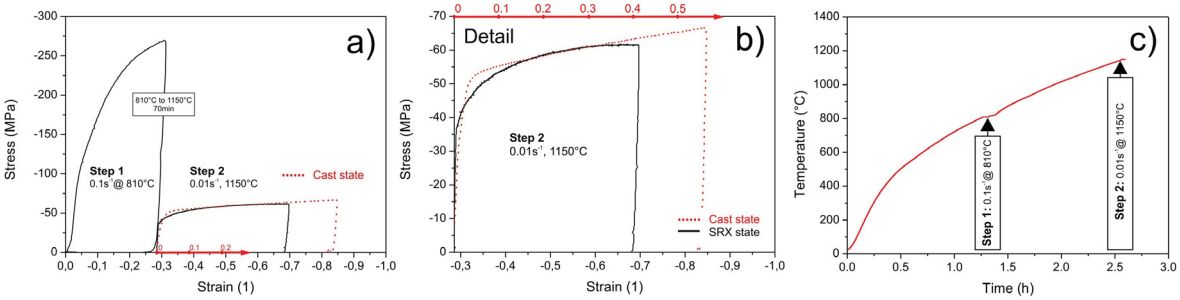

Figure E.7.: Stress strain behavior (a) and (b) and temperature characteristics (c) for a combined compression test of initially cast structured material A220, deformed at 810°C/$\dot{\epsilon} \approx 0.1\,s^{-1}$ and at 1150°C/$\dot{\epsilon} \approx 0.01\,s^{-1}$.

In Fig. E.7 a) the stress-strain behavior of the combined deformation experiment for different strain rates and temperatures is shown. Between the forming steps the material will be heated up and refined by static recrystallization. The amount of prestrain directly determines the static recrystallized grain size by the nucleation density, as shown in the quantitative analyses (Fig. E.8 f)) and IPFs of Fig. E.8 b) $\epsilon = 30\%$ and Fig. E.8 c) $\epsilon = 80\%$. From KAM maps follows that both different prestrained materials are fully static recrystallized and nearly misorientation free. The second deformation step, performed at a lower Z value, can easily initiate DRX, see Fig. E.8 d. The direct comparison of a cast structured material deformed in one single step Fig. E.8 e) or with the combined forming process Fig. E.8 d) to nearly the same accumulated strain clearly shows the efficiency of the recommended method. This is also confirmed by the stress strain behavior which is changed from an elbow like shape to a typical warm forming flow curve determined by extensive DRX.

Method B (torsion test)

Changing the deformation method from compression to torsion allows application of higher strains on the material. Inducing such high plastic deformation energy, the structural instability DRX in coarser grained structures can also be reached without changing the shape of the sample. Confirmed by the mechanical behavior, the maximum shear stress tends to the same saturation stress for high plastic strains. This is independent of the initial grain size, see stress-strain behavior in Fig. E.9c. IPF in Fig. E.9 (a) initially cast state and (b) a $205\,\mu m$ grain sized material illustrate the microstructural evolution after $\epsilon = 175\%$ at 1150°C. Both materials with different initial grain size indicate a nearly fully recrystallized microstructure in the outer, highly strained region. The new grain boundaries of the DRX grains serve as potential nucleation sites and trigger the further nucleation process in the cast structured material. Reducing the plastic strain, which is equivalent to the inner region of the torsion test sample, leads to a partially recrystallized and further on to an unrecrystallized microstructure. For the described methods an excellent formability of the material is required. Especially at deformation steps at lower temperatures and higher strain rates, in other words for a high Z parameter, the material can easily fail. For example, initially coarse grained materials fracture at lower plastic strain than the finer grained ones, see in Fig. E.9 (fracture

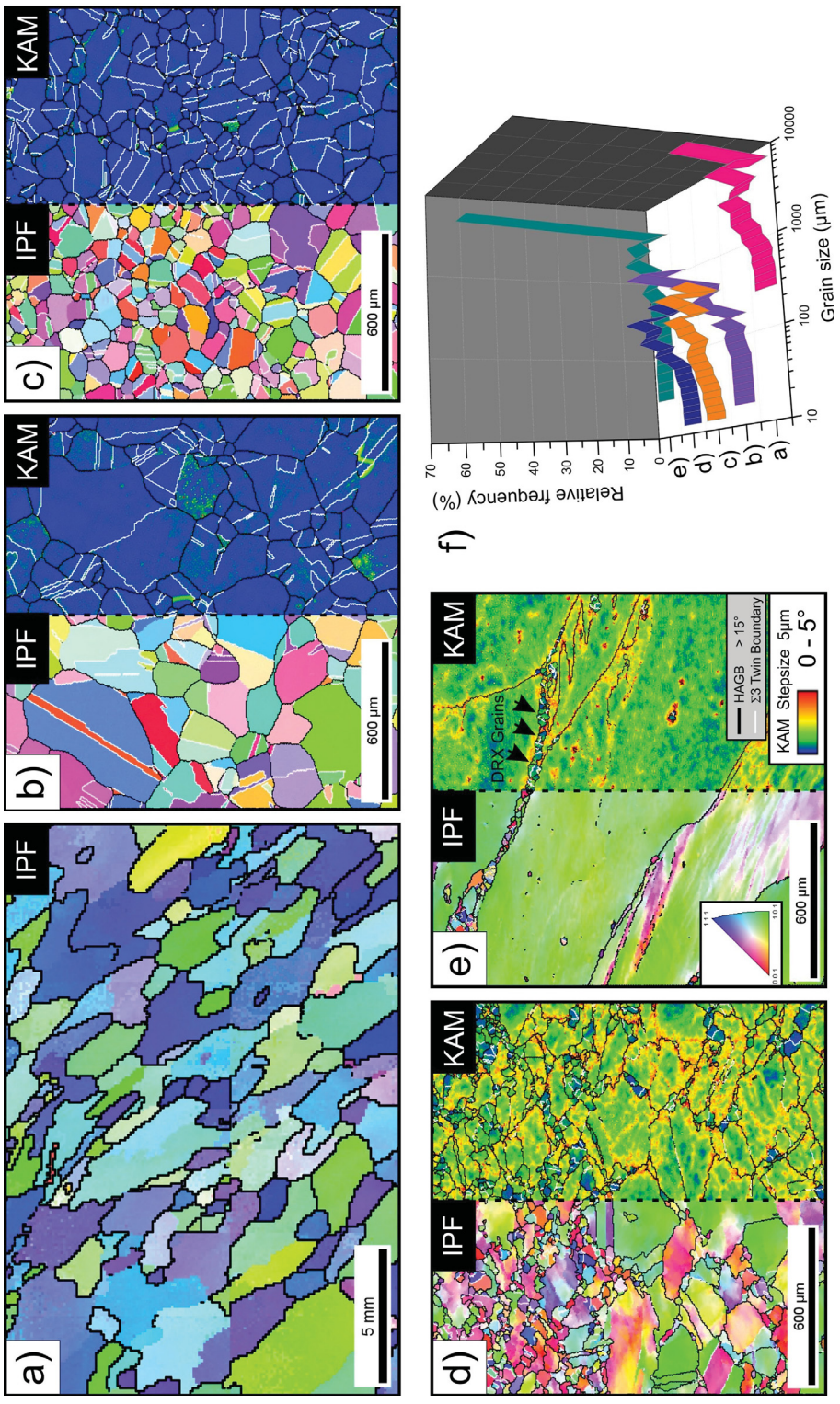

Figure E.8.: IPFs and KAM-maps of the material A220 at different forming conditions: (a) initially undeformed cast state, (b) and (c) are static recrystallized microstructures after heating up to 1150°C a material prestrained at 810°C/$\dot{\epsilon} \approx 0.1\,s^{-1}$ to an ϵ of 30% (b) and to an ϵ of 80% (c), (d) deformation step 2 of a 30% prestrained static recrystallized microstructure, at 1150°C/$\dot{\epsilon} \approx 0.01\,s^{-1}$; (e) initially undeformed cast state deformed at 1150°C/$\dot{\epsilon} \approx 0.01\,s^{-1}$ to an ϵ of 57%; (f) grain size distribution of microstructural states (a) to (e);

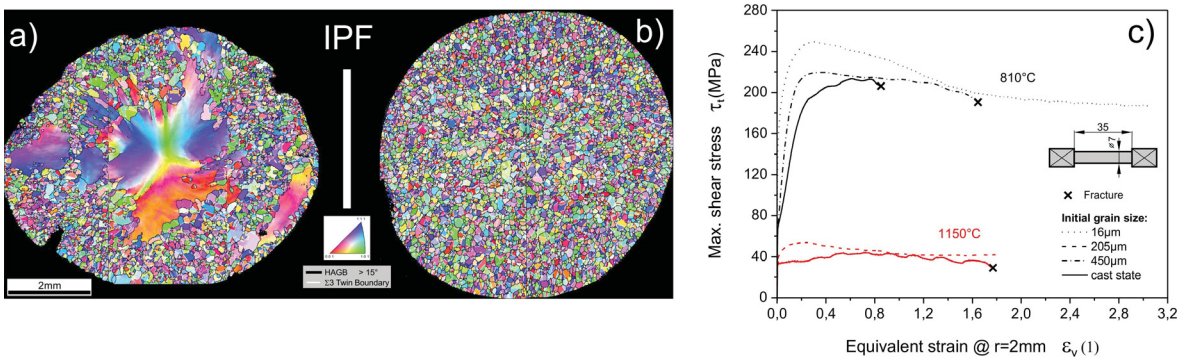

Figure E.9.: IPFs (tension direction) of torsion tested samples with different initial grain sizes (a) A220 initial cast structure and (b) A220 initial grain size:205 μm. Both materials were strained to $\epsilon_v = 175\%$ at 1150°C. (c) Stress-strain behavior of torsion tested specimens at 810 and 1150°C.

is marked with a cross). In these coarse structures strain localizations may easily extend the complete cross-section, due the large grain size, which is in the dimension of the sample diameter. Basically, for the refinement process a high stored energy is necessary but the formation of new grains in cast structures is a time consuming process.

E.5. Conclusion

Austenitic stainless steel with different initial grain sizes from μm-regime to the mm grain sized cast state was warm formed in the temperature range from 810 to 1150°C at strain rates of $\dot{\epsilon} \approx 0.01\,s^{-1}$ and $\dot{\epsilon} \approx 0.1\,s^{-1}$. The microstructural evolution of the material showed a strong dependency on the initial grain size and on the Zener-Holloman parameter Z. The decrease in the initial grain size enormously effects the geometrically necessary dislocation density per unit volume. This fact strongly influences the DRX behavior of the material.

- The increase in misorientation, which appears when decreasing the initial grain size, results from the requirement to fulfill the forming compatibility. Owing to the larger amount of grains, a higher density of geometrically necessary dislocations are stored per unit volume to achieve strain gradients at grain boundaries.

- The increase of the temperature compensated strain rate Z leads to a higher GND density and a more pronounced crystal fragmentation process. Depending on the strain path and the adjacent grains, crystalline orientation changes can be observed on all length scales. For a lowering of the Z value, the microstructural evolution is dominated by dynamic recovery and dynamic recrystallization.

- The mobilization of grain boundaries by preceding dynamic recovery plays a major role is the DRX nucleation process. The higher density of geometrically necessary dislocations, observed for initially smaller grained materials enormously enhances dynamic recovery. Combined with the fact of the higher amount of grain boundaries, which act as potential nucleation sites, the microstructural instability (DRX) is pronounced in finer grained structures.

- At the highest forming temperature a change from a parabolic to an elbow like shape of the flow curve occurs for the as cast state. A retarded and weaker dynamic recrystallization behavior due to the absence of potential nucleation sites, results in difficulties of

grain refinement in coarse grained structures. During the application of higher plastic strains new high angle grain boundaries evolve and act as further nucleation sites. A new double hit forming strategy, where the material is prestrained at higher Z values, static recrystallized and afterwards strained at a lower Z to induce dynamic recrystallization sounds promising for an industrial process.

Bibliography

[1] H.J. McQueen, J.J. Jonas, Recovery and recrystallization during high temperature deformation, in: Treatise on Materials science and technology, vol. 6, Academic Press, New York, 1975, pp. 393-493.

[2] C.M. Sellars. Phil. Trans. R. Soc. Lond. A 288 (1978) 147-158.

[3] C.M. Sellars. Met. Forum 4 (1981) 75-80.

[4] H.J. McQueen. Met. Forum 4 (1981) 81-91.

[5] R.D. Doherty, D.A. Hughes, F.J. Humphreys, J.J. Jonas, D.J. Jensen, M.E. Kassner, W.E. King, T.R. McNelley, H.J. McQueen, A.D. Rollett. Mater. Sci. Eng. A 238 (1997) 219-274.

[6] A. Belyakov, H. Miura, T. Sakai. Mater. Sci. Eng. A 255 (1998) 139-147.

[7] H.J. McQueen, Dynamic recovery and recrystallization, in: K.H.J. Buschow, et al.(Eds.), Encyclopedia of Materials: Science and Technology, Elsevier Science Ltd. Oxford, 2001, pp. 2375-2381.

[8] H.J. McQueen. Metall. Mater. Trans. A 33 (2002) 345-362.

[9] F.J. Humphreys, M. Hatherley, Recrystallisation and Related phenomena, second ed., Pergamon Press, Oxford, 2003.

[10] F. Montheillet. Rev. Metall. 9 (2002) 767-776.

[11] H.J. McQueen, C.A.C. Imbert. J. Alloys Compd. 378 (2004) 35-43.

[12] G. Angella, B.P. Wynne, W.M. Rainforth, J.H. Beynon. Acta Mater. 53 (2005) 1263-1275.

[13]) M. Jafari, A. Najafizadeh, J. Rasti. Journal of ISSI 4 (2007) 16-23.

[14] G. Angella, B.P. Wynne, W.M. Rainforth, J.H. Beynon. Mater. Sci. Eng. A 475 (2008) 257-267.

[15] A. Dehghan-Manshadi, M.R. Barnett, P.D. Hodgson Mater. Sci. Eng. A 485 (2008) 664-672.

[16] H. Miura, M. Osama, R. Mogawa, T. Sakai. Scripta Mater. 48 (2003) 1501-1505.

[17] H. Miura, T. Sakai, H. Hamaji, J.J. Jonas. Scripta Mater. 50 (2004) 65-69.

[18] H. Miura, T. Sakai, R. Mogawa, G. Gottstein . Scripta Mater. 51 (2004) 671-675.

[19] S. Mahajan, C.S. Pande, M.A. Imam, B.B. Rath. Acta Mater. 45 (1997) 2633-2638.

[20] C. Escher, G. Gottstein. Acta Mater. 46 (1998) 525-539.

[21] H. Miura, H. Aoyama, T. Sakai. J. Jpn. Inst. Met. 58 (1994) 267-275.

[22] In: T. Sakai, in: S. Yue, E. Essadiqi (Eds.), Thermomechanical Processing of Steels (J.J. Jonas Symp.), TMS-CIM, Montreal, 2000, pp. 47-62.

[23] J.P. Sah, G.J. Richardson, C.M. Sellars. Met. Sci. 8 (1974) 325-331.

[24] R.D. Doherty, in: F. Haessner (Ed.), Recrystallization in Metallic Materials, Dr. Riederer Verlag, Stuttgart, 1978 pp. 2361.

[25] L. Blaz, T. Sakai, J.J. Jonas. Met. Sci. 17 (1983) 609-616.

[26] OIM Analysis 5 User Manual, TexSEM-Labs. Inc; 2008.

[27] A. Vorhauer, T. Hebesberger, R. Pippan. Acta Mater. 51 (2003) 677-686.

[28] W. Pantleon. Scr. Mater. 58 (2008) 994-997.

[29] H.J. McQueen, N.D. Ryan. Mater. Sci. Eng. A 322 (2002) 43-63.

[30] W. Roberts, H. Bodén, B. Ahlblom. Met. Sci. 13 (1979) 195-205.

[31] M. Ohashi, T. Endo, T. Sakai, J. Japan Inst. Metals 54 (1990) 435-441.

[32] A. Belyakov, K. Tsuzaki, H. Miura, T. Sakai. Acta Mater. 51 (2003) 847-861.

[33] A.I. Fernández, P. Uranga, B. López, J. M. Rodriguez-Ibabe. Mat. Sci. Eng. A 361 (2003) 367-376.

[34] D.W. Suh, J.Y. Cho, K. Nagai. Metall. Mater. Trans. A 35 (2004) 3399-3408.

[35] A. Dehghan-Manshadi, P.D. Hodgson. Metall. Mater. Trans. A 39 (2008) 2830-2840.

[36] C. Rehrl, S. Kleber, O. Renk, R. Pippan. Mater. Sci. Eng. A 528 (2011) 6163-6172.